# Hard X-Ray Microanalysis with Parabolic Refractive Lenses.

Von der Fakultät für Mathematik, Informatik und Naturwissenschaften
der Rheinisch Westfälischen Technischen Hochschule Aachen
zur Erlangung des akademischen Grades
eines Doktors der Naturwissenschaften genehmigte Dissertation

vorgelegt von

Diplom-Physikerin Marion Kuhlmann
aus Bramsche.

Berichter: Universitätsprofessor Dr. B. Lengeler
Universitätsprofessor Dr. H. Lüth

Tag der mündlichen Prüfung: 13. August 2004

Diese Dissertation ist auf den Internetseiten der Hochschulbibliothek online verfügbar.

# Contents

# Chapter 1

# Introduction

Since their discovery by Wilhelm Conrad Röntgen in 1895 X-rays have been used in analytical applications. Most common, X-rays are known as medical diagnostic tools due to their ability to non-destructively pass through matter which cannot be penetrated by visible light.

Beside this, many physical analysis methods rely on the properties of X-rays. Hard X-rays cover the energy range from about $1000\,eV$ to $200\,keV$, which correspond to a large part of the spectrum of electronic and a few nuclear transitions in atoms. Therefore, the elemental composition of a sample can be analyzed by its emitted fluorescence radiation. Likewise absorption spectroscopy can describe the chemical state and the short range environment of an element. Further, the hard X-rays wavelengths of $10\,\text{Å}$ to $0.05\,\text{Å}$ allow to study the structure of condensed matter, as they are in the range of characteristic interatomic distances. This is the foundation of X-ray crystallography.

As powerful as these analytical methods may be, many applications need a focused X-ray beam. Especially, heterogeneous samples and complex structures benefit from the higher spatial resolution of a micro focused beam. Some focusing optics are able to implement high resolution imaging. For soft X-rays, full field and scanning microscopy have been realized by means of Fresnel zone plates as optical elements. However most optics (like mirrors, multi layers, capillaries, Fresnel zone plates, and Bragg-Fresnel optics) become less efficient with higher X-ray energies.

This thesis follows the development of microscopy, micro probing, and micro diffraction in the hard X-ray range based on parabolic refractive lenses. Obviously, refractive lenses for visible light are most successful. But the weak refraction and strong absorption of hard X-rays in matter make the realization of refractive lenses difficult. The first refraction experiment by Röntgen led to the conclusion that there are non refractive lenses for X-rays. Since then, the concept have been controversially discussed and was mainly considered as unrealistic. Highly brilliant X-ray sources and advanced instrumentation are the foundation for the first experiment, which used refractive X-ray lenses, by Snigirev, et al., in 1996. The aperture of refractive lenses for hard X-rays is comparable to their radius of curvature. Therefore, spherical refractive lenses suffer from aberration and are not appropriate for microscopy and other imaging applications. Parabolic refractive hard X-ray lenses have solved this problem. A full field hard X-ray microscope which used a stack of parabolic refractive aluminium lenses was first implemented in 1999 by Lengeler, et al.

To improve the imaging application of parabolic refractive lenses and to enhance the meaningful energy range beryllium lenses have been developed. Their benefits for analytical appli-

cation are outlined in the chapters 4 and 5.

Microanalysis with hard X-rays has benefited from the high brilliance of 3rd generation synchrotron radiation sources. The experiments were carried out at the European Synchrotron Radiation Facility ESRF in Grenoble, France, and at the Advanced Photon Source APS at Argonne National Laboratory, USA. The next generation of synchrotron radiation sources will be the X-ray free electron laser XFEL, whose spectral brilliance is expected to be several orders of magnitude higher than that of present synchrotron radiation sources. Beryllium refractive lenses will probably allow microanalysis despite the high power of these new sources. Arranging the individual lenses in a stack gives the refractive X-ray lenses a high degree of flexibility concerning choice of energy and spot size. In that way, standard small angle scattering experiments were improved. Also, parabolic beryllium lenses were used in implementing XANES microtomography. This combination of near edge absorption spectroscopy with two dimensional scanning microscopy allows to examine the chemical state and the local environment of a given atomic species in a virtual slice through a sample without really cutting it. The opportunities of this powerful approach are outlined in chapter 6.

The demand for X-ray microprobes with still smaller spot size is growing. For this reason nanofocusing refractive lenses have been designed in Aachen. A prototype made out of silicon is presented in chapter 7. With this first nanofocusing hard X-ray lens we were able to enhance the results of fluorescence nanotomography experiments and nanodiffraction, already. In the near future focusing of hard X-rays with refractive lenses below 100 nm is a realistic goal, opening the way to study biologic cells and structures of nanotechnologic devices.

# Chapter 2

# Optics for Hard X-Rays

The interaction of X-ray with matter is discussed in this chapter. Then, hard X-ray optics will be introduced, followed by a general presentation of refractive lenses, including their design concept, the choice of material, and their classification as hard X-ray optic.

## 2.1 Interaction of X-Rays with Matter

At a boundary between vacuum to matter X-rays are refracted and reflected. Inside the matter they are attenuated by absorption and scattering. If the material has a periodic structure diffraction can occur. Further, inhomogeneities in the material generate small angle scattering.

The propagation of an electromagnetic wave in matter depends on its wavelength $\lambda$ and on the material to interact with. Different phase velocities for different materials are expressed by the index of refraction $\mathsf{n}$ [1].

$$\mathsf{n} = 1 - \delta + i\beta. \tag{2.1}$$

The refraction is described by the real part 1-$\delta$ whereas the attenuation of X-rays in matter is described by $\beta$.
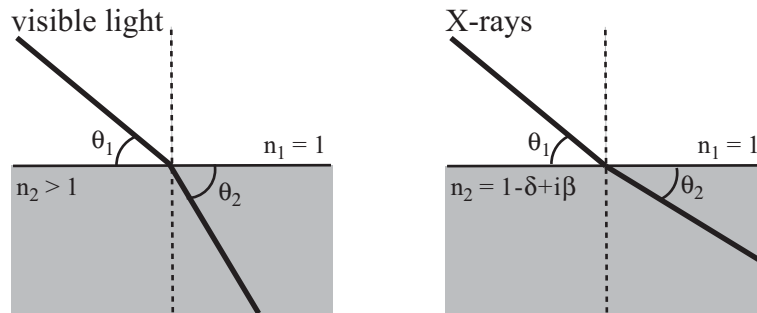


Figure 2.1: Refraction at the boundary between vacuum and matter for visible light and for X-rays according to Snell's law, equation (2.2). In contrast to visible light, X-rays are refracted away from the surface normal.

**Refraction:** the change in direction of a beam at the boundary between two media is expressed by Snell's law [2]. It is common for X-rays to consider the incident angle between the ray and the surface of the boundary and not to the surface normal. Therefore, Snell's law appears as

$$\mathsf{n}_1 \cos\theta_1 = \mathsf{n}_2 \cos\theta_2. \tag{2.2}$$

The indices of refraction $\mathsf{n}_1$ and $\mathsf{n}_2$ refer to the two materials, respectively, between which the boundary is considered. The incident angle is $\theta_1$, whereas $\theta_2$ is the refracted angle.
The differences of the refraction in case of visible light and X-rays are illustrated in figure 2.1. The index of refraction in vacuum is unity. For visible light, $\mathsf{n}$ in matter is always larger than unity. Hence, a beam is refracted to the surface normal. Contrarily, for X-rays in matter, 1-$\delta$ is smaller than unity. In this respect the beam is refracted away from the surface normal. The index of refraction decrement $\delta$ is given by

$$\delta = \frac{\mathsf{N_A}}{2\pi} r_0 \lambda^2 \frac{\varrho}{\mathsf{A}} \cdot (\mathsf{Z} + f') \tag{2.3}$$

material parameter:
| | |
|---|---|
| $\mathsf{A}$ | atomic mass [g/mol] |
| $\mathsf{Z}$ | atomic number |
| $\varrho$ | the density |
| $f = f_0(\mathsf{Q}) + f' + if''$ | atomic scattering factor |
| $\quad = \mathsf{Z} + f' + if''$ | in forward direction,   listed in [3] |

physical constants:
| | |
|---|---|
| $\mathsf{N_A} = 6.022 \cdot 10^{23}\,\mathrm{mol}^{-1}$ | Avogadro number |
| $r_0 = e^2/mc^2$ | |
| $\quad = 2.818 \cdot 10^{-15}\mathrm{m}$ | classical radius of the electron |

Typically, $\delta$ is of the order $10^{-6}$ [e. g., $\delta_{Be}(12\,\mathrm{keV}) = 2.4 \cdot 10^{-6}$ or $\delta_{Al}(23.3\,\mathrm{keV}) = 1 \cdot 10^{-6}$]. As a consequence, a focusing lens for X-rays must have a concave form, whereas it is convex for visible light. In addition, the change of angle is very small. With $\theta_1 = 45°$ and $\delta = 10^{-6}$ the change in beam direction at the the boundary between vacuum and matter is only $\Delta\theta = 0.2"$. Thus, many refractive X-ray lenses are needed in order to achieve a small focal length, below $1\,\mathrm{m}$.

**Attenuation:** the imaginary part $\beta$ of the refractive index is linked to the linear attenuation coefficient $\mu$ by equation (2.5).

$$\beta = \frac{\mathsf{N_A}}{2\pi} r_0 \lambda^2 \frac{\varrho}{\mathsf{A}} \cdot f'' \tag{2.4}$$

$$\phantom{\beta} = \frac{\mu\lambda}{4\pi} \tag{2.5}$$

The attenuation of the transmitted intensity $\mathsf{I}$ passing though a homogeneous material of thickness $\mathsf{d}$ is described by the Lambert-Beer law

$$\mathsf{I} = \mathsf{I}_0 \cdot e^{-\mu\mathsf{d}}. \tag{2.6}$$

Here, $\mathsf{I}_0$ represents the incident intensity and the linear attenuation coefficient $\mu$ is the inverse of the characteristic length of the exponential decay.

Different effects contribute to the attenuation: photoabsorption coefficient $\tau$, scattering processes $\mu_S$, and pair production $\mu_P$. For energies below $120\,\text{keV}$ $\mu_P$ is zero.

$$\mu = \tau + \mu_S + \mu_P. \tag{2.7}$$

In the context of refractive hard X-ray lenses the photoabsorption is dominant. A strongly bound electron in an atom absorbs a photon, while the nucleus accounts for the momentum balance in the process. The stronger the electron is bound, the higher is the probability that a photoabsorption process occurs. This corresponds to a photoabsorption coefficient $\tau$ increasing with a strong power of $\mathsf{Z}$ and decreasing with a strong power of $\mathsf{E}$ the X-ray energy

$$\tau \sim \frac{\mathsf{Z}^3}{\mathsf{E}^3}. \tag{2.8}$$

Besides photoabsorption, scattering processes attenuate X-rays passing through matter. In equation (2.7), the coherent and incoherent scattering are summed up in $\mu_S$. If a large group of electrons are involved in the process and the momentum transfer is balanced by an ensemble of atoms the scattering is coherent (Rayleigh scattering). This elastic process decreases with higher X-ray energies because its cross section includes the square of the atomic scattering factor f which falls off with increasing energy. The contribution of the coherent scattering to the attenuation is negligible compared to the strong photoabsorption in the same energy range. On the other hand, the incoherent scattering (Compton scattering) increases with increasing X-ray energy, so that it dominates the attenuation for large values of $\mathsf{E}$.

Figure 2.2 shows the different contributions in some typical lens materials. Displayed is the attenuation coefficient divided by the density of the material. This mass attenuation coefficient $\mu/\rho$ allows a correct comparison of the attenuation processes in different materials as a function of the X-ray energy. In figure 2.2(a) the contributions $\mu/\rho$ are plotted for beryllium. With increasing energy the total attenuation decreases since the photoabsorption falls off. The coherent scattering is negligible compared to the photoabsorption. At $8\,\text{keV}$, Compton scattering becomes more and more dominant in the total attenuation. The mass attenuation coefficient of other possible materials of refractive X-ray lenses[1] (Li, B, C, Si, Al, and Ni) are shown in figure 2.2(b). All total attenuation functions of the X-ray energy show the same influence of the attenuation contributions as discussed for Be, only the curves being basically shifted in energy. However, aluminium, silicon and nickel show absorption edges in the displayed energy region.

The strong attenuation of hard X-rays in matter favors elements with low atomic number $\mathsf{Z}$ as materials for refractive lenses. Obviously, the Compton scattering ultimately limits the transparency of refractive lenses. For this reason even the high absorbing nickel is considered as lens material for energies above $100\,\text{keV}$.

**Reflection:** at a boundary between two media a photon has a probability of being refracted and reflected. One consequence of the index of refraction being smaller than 1 is that X-rays show external total reflection. The critical angle at which this total reflection occurs is

$$\theta_{1c} = \sqrt{2\delta} \quad . \tag{2.9}$$

This angle is typically below $0.5°$. It follows that hard X-ray mirrors can only be used at grazing incidence.

---

[1] A general discussion of lens materials is given in appendix A.
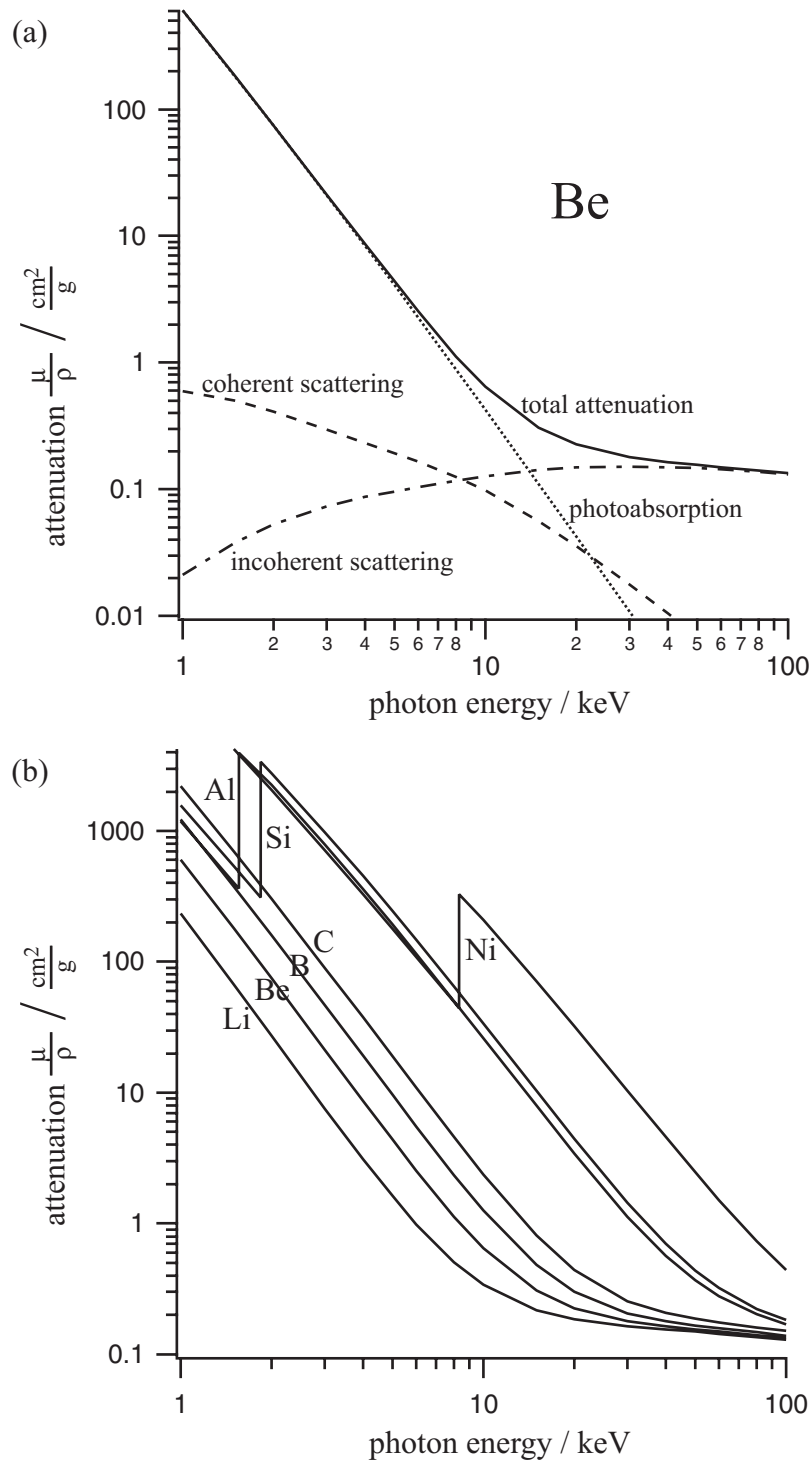
Figure 2.2: The mass attenuation coefficient $\mu/\rho$ in the range of $1\,\text{keV}$ - $100\,\text{keV}$ for different lens materials: (a) in Be, with the different contributions, and (b) for the possible lens materials Li, Be, B, C, Si, Al, and Ni. The data are taken from [4].

(a)

(b)
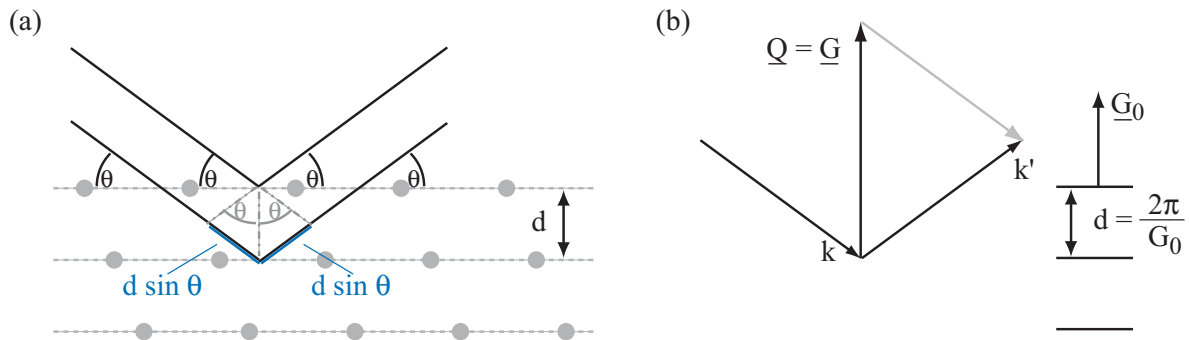
Figure 2.3: Bragg and Laue constructions for diffraction peaks. (a) The Bragg angle is half the angle by which the incident ray is deflected. (b) Laue condition $\underline{Q} = \underline{G}$.

**Diffraction:** if X-rays are scattered by a solid with translation symmetry pronounced peaks (Bragg peaks) occur when the condition

$$m\lambda = 2d\sin\theta \tag{2.10}$$

is fulfilled. Here, d is the distance of neighboring lattice planes. The wavelength of the photons $\lambda$ has to be in the order of the interatomic distances, a condition fulfilled for X-rays. Then, the path difference between two scattered rays is $2d\sin\theta$ where $\theta$ is the angle of incidence (figure 2.3a). The rays constructively interfere if this path difference is an integral number m of the wavelength. Translated into the Laue condition

$$\underline{Q} = \underline{G} \quad , \tag{2.11}$$

a Bragg refection occurs if the wave vector transfer $\underline{Q} = \underline{k}' - \underline{k}$ matches a reciprocal lattice vector $G = 2\pi m/d$, whose direction is perpendicular to the lattice planes (figure 2.3b). The Bragg and Laue expressions are equivalent. The positions of the Bragg peaks define the lattice structure, whereas the intensity of the peaks reflects the ions and their position in the unit cell of a crystal.

This is the basis for X-ray crystallography. Diffraction is also used in X-ray monochromators, as for a known lattice distance d photons of the energy $E = hc/\lambda$ are selected by the means of the Bragg angle $\theta$.

**Small Angle Scattering:** a perfect, rigid crystal will scatter all photons in the Bragg peaks but thermal vibrations broaden the peaks. Due to defects in the crystal the intensity of the peaks is diminished and intensity is generated between the Bragg peaks. A crystal mainly contains for instance point defects, impurities, dislocations, grain boundaries, precipitation, and voids. Small point defects produce diffuse scattering at all angles. The larger the inhomogeneities, the more scattering occurs in forward direction. This small angle scattering is shown in figure 2.4 as a function of the momentum transfer $\underline{Q}$.

$$|\underline{Q}| = \frac{4\pi}{\lambda}\sin\theta \tag{2.12}$$
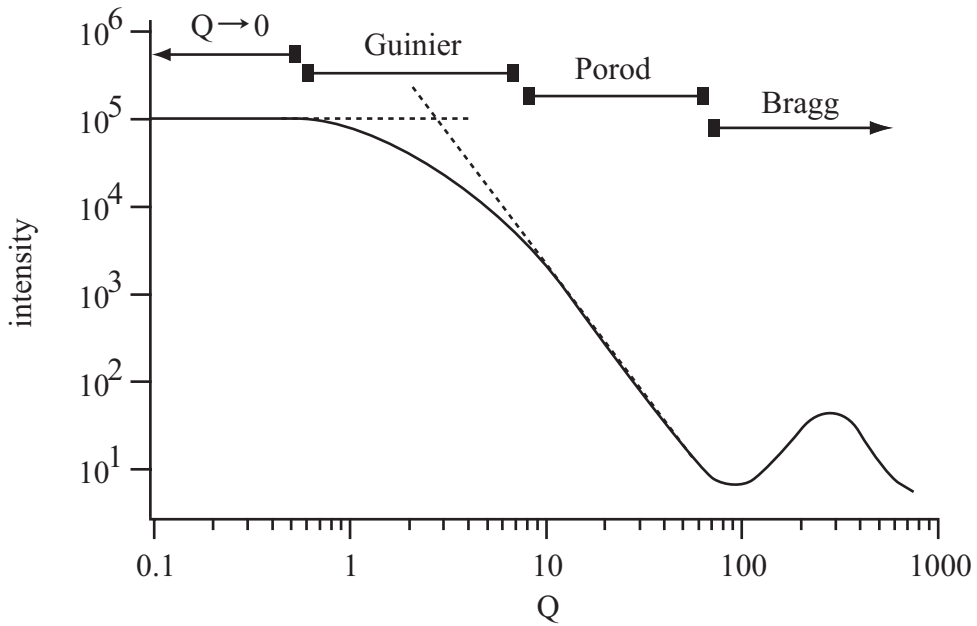
Figure 2.4: Intensity as a function of the momentum transfer $\mathbf{Q}$ for small angle scattering. Characteristic regions include structure information of the scattering material.

The scattering cross section

$$\frac{d\sigma}{d\Omega} = \left(\frac{d\sigma}{d\Omega}\right)_{Th} \cdot \left|\sum_j f_j e^{-i\underline{\mathbf{Q}}\cdot\underline{r}_j}\right|^2 \tag{2.13}$$

can be written for N inhomogeneities with a volume V and concentration c as

$$\frac{d\sigma}{d\Omega} = \left(\frac{d\sigma}{d\Omega}\right)_{Th} \cdot N\,V^2\,|\Delta\rho|^2\,F(\mathbf{Q}) \tag{2.14}$$

Both, the defects and the matrix in which they are embedded, are considered as homogeneous. The scattering of a single photon by a single electron is represented by the Thomson cross section $\left(\frac{d\sigma}{d\Omega}\right)_{Th} = r_0^2\,(\underline{e}_1 \cdot \underline{e}_2)$. The difference in the scattering amplitude of the matrix and the inhomogeneities is $\Delta\rho = n\,f - n_m f_m$. The structure factor of the inhomogeneity is

$$F(\mathbf{Q}) = \left|\frac{1}{V}\int_V d^3r\,e^{-i\underline{\mathbf{Q}}\underline{r}}\right|^2 \quad . \tag{2.15}$$

For a spherical particle of radius R it reads

$$F(\mathbf{Q}) = \left[3\,\frac{\sin QR - QR\cos QR}{(QR)^3}\right]^2 \quad . \tag{2.16}$$

With the equations (2.14 to 2.16) the different characteristic regions in figure 2.4 can be explained. In forward direction, when $\mathbf{Q} \to 0$, the structure factor becomes 1 and therefore the small angle scattering intensity is proportional to the constant product $N\,V$.

If the product $QR$ is smaller than unity (Guinier range) the structure factor can be expressed as $F(Q) = \exp(-\frac{1}{3}Q^2 R_G^2)$. For non-oriented defects $R_G$ is the Guinier radius defined as

$$R_G = \sqrt{\frac{n_1 + c^2}{n_2}} \cdot R \quad , \text{with}$$

| | $n_1$ | $n_2$ | c |
|---|---|---|---|
| sphere | 2 | 5 | 1 |
| cube | 2 | 3 | 1 |
| disc | 1 | 4 | 1 |
| needle | 1 | 12 | 0 |

$$(2.17)$$

The Guinier radius can be found from the slope of the logarithm of the scattering cross section plotted versus $Q^2$. If $QR$ is much larger than unity (Porod range) the scattering cross section of inhomogeneities with a sharply defined boundary is proportional to the total surface area of all inhomogeneities. At even larger scattering angles Bragg peaks can occur as indicated in figure 2.4.

## 2.2 Focusing Optics for Hard X-Rays

A brief presentation of the most common optical devices used at 3rd generation synchrotron radiation facilities follows.

**Optical elements based on total reflection**

Coated and uncoated mirrors are commonly used at synchrotron radiation facilities. In order to focus a mirror must be bent. Due to external total reflection an ellipsoid mirror focuses a point source in one focal point into the second focal point. Common mirrors have toroid shapes in the meter range to catch the beam under small angles. Significant progress in form fidelity and in surface finishing made them very common optical element for X-rays. The crossed geometry (KB-geometry) of two mirrors constitutes an X-ray microscope [5]. Further more, flat mirrors are used for eliminating higher harmonics in a beam monochromatized by Bragg reflection. This is possible because the critical angle for the total reflection is lower for higher order Bragg peaks.

Capillaries are hollow glass fibres which guide the X-rays by total reflection. A typical fiber has an opening of $\sim 50\,\mu$m and an exit of $\sim 1\,\mu$m - $0.1\,\mu$m in diameter, which increases the flux considerably. Even more intense micro beams were realized with poly-capillaries containing hundreds of individual fibres [6]. They are often used with X-ray tubes. For high energy X-rays (60 keV) lead glass capillaries have been used since they have a larger angle of total reflection [7].

**Optical elements based on diffraction**

Bragg reflection from crystals and multilayers is based on total reflection at lattice planes. However, the angle of total reflection is much larger than for mirrors. Crystals are used for synchrotron radiation monochromators, mainly as flat or bent double crystals. Multi-layers are artificial periodic structures. Both can focus a beam, in particular when implemented in KB-geometry.

Fresnel zone plates (FZP) were developed in 1974 [8]. They consist of concentric rings designed in a way that the transmitted radiation is interfering constructively in the focal point. With

higher energies the absorbing zones, which block the part of the beam that would destructively interfere, must become extremely thick. At the same time, their spacing gets narrower, considering their radius dependence on the wavelength $\lambda$ as $r_n = \sqrt{n\lambda z}$ with the distance between object and detector. The spatial resolution is limited by the width of the first zone $\sqrt{\lambda z}$. Therefore, the performance of FZP is limited by manufacturing zones with a high aspect ratio.

Efforts were made to operate FZP at higher energies. For that purpose, two zone plates were aligned to enhance the focusing effect [9]. By the same token multi-layer Fresnel zone plates were fabricated to operate in the energy regime from 25 keV - 100 keV [10]. Furthermore, phase FZP with multi levels zones were used to improve the efficiency [11].

## 2.3  Parabolic Refractive Lenses as Hard X-Ray Optic

Refractive lenses are a novel optical component for hard X-rays. They can be used above 5 keV where Fresnel zone plates become more and more inefficient. Unlike KB mirrors lenses have a straight optical path. In contrast to capillaries refractive lenses are designed for imaging, even up to high energies, like 120 keV.

### 2.3.1  Historical Note

X-rays were discovered in 1895 by W. C. Röntgen [12]. During the first experiments with X-rays, Röntgen has tried to focus them and found no visible effect. He was able to determine a refraction index below 1.05 for all analyzed materials and stated 'That with lenses one cannot concentrate X-rays.' The first observation of X-ray refraction was made by C. G. Barkla 1916 [13]. However, the value of the index of the refraction decrement $\delta$ were known not until 1948. Then P. Kirkpatrick and A. V. Baez discussed the possibilities of refractive lenses as 'a cumbersome and very weak system with poor transparency' [5]. They decided to use another method and implemented in a very successful way mirrors as optical elements for X-rays.

In the early 1990's the controversial discussion was continued [14, 15]. For the first time, in 1993, B. X. Yang theoretically introduced a parabolic design for refractive hard X-ray lenses [16]. Still, he proposed Fresnel lenses as 'superior focusing elements for hard X-rays', because of the fabrication difficulties for useful refractive lenses. The first refractive lenses for hard X-rays were reported 1996 [17]. The lenses were drilled holes, with a radius of 300 $\mu$m, in bulk aluminium with cylindrical or cross-cylindrical geometry. At 14 keV a spot size of 8 $\mu$m was measured. A patent on spherical refractive X-ray lenses was claimed by Tomie [18, 19, 20], in which the possibility to align many single refractive lenses was still precluded.

Experiments with stacked single parabolic refractive lenses were presented in 1999 [21], which discussed the optical properties of the lenses. The imaging abilities, even for hidden structures, were demonstrated with crossed gold meshes. Later, tomographic and microprobing applications were implemented [22, 23]. Beryllium parabolic refractive lenses were first manufactured in 2001 [24]. The concept of special refractive lenses for extreme nanofocusing has been the newest approach since 2003. The prototype of planar silicon parabolic refractive lenses is described in [25].

(1a) Single rotational parabolic lens

(1b) Stack of rotational parabolic lenses

1 mm

(2a) Single planar parabolic lens

(2b) Planar lens with many single parabolic lenses

0.05 mm
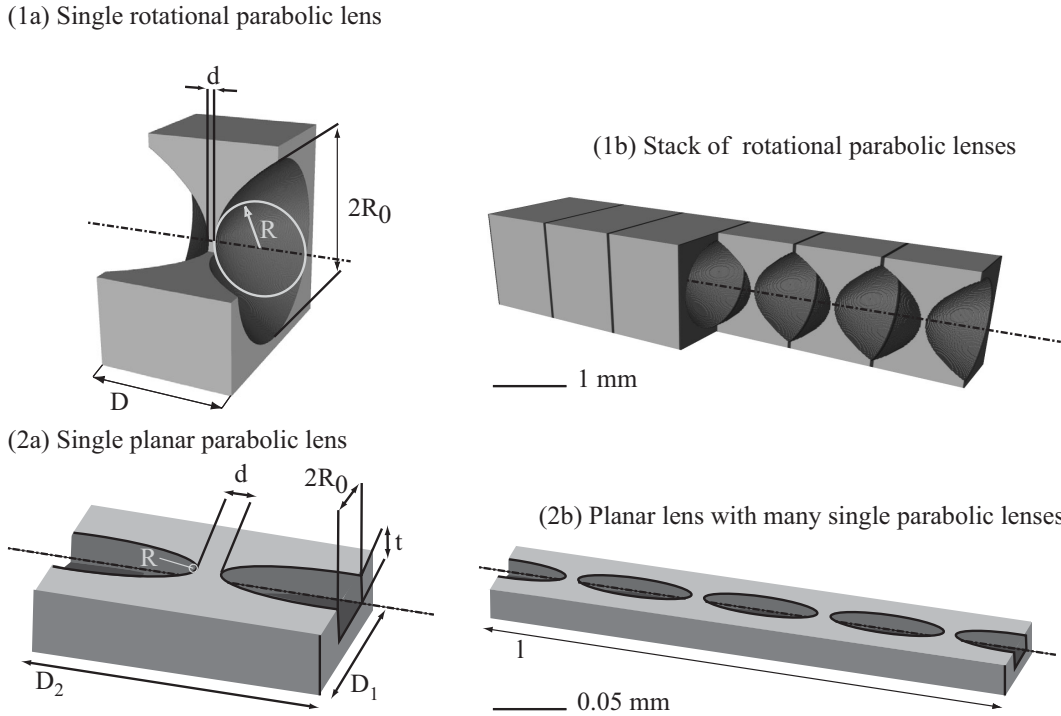
Figure 2.5: Sketch of types of parabolic refractive lenses.
(1) Rotational parabolic refractive lenses. Single lenses (a) with two pressed concave paraboloids aligned in one stack (b).
(2) Planar parabolic refractive lenses. Etched in one wafer, smaller parabolic single structures (a) can be implemented. The positioning of many lenses is included in the manufacturing.

### 2.3.2 Design

The microanalysis experiments presented in this thesis are based on parabolic refractive lenses for hard X-rays. Two types of lenses were designed and are under further development. The sketch in figure 2.5 illustrates their appearance. In both designs the lenses have a parabolic shape. In the following, such a profile is defined by the radius $R$ at the apex of the parabola. Each single lens has two concave parabolic surfaces with a minimal distance $d$ between each other. The slight focusing effect due to the weak refraction of hard X-rays of one lens is compensated by stacking many lenses in a row.

The first type of lenses 2.5(1) is realized in aluminium and beryllium. These lenses are rotationally parabolic. A high precision CNC lathe allows for the manufacturing of pressing tools for these lenses with parabolic radii $R$ between $80\,\mu$m and $300\,\mu$m. Apertures between $2R_0 = 850\,\mu$m and $1.2$ mm can be achieved. For stacking the lenses a specially designed holder is used to perform an alignment with an accuracy of few micrometer.

The second type of parabolic refractive lenses is planar, figure 2.5(2). Using silicon micromachining, shapes of lenses with parabolic radii $R$ of $1\,\mu$m - $3\,\mu$m were manufactured. Typically, a single lens is placed on a field $D_1 \times D_2$ of $41\,\mu$m $\times 82\,\mu$m. The depth $t$ should be equal to their maximal aperture of $2R_0 \simeq 36\,\mu$m. The manufacturing allows the use of one silicon wafer for a high number of single lenses figure 2.5(2b). Reasons for the different designs will

be given in the next chapters. Obviously, the rotationally parabolic refractive lenses provide a point focus and a high quality imaging optic, whereas the planar lenses generate a thin line focus.

### 2.3.3   Principal Geometries

Parabolic refractive lenses for hard X-ray generate a straight optical path. The optical geometries are similar to the optics of visible light using glass lenses. In figure 2.6(1)-(4) are illustrated the main application schemes. The stack of lenses is symbolically represented by two parabolic shapes.
(1) First, an analytical microprobe is realized if the synchrotron radiation source itself is imaged by the refractive lenses. The distance source-lens $L_1$ is chosen long, normally between 30 m and 70 m. Many single refractive lenses are used in order to shorten the focal length $f$ in a strongly demagnifying mode. Photons of the beam are focused to a small intense spot at the image distance $L_2$ which defines the spatial resolution in scanning analytical methods. In an imaging setup an object is illuminated by the source. Usually the length $L_0$ is given by the beamline design. (2) The second geometry illustrates that a short focal length $f$ and a long image-distance $L_2$ lead to a strong magnification of the sample. This is the concept for a hard X-ray microscope. (3) On the other hand, a short focal length $f$ and a long distance between the object and the lens $L_1$ allow a demagnification of the sample, e. g. a mask for X-ray lithography, which is shown in the third geometry.
(4) Finally, in the forth geometry a few single lenses can generate an X-ray beam with much less divergence than without the refractive lenses. Therefore, the objective must be located approximately in a distance of its focal length from the source. Such a geometry is helpful for example in small angle scattering experiments.

(1) imaging the source

$L_1$    $L_2$

(2) magnifying an illuminated object

f

$L_0$   $L_1$    $L_2$

(3) demagnifying an illuminated object (mask)

f

$L_0$   $L_1$    $L_2$

(4) making the beam parallel

$L_2 = f$
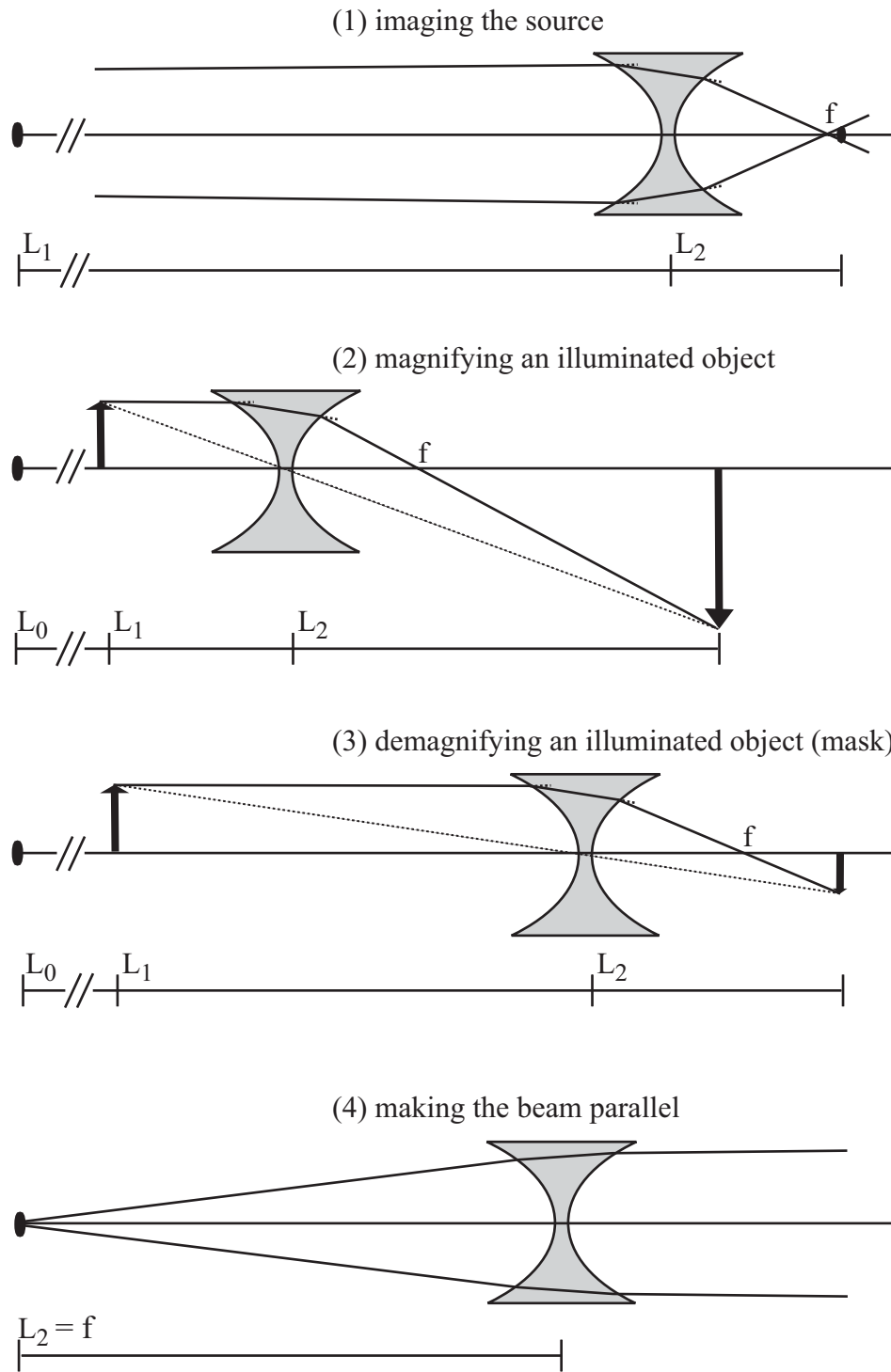
Figure 2.6: Principal geometries in which parabolic refractive X-ray lenses are used.

# Chapter 3

# Parabolic Refractive Lenses: Properties

## 3.1 Parabolic Shape

The shape of refractive lenses is of utmost importance. Classical optics in the Gaussian approximation are based upon the assumption that the incident angle $\Theta$ to the surface normal is small enough for the approximation $\Theta \approx sin\Theta \approx tan\Theta$ to be valid. Linearizing requires that all refracting surfaces are almost normal to the optical axis. This requires radii $R$ of the lenses large compared to the geometrical aperture $2R_0$. This assumption is not valid for hard X-ray lenses.
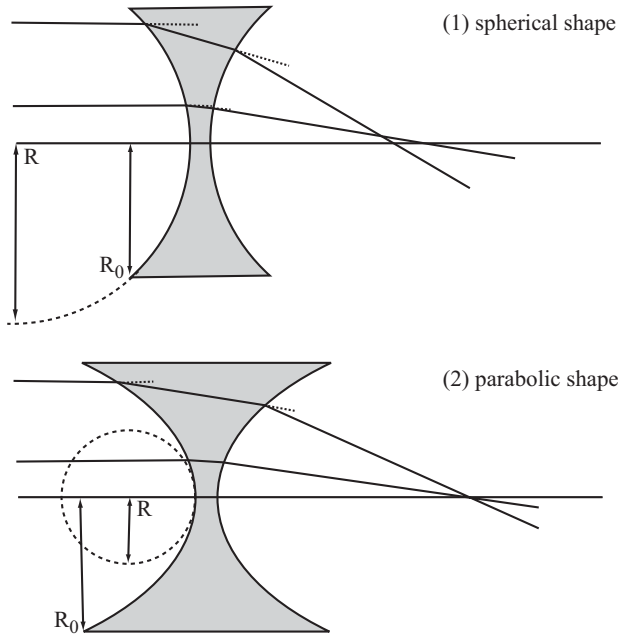


Figure 3.1: The compensation of spherical aberration by a parabolic lens shape. (1) A bundle of rays entering a spherical lens parallel to the optical axis does not meet in one point. (2) For a parabolic shape the refraction of outer rays is weaker. All rays meet in the focal spot.

The radii of refractive lenses are in the range of $1\,\mu m$ - $500\,\mu m$ and are comparable to the apertures of $10\,\mu m$ - $1.4\,mm$. Figure 3.1(1) demonstrates the origin of spherical aberration, if the Gaussian approximation is not fulfilled. Rays which enter the lens far from the center are stronger refracted than rays which are close to the optical axis. A parabolic shape like figure 3.1(2) compensates for this. A bundle of rays entering a parabolic lens parallel to the optical axis is focused on the focal spot in excellent approximation.
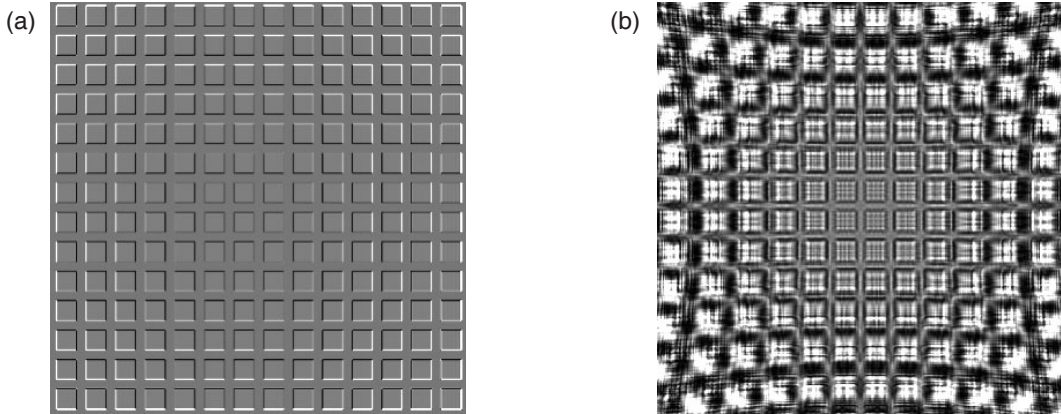


Figure 3.2: Numerically generated images of a Ni mesh (2000mesh) in a one to one geometry at $25\,keV$ using 120 Al lenses with (a) perfect parabolic shape and (b) spherical shape.[26]

A reliable verification of the shape of a refractive lens for hard X-rays is their imaging quality. Form errors of the lenses results in aberrations of the image. Simulated images in figure 3.2 show the effect of different lens shapes. The specimen is a Ni mesh with 2000 grids per inch. The regular $12.7\,\mu m$ period can be correctly imaged with parabolic refractive lenses, but not with spherical lenses. Figure 3.2(b) illustrates the limits of the spherical approximation in case of refractive lenses for hard X-rays. There are artefacts and distortions everywhere in the image.

## 3.2   Surface Roughness

The surface roughness $\sigma$ is the root mean square deviation from the ideal surface. It has an influence on the transmission amplitude of the electromagnetic wave propagating through a lens, according to an exponential damping factor $\exp\left(-Q^2\sigma^2\right)$, which is depending on the momentum transfer $Q$.
The momentum transfer at a lens surface at normal incidence is

$$Q_0 = k \cdot \delta \simeq k \cdot 10^{-6}. \tag{3.1}$$

Considering the root mean square roughness $\sigma$, the transmission of a lens composed of $N$ single lenses will be reduced by the exponential factor $exp(-2NQ_0^2\sigma^2)$, because the roughnesses of different lenses are not correlated. Since each lens has 2 parabolic surfaces, the effective roughness is $\sqrt{2N}\sigma$ for $N$ lenses. A comparison of the roughness for a lens($l$) and a mirror($m$) resulting in the same damping gives

$$\sigma_m = \sigma_l \sqrt{2N}/2\vartheta; \quad \text{in case of } (N = 100) \Rightarrow \sigma_m = 2 \cdot 10^{-3}\sigma_l \quad . \tag{3.2}$$
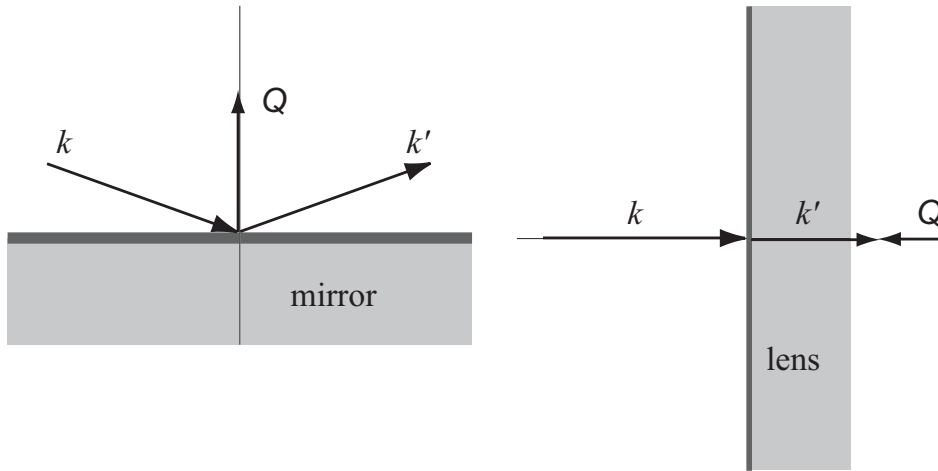
Figure 3.3: Momentum transfer in case of a mirror and of a lens.

The incident angle $\vartheta$ for totally reflecting mirrors is about $\vartheta = 0.2°$. Refractive lenses are less sensitive to surface roughness by 3 orders of magnitude compared to mirrors. This is a consequence of the higher momentum transfer for a mirror compared to a refractive lens, as demonstrated in figure 3.3.

The weak sensitivity to roughness is important for manufacturing refractive lenses. For a rotational lens with a radius $R \simeq 200\,\mu m$ a roughness smaller than $1\,\mu m$ rms barely deteriorates the lens performance if the shape is still parabolic. Considering the smaller dimensions of a planar lens, the roughness has to be below $100\,nm$.

## 3.3    Focal Length

For a concave thin lens with parabolic radius $R$ on both sides the focal length $f_0$ is

$$f_0 = \frac{R}{2N\delta} \cdot [1 + O(\delta)]. \tag{3.3}$$

The focal length is proportional to the parabolic radius $R$ and can be reduced by increasing the number of lenses $N$ [21]. The energy dependence of the focal length (chromatic aberration) is hidden in the index of refraction decrement $\delta$ introduced in equation (2.3).

The focal length $f_0$ for parabolic refractive lenses uses the thin lens approximation [27]. This assumption is no longer justified for the short focal distances achieved recently [23]. The propagation of a ray through an axially symmetric system of lenses is described by a transfer matrix formalism [2]. A ray is characterized as its distance $y$ from the optical axis and its slope with respect to the optical axis, the inclination $\Theta$. A matrix $T_{01}$ describes the propagation from the initial position $(y_0,\Theta_0)$ to a final position $(y_1,\Theta_1)$:

$$T_{01} \begin{pmatrix} y_0 \\ \Theta_0 \end{pmatrix} = \begin{pmatrix} y_1 \\ \Theta_1 \end{pmatrix}.$$

Each single lens has the focal distance $f_s = R/2\delta$. This is expressed by the transfer matrix for the refraction $T_{f_s}$. Two single lenses are separated by $\Delta l$ which leads to the transfer matrix

for the translation $T_{\Delta l}$ :

$$T_{f_s} = \begin{bmatrix} 1 & -\frac{1}{f_s} \\ 0 & 1 \end{bmatrix} \qquad \text{and} \qquad T_{\Delta l} = \begin{bmatrix} 1 & 0 \\ \Delta l & 1 \end{bmatrix}.$$

Considering the lens setup, the ordered product

$$T_{01} = T_{\Delta l/2}(T_{f_s}T_{\Delta l})^{N-1}T_{f_s}T_{\Delta l/2}$$

defines the propagation and refraction through a system of $N$ lenses. The minimal situation with only one lens correctly gives $f_s$ as result. Additional lenses displace the focus to a longer distance than in the uncorrected case. With the overall length of the lens $l$ one obtain for the focal distance approximately [23]

$$f \simeq f_0 + \frac{l}{6}. \tag{3.4}$$

## 3.4   Transmission and Gain

Little absorption is a criterion of high priority and the mayor reason for beryllium as lens material. But refraction and transmission are largely contradictory requirements. The gain is the appropriate quality parameter.

The transmission $T$ through the geometrical aperture of a rotational parabolic refractive lens is

$$T = \frac{R}{\mu NR_0^2}(1 - e^{-\mu NR_0^2/R}) \cdot e^{-\mu Nd} \tag{3.5}$$

$$= \frac{1}{(\mu/\delta)} \cdot \frac{\left(2f - \frac{l}{3}\right)}{R_0^2} \cdot \left(1 - e^{-(\mu/\delta)\cdot R_0^2/(2f - \frac{l}{3})}\right) \cdot e^{-(\mu/\delta)\cdot R\, d/(2f - \frac{l}{3})} \tag{3.6}$$

In equation (3.6) the number $N$ of single parabolic refractive lenses is expressed in terms of the modified focal distance, equations (3.4) and (3.3). For a given energy, the transmission $T$ depends mainly on the ratio $\mu/\delta$ which is displayed in figure 3.4.
For a fixed focal distance, say $2.5\,\text{m}$ , and a parabolic lens radius of $R = 200\,\mu\text{m}$ for all lens materials there is an energy for maximal transmission which increases with $Z$ [$E_{Tmax}(\text{Be}) = 11\,\text{keV}$, $E_{Tmax}(\text{Al}) = 42\,\text{keV}$, and $E_{Tmax}(\text{Si}) = 48\,\text{keV}$].
We now consider planar parabolic refractive lenses. Their transmission is

$$T_c = \frac{R}{2\,\mu NR_0^2} \cdot e^{-\mu N\left(\frac{R_0^2}{R} + d\right)}. \tag{3.7}$$

Obviously, the transmission for a cylindric lens is better than for a parabolic one. However, its focusing ability is poorer. The gain $g$ is the quality parameter which takes the transmission and focusing into account.

The gain $g$ is a dimensionless parameter which puts the performance in relation to a hypothetical pinhole of the size of the focal spot [28].

$$g = \frac{4R_0^2 T}{B_v B_h} \tag{3.8}$$
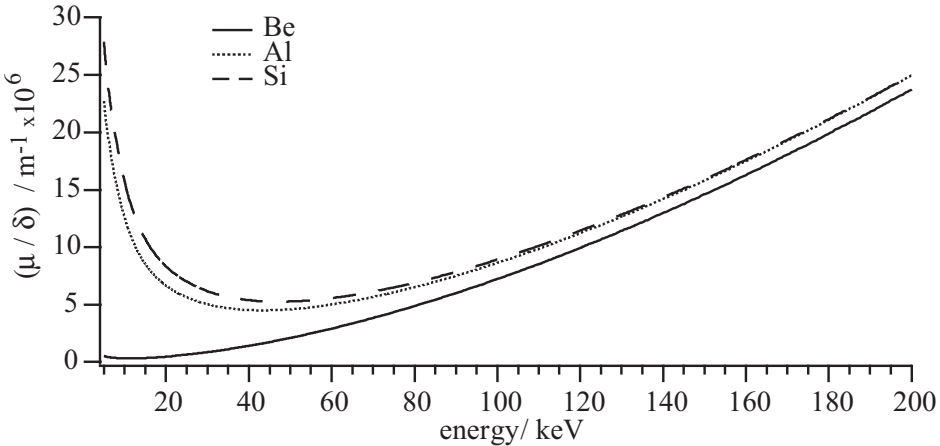
Figure 3.4: The variation of $(\mu/\delta)$ with the photon energy for the lens materials Be, Al, and Si. This parameter is mainly responsible for the transmission of X-rays through a refractive lens.

The focusing performance of the optical element is described by the size of the image. This focal spot $(B_v \times B_h)$ is the image of the elliptical shape of a synchrotron radiation source. Gains up to more than 10 000 can be achieved.

Geometrical aspects, which do not directly depend on the lens performance, have a strong impact on the gain. Figure 3.5 illustrates this for $N = 95$ Al lenses with $R = 200\,\mu$m at $E = 20\,$keV and different distances between source and lens $L_1$ as well as different source sizes.
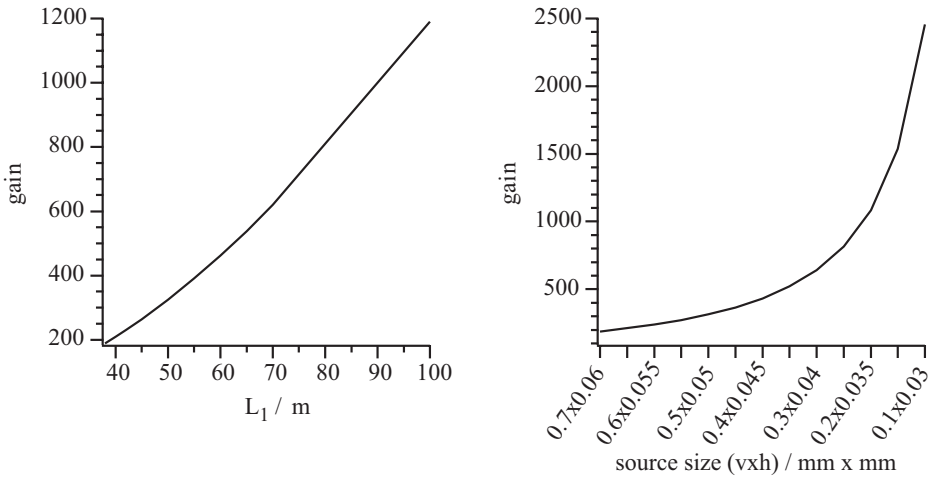


Figure 3.5: Parameters influencing the gain which are independent of the lens design: the gain increases with increasing source-lens distance $L_1$ (left) and with decreasing source size (right).

## 3.5    Effective and Numerical Aperture

The absorption of X-rays is not negligible for refractive lenses. Therefore, the geometrical aperture $2R_0$ is larger than the effective aperture $D_{eff}$

$$D_{eff} = \sqrt{\frac{2R}{\mu N}}. \tag{3.9}$$

The numerical aperture N.A. is

$$\text{N.A.} = \frac{D_{eff}}{2L_1} \quad . \tag{3.10}$$

The object-lens distance $L_1$ in imaging setups is of the order of $1\,\text{m}$ and $D_{eff}$ is about $0.5\,\text{mm}$. This results in a small numerical aperture of order $10^{-4}$ to $10^{-3}$.

## 3.6    Depth of Field and Depth of Focus

The depth of field $d_l$ is defined as the distance of two object points along the optical axis which can be correctly immaged.

$$d_l = \frac{8}{\pi}\lambda\frac{L_1}{D_{eff}^2} = \frac{2}{\pi}\frac{\lambda}{(\text{N.A.})^2} \tag{3.11}$$

The low values of N.A. make $d_l$ large. For tomography this is very advantageous. A microbeam generated by refractive lenses has a large depth of focus DoF [23] which is defined as the beam length where the lateral beam size is smaller than $\sqrt{2}\,B_{v,h}$.

$$\text{DoF} = \frac{4\,B_{v,h}}{2\sqrt{2\,ln(2)}} \cdot \frac{L_2}{D_{eff}} \tag{3.12}$$

Samples of millimeter size can be analyzed because the probing beam has the same size throughout the whole sample.

## 3.7    Resolution

The transversal resolution $d_t$ is very important in imaging. It is the distance of two lateral points of the object whose image points are separated by the FWHM of each image.

$$\begin{aligned}
d_t &= \frac{2\sqrt{2ln(2)}}{\pi} \cdot \frac{\lambda L_1}{D_{eff}} \tag{3.13}\\[2mm]
&= 0.75 \cdot \frac{\lambda}{2\,\text{N.A.}} \tag{3.14}
\end{aligned}$$

The value is dominated by the small numerical aperture of refractive lenses which is due to the high attenuation of X-rays in the lens materials. But $d_t$ depends only linearly on N.A. in contrast to the longitudinal resolution $d_l$ which contains the square of N.A.

Equation (3.13) is valid for incoherent illumination. A coherent illumination deteriorates the resolution due to the amplitude interferences of neighboring parts of the image: $d_t^{coh} = \sqrt{2}d_t^{incoh}$ for parabolic refractive lenses [21, 29].

## 3.8 Chromatic Aberration

In many cases parabolic refractive lenses are used with monochromatic radiation. The desired focal length for one specific energy is adjusted by the lens material, the number of single lenses, and/or their radius of curvature. But there are some applications for which monochromatic radiation is not adequate. For example, a wider energy bandwidth results in more flux. Al refractive lenses were already used for such a 'pink beam' [23]. An other example is the element specific analysis of the absorption fine structure for which the energy has to be tunable (chapter 5). The energy dependence of the focal distance of parabolic refractive lenses was shown above, equations (2.3) and (3.3). It is apparent that refractive lenses suffer from chromatic aberration. With equation (2.3) the change of the index of refraction decrement $\Delta\delta$ can be calculated.

$$\Delta\delta = -\frac{1}{2\pi}N_A r_0 \frac{2h^2 c^2}{E^3} \cdot \frac{Z + f'}{A} \cdot \Delta E = -\frac{2\,\delta(E_0)}{E_0}\Delta E \tag{3.15}$$

This can be translated into a change of the focal distance. Assuming the thin lens approximation,

$$\Delta f = -\frac{R}{2N\delta^2} \cdot \left(-\frac{2\delta}{E_0}\right) \cdot \Delta E = 2f_0 \cdot \frac{\Delta E}{E_0} \quad . \tag{3.16}$$

In case of a pink beam the band width $\Delta E/E$ is typically 1% resulting in a flux gain of 100 in comparison to a typical monochromatic beam at an undulator source with an energy resolution of $\Delta E/E = 10^{-4}$. The chromatic aberration will be noticed when the change in focal distance, translated into a change in image distance, is larger than the depth of focus in a microprobing experiment. For instance in a microfocus setup using a pink beam the chromatic aberration is negligible [23], however for the analysis of absorption fine structures it is not (details in chapter 6).

The chromatic aberration of refractive lenses limits the experimental possibilities of some applications. In the optics of visible light the problem of chromatical aberration can be solved by an achromate. Therefore, two lenses with different optical parameters are combined to compensate the chromatical aberrations of each other. This is achieved by using different indices of refraction and different variation of the index with energy. However, this condition cannot be realized for X-rays as shown in figure 3.6. Illustrated is this for the lens materials Li, Be, B , Al, Si, Ni and as high Z example for Pt. Whereas the absolute values of $\delta$ differ for the materials the slopes of the curves are the same. If the values are corrected due to the density of the elements, there are only slight differences (figure 3.6right). To sum up, an achromate lens system, which is common for visible light, is not realizable for hard X-rays.

It would be possible to move the lens along the optical axis to hold the focal spot on place during tuning the energy. Such an implementation demands extreme requirements for the lateral stage movements in terms of accuracy and velocity. The necessary efforts would implicit a permanent installation at one beamline. A defined changing of single lenses would be a second possible approach. Rotational Al or Be lenses with different but defined parabolic radii R are beyond our manufacturing abilities, today. In case of planar lenses this can be accomplished. But again, only a permanent installation can legitimate such efforts.
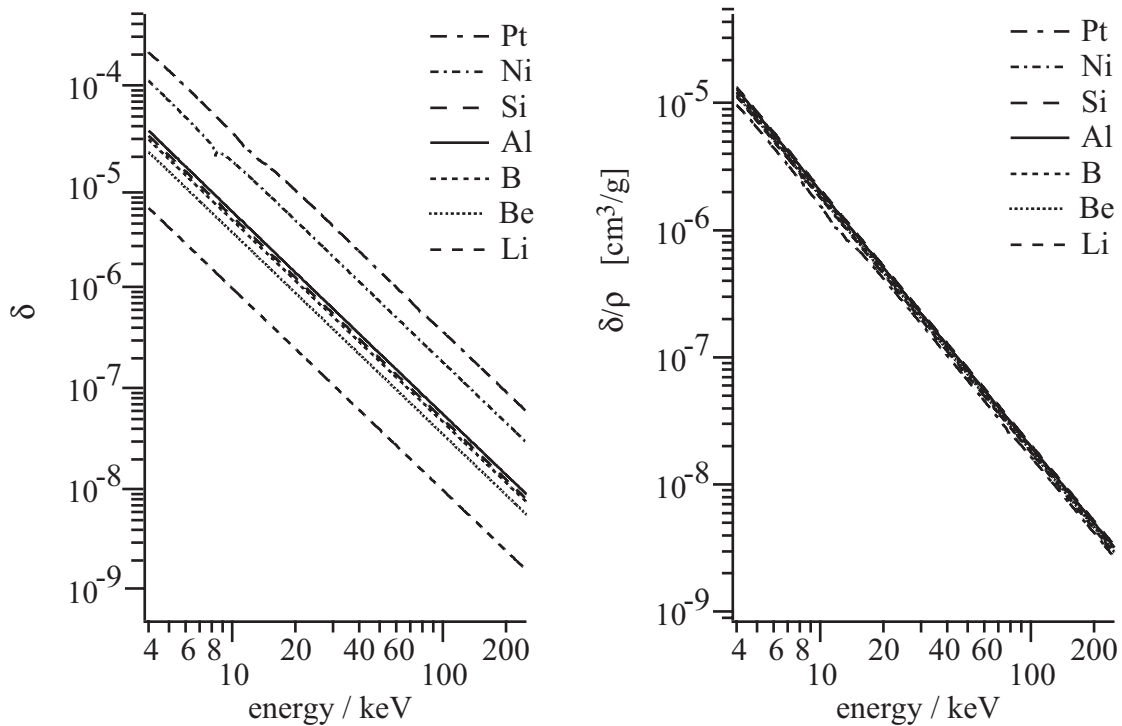
Figure 3.6: The index of refraction decrement $\delta$ at different energies for common materials. (Left) The values of $\delta$ for the lens materials (Li, Be, B, Al, Si, Ni) and Pt, as example for a high $Z$ element, in the hard X-ray region (4 keV - 250 keV). (Right) The mass index of refraction decrement $\delta/\rho$ for the same materials.

## 3.9　Example: Imaging a Synchrotron Radiation Source in a Typical Geometry.

As an example we consider now a microbeam setup to image a synchrotron radiation source on a sample which can be used as micro probe (figure 2.6). A common lens material is aluminium.

| material | aluminium | $Z = 13$ |
|---|---|---|
| density | | $\varrho = 2.7 \, \text{g/cm}^3$ |
| atomic mass | | $A = 26.98 \, \text{g/mol}$ |

The microbeam setup presented here can be used for fluorescence analysis, which requires an incident beam of typically $E = 20 \, \text{keV}$. The first experiments with parabolic refractive Al lenses were done with the undulator source of the beamline ID22 at the European Synchrotron Radiation Facility, ESRF.

| synchrotron source | ESRF/ID22 undulator | |
|---|---|---|
| | source size horizontal | $700 \, \mu\text{m}$ |
| | vertical | $60 \, \mu\text{m}$ |
| | divergence horizontal | $30 \, \mu\text{rad}$ |
| | vertical | $30 \, \mu\text{rad}$ |

The space available in an experimental hutch at a synchrotron radiation facility is limited and a focal length of up to $2\,$m is common. If we assume $1\,$m, we need at least $\mathsf{N}=75$ single lenses with a radius of $\mathsf{R}=200\,\mu$m. In general the maximal number of Al lenses is $\mathsf{N}=300$ in one holder, but the alignment of two holders is not more complicated than the alignment of one. The radius $\mathsf{R}$ is a key value, which is determined by the manufacturing possibilities.

| refractive lenses | | |
|---|---|---|
| | number | $\mathsf{N}=75$ |
| | apex radius | $\mathsf{R}=200\,\mu$m |
| | minimal thickness | $\mathsf{d}=10\,\mu$m |
| | geometrical aperture | $2\mathsf{R}_0=850\,\mu$m |

Due to the beam divergence, the geometrical aperture of the lenses of $2\mathsf{R}_0=850\,\mu$m is completely illuminated by the beam at $\mathsf{L}_1=42\,$m distance from the synchrotron radiation source.

| geometry | | |
|---|---|---|
| | lens position at | $\mathsf{L}_1=42\,$m |
| | image position at | $\mathsf{L}_2=1.0023\,$m |
| | focal length | $\mathsf{f}_0=0.999\,$m |
| | focal length corrected | $\mathsf{f}=1.012\,$m |
| | effective aperture | $\mathsf{D}_{\mathsf{eff}}=152\,\mu$m |
| | numerical aperture | $\mathsf{N.A.}=0.000074$ |
| | resolution | $\mathsf{d}_t=0.312\,\mu$m |

The correction of the focal length $\mathsf{f}_0$ is required for Be and Si lenses, whose performance in microanalytical experiments will be discussed in the following chapters. But even for 75 Al lenses the effect of a thick lens is visible since the approximate focal distance of $0.999\,$m is extended to $1.012\,$m. But the depth of focus with $17.061\,$mm for the microbeam is still larger than the correction of $13\,$mm. This changes if $\mathsf{N}\geq 85$ Al lenses are stacked and the effect of a thick lens is not compensated by the depth of focus anymore, if all other parameters are the same.

The transmission through the lenses would be only 0.7%. It implies that for Al lenses an energy of $20\,$keV is at the lower working range. The development of Be lenses improves this performance. Nevertheless, a gain of 227 compared to a hypothetical pinhole of the spot size can be accomplished, here. The achieved spot size of $17.5\,\mu$m horizontal to $1.5\,\mu$m vertical corresponds to a 40 fold demagnification of the source.

| performance | | |
|---|---|---|
| | transmission | 0.7% |
| | spot size horizontal | $17.5\,\mu$m |
| | spot size vertical | $1.5\,\mu$m |
| | gain | 227 |
| | depth of focus | $17.061\,$mm |

The depth of focus of the microbeam would compensate a chromatic aberration over a range of $200\,$eV around $20\,$keV.

# Chapter 4

# Beryllium Parabolic X-Ray Lenses: Properties and Performance

For hard X-ray microscopy and microanalysis, aluminium lenses have given good results which are in remarkable agreement with their expected theoretical performance. But these optics cannot be used below 18 keV due to a low transmission of 1 % and smaller. In chapter 2.1 the mass absorption coefficient $\mu/\rho$ was considered to illustrate the influence of photoabsorption and scattering inside the lens material. The plot of the mass absorption coefficient for different materials versus the energy in figure 2.2 favors materials with low atomic number Z. The solid with the lowest attenuation is lithium, but its high reactivity makes lenses of Li hard to handle and its low density results in a weak refraction. Therefore, efforts were made to manufacture parabolic refractive lenses from beryllium in order to improve the microanalysis with parabolic refractive lenses with hard X-rays, figure 4.1. This chapter discusses in detail the reasons for this choice of lens material and demonstrates the improvements which can be expected. The applications, which benefits of refractive Be lenses, will be discussed in the next chapters.
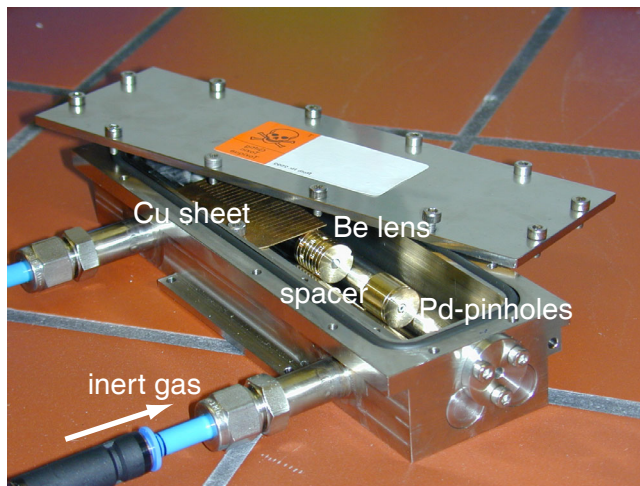


Figure 4.1: Lens holder with Be lenses and additional assembling features.

## 4.1   Improvements due to Beryllium

In the following, the properties of refractive beryllium lenses are discussed. Calculations and experimental results are compared with aluminium lenses.

**Transmission**
Beryllium is the best candidate to improve the transmission of parabolic refractive lenses due to its low atomic number $Z = 4$. Table 4.1 gives some values for the transmission through Al and Be lenses for different energies. Regarding the energy dependence of the mass absorption coefficient $\mu/\rho$ a good working energy for Al lenses is $\sim 40\,\text{keV}$ whereas for Be lenses it is $\sim 12\,\text{keV}$. Nevertheless, both materials can be used at $20\,\text{keV}$. It is evident that the performance of both lens materials is similar at their best working energies. The decrease of transmission with a higher number $N$ of single lenses is stronger in case of Al lenses. In particular, at $20\,\text{keV}$ the different increase of attenuation is evident. In case of 100 single Al lenses the transmission is below $0.5\,\%$, whereas for Be lenses this value is still above $10\,\%$.

Table 4.1: Exemplar transmission values for objectives build of parabolic refractive lenses. The lens materials aluminium and beryllium are compared.

|         | Al at $40\,\text{keV}$ | Al at $20\,\text{keV}$ | Be at $20\,\text{keV}$ | Be at $12\,\text{keV}$ |
|---------|---------|---------|---------|---------|
| $N = 1$ | $92.7\,\%$ | $65\,\%$ | $96.7\,\%$ | $93.6\,\%$ |
| 10      | $50.8\,\%$ | $10\,\%$ | $72.5\,\%$ | $55.2\,\%$ |
| 50      | $12.2\,\%$ | $1.4\,\%$ | $27.9\,\%$ | $14.1\,\%$ |
| 100     | $5.7\,\%$ | $0.4\,\%$ | $13.8\,\%$ | $6.4\,\%$ |
| 150     | $3.51\,\%$ | $0.18\,\%$ | $8.8\,\%$ | $3.9\,\%$ |
| 185     |  |  | $7\,\%$ | $3\,\%$ |
| 300     | $0.014\,\%$ | $0.023\,\%$ |  |  |

It has to be mentioned, that even for the worst listed transmission it is possible to perform microanalysis experiments with parabolic refractive lenses at 3rd generation synchrotron radiation facilities.

**Effective and numerical aperture**
For Al lenses $D_{\text{eff}}$ is always smaller than the geometrical aperture $2R_0$. A parabolic radius $R = 200\,\mu\text{m}$ pressed from two sides in a $1\,\text{mm}$ thick piece of lens material results in a geometric aperture of $\sim 850\,\mu\text{m}$. Due to the high absorption in aluminium no more than $400\,\mu\text{m}$ were needed for all accomplished experiments. The optimal transmission of beryllium allows the use of a larger lens area. In general, it is $400\,\mu\text{m} < D_{\text{eff}} < 850\,\mu\text{m}$ and the manufactured apertures does not reduce the lens performance. In chapter 5 a special experimental geometry with an effective aperture $> 1\,\text{mm}$ is described. In such a case lenses with $D = 2\,\text{mm}$ thick raw material can be processed which results in a geometrical aperture of $1.2\,\text{mm}$. Due to equation (3.10), the numerical aperture is proportional to $D_{\text{eff}}$. Hence, in the following discussion we consider the behavior of the numerical aperture.
In figure 4.2 we consider lenses with a fixed focal length of $2.5\,\text{m}$ generated by a realistic number $N$ of single lenses with $N(\text{Be}) = 185$ and $N(\text{Al}) = 300$. It was assumed that Li lenses have the same design as Be lenses and that Ni lenses are equal in design to Al lenses. A distance of

40 m from the source $L_1$ was chosen. With these parameters the numerical apertures versus the energy was calculated, figure 4.2(left). For Be the maximal N.A. occurs at 11 keV. At this point, the value is 5.6 times larger than the numerical aperture of Al lenses and 16.6 times larger than of Ni lenses.
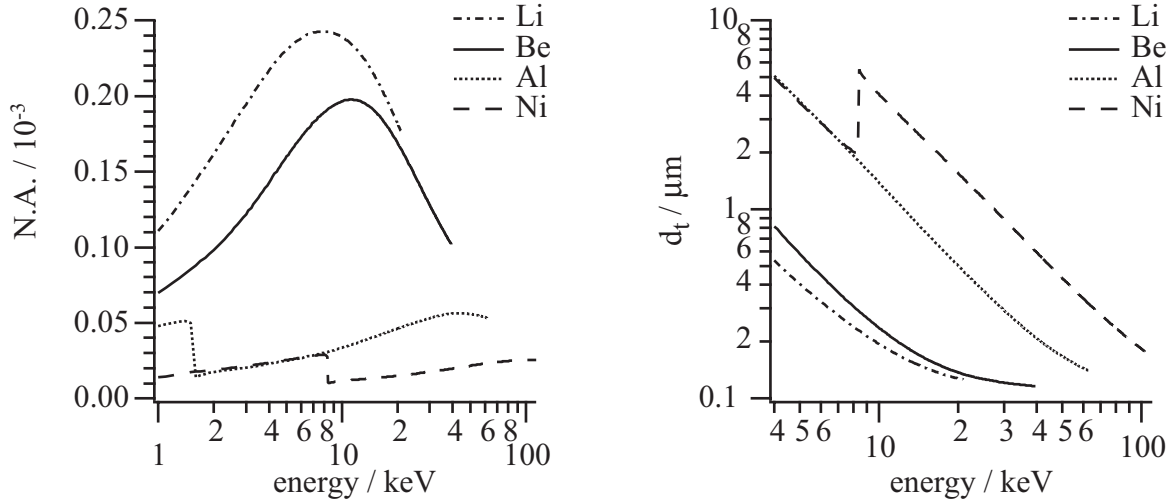


Figure 4.2: For the fixed focal length of 2.5 m, the calculated numerical aperture N.A. and the lateral resolution $d_t$ is plotted versus X-ray energies. The values for Be are compared with those of Al, Li or Ni.

Equation (3.13) gives the lateral resolution $d_t$ in terms of the N.A. Likewise, in figure 4.2(right) the results for N.A. are transferred into values of the resolution. In this context the benefits of Li are no longer important. Indeed, each value of $d_t$ for Li can be reached with Be lenses, too, just by increasing the energy by less than 1 keV. All presented types of lenses can reach a resolution $d_t$ below 200 nm. In particular, this is true for energies higher than 9.7 keV in case of Li, >11.8 keV for Be, >41.4 keV for Al, and >92.1 keV for Ni.

Both, the numerical apertures and the resolution in figure 4.2, indicate a more general aspect for refractive lenses. Be lenses are an improvement, but only for energies up to ~40 keV. Above, the handling in number and the overall length of the lens system make Al lenses more favorable and for the highest energies even Ni lenses should be considered.

**Field of view, FoV**
The field of view is an essential parameter for all imaging purposes. The pronounced low divergence of synchrotron radiation makes the effective aperture $D_{eff}$ an appropriate parameter for the FoV. For the experiments in figure 4.3(a) and (b) Al and Be were used, respectively. Each experimental setup was optimized for the used lens material, resulting in an effective apertures at 162 $\mu$m for Al lenses and 463 $\mu$m for Be lenses, but the measured field of views were lower (FoV$_{Al} \cong 130\,\mu$m and FoV$_{Be} \cong 450\,\mu$m). Hence, the scattering and absorption within the lenses need to be improved further on.

The field of view of Be lenses is larger by a factor 3.5 compared to the value for Al lenses. The Be lenses reached 97 % of its effective aperture. So the estimated improvements in the field of view due to Be are similar to the improvement of the effective apertures in figure 4.4.
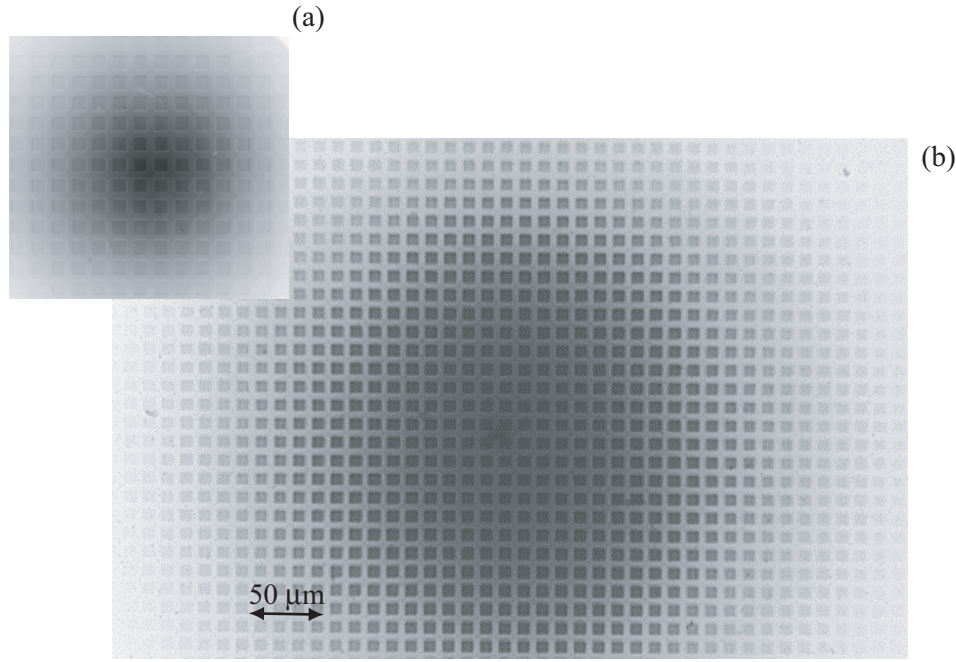
Figure 4.3: Measured field of view for (a)Al and (b)Be parabolic refractive X-ray lenses. An improvement is visible from $130\,\mu$m to at least $450\,\mu$m.
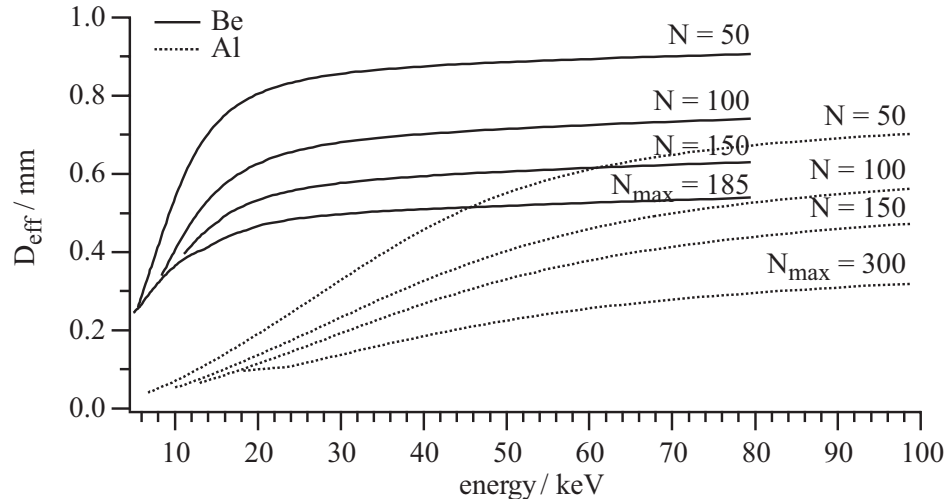


Figure 4.4: The calculated effective aperture illustrates the lower limit for the field of view. $D_{eff}$ is plotted versus the energy for the lens materials Be and Al as well as for different numbers $N$ of single refractive lenses. The parabolic radius $R = 200\,\mu$m is fixed.

Here, $D_{eff}$ is plotted versus X-ray energy for stacks of lenses with different optimal numbers of single lenses. The effective apertures strongly differ in the optimum energy range for each lens material. Whereas for Be at $20\,$keV and Al at $\sim 50\,$keV no significant change of $D_{eff}$ with

the energy can be reported.
Beryllium is always an improvement concerning the field of view compared to Al. The comparison between the field of view and the resolution is dictated by the experimental requirements.
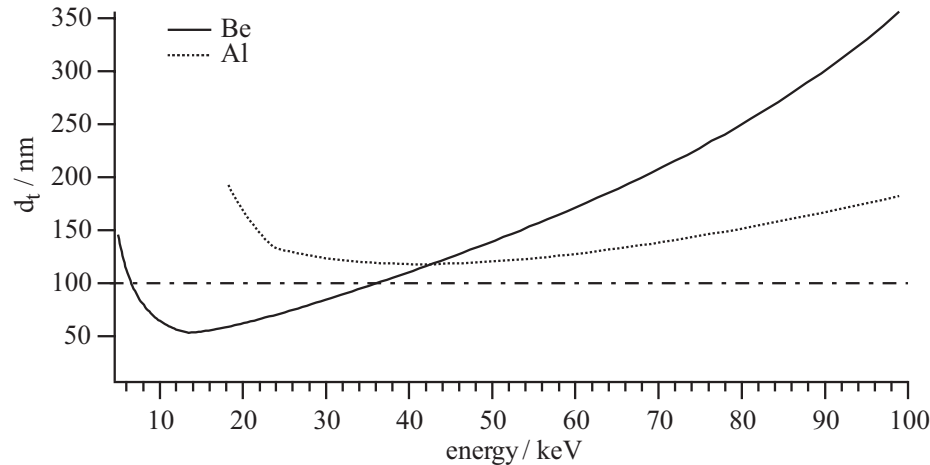


Figure 4.5: Calculated lateral resolution of rotational parabolic refractive lenses versus energy. Be lenses can achieve values below 100 nm (dot-dash line).

**Lateral resolution**

In figure 4.2, the resolution was already presented. Figure 4.5 gives a plot of the lateral resolution $d_t$ versus the photon energy $E$. In the optimization process both the parabolic radius $R$ and the number of lenses were varied. The curve for Be is decreasing to its minimum at 13.5 keV with a feasible resolution of $d_t = 54$ nm at a focal distance of $f = 0.312$ m. Between 8 keV and 36 keV a resolution below 100 nm can be achieved. This is not possible at all for Al lenses. Here, the best resolution of 115 nm occurs at 41 keV. However, above 41 keV Al lenses have a better resolution than Be lenses.

In summary, beryllium parabolic refractive lenses substantially improve the resolution in hard X-ray microscopy below 40 keV. Achieved resolutions with Be lenses are presented in the sections 5.1 and 5.2. The best results for Al lenses are discussed in [30, 31].

**Depth of field $d_l$ and depth of focus $DoF$**

The depth of field $d_l$ is a non critical parameter for applications of refractive lenses. It is only important for the size of samples in tomography experiments where the field of view is the first limiting factor. The interesting value for microprobing experiments is the depth of focus which for Al objectives was always sufficient. Otherwise the use of Be lenses constrict the $DoF$, as figure 4.6 illustrates. Considering the minimum with $DoF = 0.7$ mm for Be, these values match the usual sample size for microprobing experiments of 1 mm and below.

**Gain**

To increase the gain in an experiment using refractive lenses their transmission $T$ has to be improved and the focal spot size has to be reduced. The possible spot size is limited by the resolution. $T$ and $d_t$ benefit most from the low absorption in beryllium lenses. Indeed,
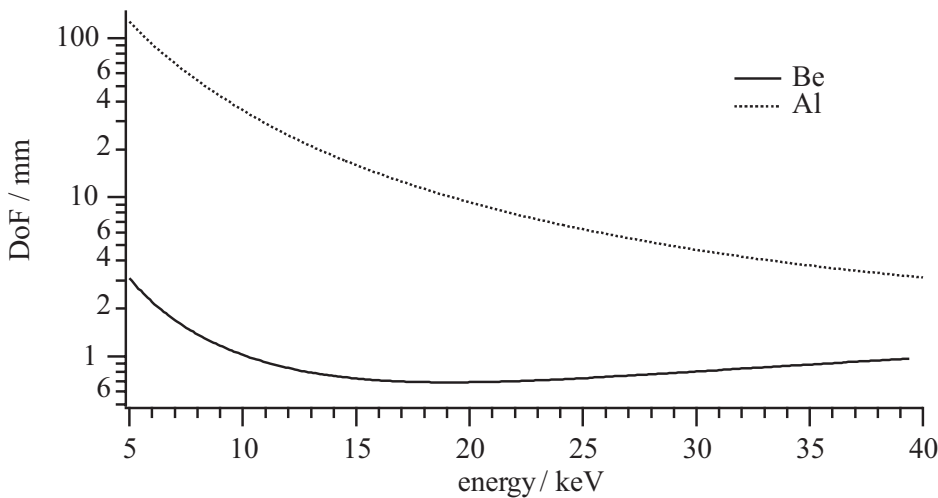
Figure 4.6: Calculated influence of the use of Be and Al for refractive lenses considering the depth of focus.

gain factors higher than $10\,000$ can be reached. The gain is influenced by many experimental parameters. To compare Al and Be lenses a source size of $0.7\,\mathrm{mm} \times 0.06\,\mathrm{mm}$ and a source-lens distance $L_1$ of $38\,\mathrm{m}$ were assumed. Likewise, for the energies $5\,\mathrm{keV}$, $12\,\mathrm{keV}$, $20\,\mathrm{keV}$, and $40\,\mathrm{keV}$ the number of lenses $N$ was optimized.

Table 4.2: The gain of optimized Al and Be objectives for different energies.

| gain | Al | Be |
|---|---|---|
| $E = 5\,\mathrm{keV}$ | | $N = 40$ |
| | | **$10\,445$** |
| $12\,\mathrm{keV}$ | $N = 24$ | $N = 154$ |
| | **$73$** | **$15\,489$** |
| $20\,\mathrm{keV}$ | $N = 95$ | $N_{max} = 185$ |
| | **$188$** | **$6\,087$** |
| $40\,\mathrm{keV}$ | $N_{max} = 300$ | |
| | **$305$** | |

The values of the gain for Be lenses are, at least, one order of magnitude higher than those for Al lenses. Even an increase of two orders of magnitude can be arranged by tuning the energy.

## 4.2   Material Quality and Shape Control

Beryllium raw material for lens production is manufactured by powder metallurgy and there-fore, it contains voids. Figure 4.7 shows a phase contrast tomogram of one of the first Be lenses in which the voids in the material become visible. This hard X-ray microscopy experiment

was done with Al lenses at beamline ID22/ESRF.

Small angle X-ray scattering can be used to find out if the materials contains inhomogeneities below $1\,\mu$m in size. Up to now, only two measurements were recorded for two different batches of 7 single Be lenses, each. In figure 4.8 the results are plotted as intensity versus the momentum transfer Q. The results of both measurements are very similar. The exponent in the power law behavior of I(Q) is $\sim$2.2 which is typical for a volume fractal (porous solid). Thus, the beryllium homogeneity can still be improved.



200 μm
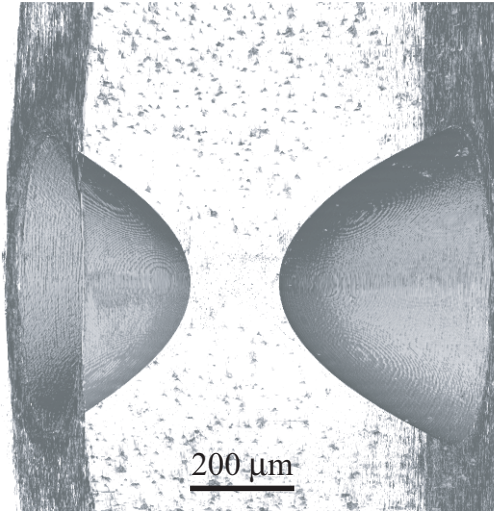
Figure 4.7: Tomogram of a single Be lens by a hard X-ray microscopy experiment. The phase contrast visualizes voids in the lens material.

As mentioned, the shape of a parabolic refractive X-ray lens is the key parameter. During the manufacturing process the shapes of the pressing tools and of the lenses themselves are tested by an optical scanning system, 'MicroProf' by *Fries Research & Technology GmbH*. An example is shown in figure 4.9(bottom). The topography of the inner lens region, $140\,\mu$m by $140\,\mu$m around its center, is displayed in a color spectrum between high (light) and low (dark) values on the z-axis. The x-points and y-points are measured in $1\,\mu$m steps, the accuracy of the z-axis is given with $100\,$nm. The horizontal line profile, through the center of the lens, is plotted in figure 4.9(top). It is fitted by a parabola of R$\,=191\,\mu$m. To illustrate the deviations, the difference between the measured data and the fit function, is plotted. The values vary by $\pm200\,$nm. Such a roughness increases a typical spot size by about $0.2\,$nm and is negligible.
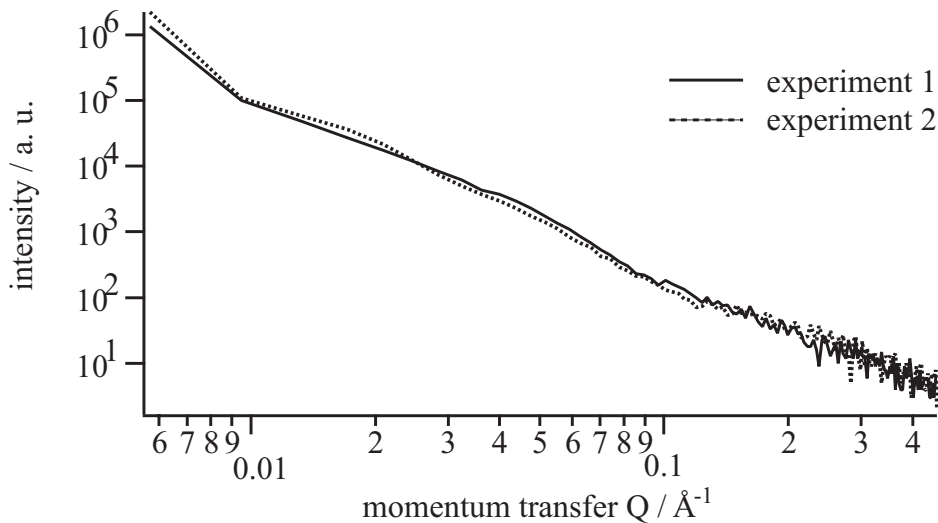
Figure 4.8: Small angle scattering of 7 beryllium lenses. Two experiments are plotted.
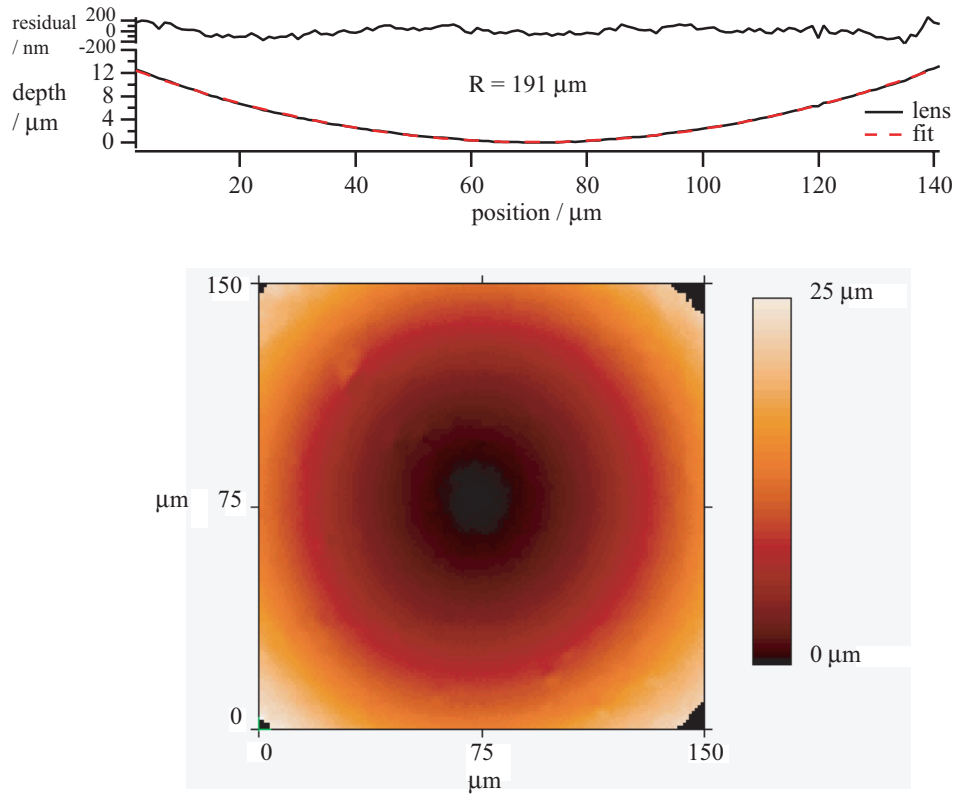


Figure 4.9: Image of the inner lens region measured by an optical scanning profile analysis. (top) Measured profile through the center of a Be lens, its parabolic fit and the differences between them.  (bottom) The completely measured inner profile in colored depth scaling presentation.

## 4.3 Comparison of Beryllium Lenses and Aluminium Lenses

To compare the lens materials beryllium and aluminium a fixed number $N = 100$ of single lenses were chosen. The design of the single lenses is the same in radius at the apex of the parabolas and geometrical aperture. For both objectives those energy regions are chosen which promise a good resolution. This is 12 keV for the Be parabolic refractive lenses and 40 keV in case of Al. Therefore, the values for $\delta/\varrho$, $\mu/\varrho$ and the transmission are similar. The effective aperture is slightly larger for Be. The resolution is about one order better for the Be lenses. Only the depth of field and depth of focus are much better for Al lenses: millimeters for Be and tens of centimeters for Al. Due to the shorter focal length of the Be objective the synchrotron radiation source is more strongly demagnified as for Al lenses. This is the reason for the enormous difference in the gain of the two experiments. The performance of refractive lenses is often questioned considering their low transmission of a few percent. But the high gain in a small spot makes them so valuable.

| | | | Al | Be |
|---|---|---|---|---|
| material: | atomic number | $Z =$ | 13 | 4 |
| | density | $\varrho =$ | $2.7\,\mathrm{g/cm^3}$ | $1.84\,\mathrm{g/cm^3}$ |
| | atomic mass | $A =$ | $26.98\,\mathrm{g/mol}$ | $9.012\,\mathrm{g/mol}$ |
| experiment: | energy | $E =$ | $40\,\mathrm{keV}$ | $12\,\mathrm{keV}$ |
| | mass index of refraction decrement | $\delta/\varrho =$ | $1.25{\cdot}10^{-7}\,\mathrm{m^3/kg}$ | $1.28{\cdot}10^{-7}\,\mathrm{m^3/kg}$ |
| | mass absorption coefficient | $\mu/\varrho =$ | $0.567\,\mathrm{m^2/kg}$ | $0.443\,\mathrm{m^2/kg}$ |
| | source horizontal | $S_h =$ | $700\,\mu\mathrm{m}$ | $700\,\mu\mathrm{m}$ |
| | source vertical | $S_v =$ | $60\,\mu\mathrm{m}$ | $60\,\mu\mathrm{m}$ |
| lenses: | number of lenses | $N =$ | **100** | **100** |
| | apex radius | $R =$ | $200\,\mu\mathrm{m}$ | $200\,\mu\mathrm{m}$ |
| | thickness | $d =$ | $0.01\,\mathrm{mm}$ | $0.02\,\mathrm{mm}$ |
| | geometrical aperture | $2R_0 =$ | $850\,\mu\mathrm{m}$ | $850\,\mu\mathrm{m}$ |
| geometry: | distance from source | $L_1 =$ | $40\,\mathrm{m}$ | $40\,\mathrm{m}$ |
| | focal length | $f =$ | $2.981\,\mathrm{m}$ | $0.452\,\mathrm{m}$ |
| | distance to image | $L_2 =$ | $3.221\,\mathrm{m}$ | $0.457\,\mathrm{m}$ |
| | effective aperture | $D_{\mathrm{eff}} =$ | $323\,\mu\mathrm{m}$ | $437\,\mu\mathrm{m}$ |
| | numerical aperture | $N.A. =$ | $5{\cdot}10^{-5}$ | $4.7{\cdot}10^{-5}$ |
| | resolution | $d_t =$ | $234\,\mathrm{nm}$ | $81\,\mathrm{nm}$ |
| | depth of focus | $DoF =$ | $81.93\,\mathrm{mm}$ | $1.227\,\mathrm{mm}$ |
| | depth of field | $d_l =$ | $3.92\,\mathrm{mm}$ | $0.144\,\mathrm{mm}$ |
| performance: | transmission | $T =$ | $5.68\,\%$ | $6.47\,\%$ |
| | spot size horizontal | $B_h =$ | $56.37\,\mu\mathrm{m}$ | $8\,\mu\mathrm{m}$ |
| | spot size vertical | $B_v =$ | $4.84\,\mu\mathrm{m}$ | $0.69\,\mu\mathrm{m}$ |
| | gain | $g =$ | 164 | 14 811 |

# Chapter 5

# Beryllium Parabolic X-Ray Lenses: Methods and Applications

Parabolic refractive lenses for hard X-rays can be used in different optical geometries. Imaging setups, which magnify or demagnify an object, taking advantage of the true imaging quality of rotational parabolic refractive lenses, comparable to glass lenses of visible light. If the source is imaged on a sample a probing microbeam is generated which is useful for analytical applications. In a scanning mode, the spatial resolution is improved due to a small focal spot, useful for example, in fluorescence and absorption spectroscopy, in diffraction experiments or in small angle scattering setups.

This chapter presents these principal applications while the improvements due to beryllium lenses are discussed. Some typical results are reported. XANES microtomography and the special demands on parabolic refractive lenses for extreme nano focusing are the topics of later chapters. First, the use of the lenses in microscopy and micro probing experiments are discussed, and the benefits for applications like tomography, lithography, micro diffraction and small angle scattering will be demonstrated. Rotational parabolic refractive beryllium lenses as an optical element for a X-ray free electron laser will be discussed as an interesting opportunity for the future.

## 5.1   Imaging and Microscopy

A typical setup for an X-ray microscope is sketched in figure 5.1. A synchrotron radiation source with a gaussian intensity distribution and an elliptic electron beam cross section is shown on the left. An object, here a mesh, is illuminated by synchrotron radiation. A rotating diffuser ($B_4C$ powder of $0.5\,mm$ to $2.5\,mm$ thickness) ensures an incoherent illumination of the object. The position of the stacked lenses and their number determine the magnification $m$ of the image. Comparable to common optics the magnification is the ratio of the image distance $L_2$ to the object distance $L_1$.

$$m = \frac{L_2}{L_1} = \frac{L_1 - f}{f}. \tag{5.1}$$

$L_2$ and hence $m$ depend only on $L_1$ and on the focal length $f$. A large magnification is achieved if the location of the sample $L_1$ is only slightly larger than the focal length.
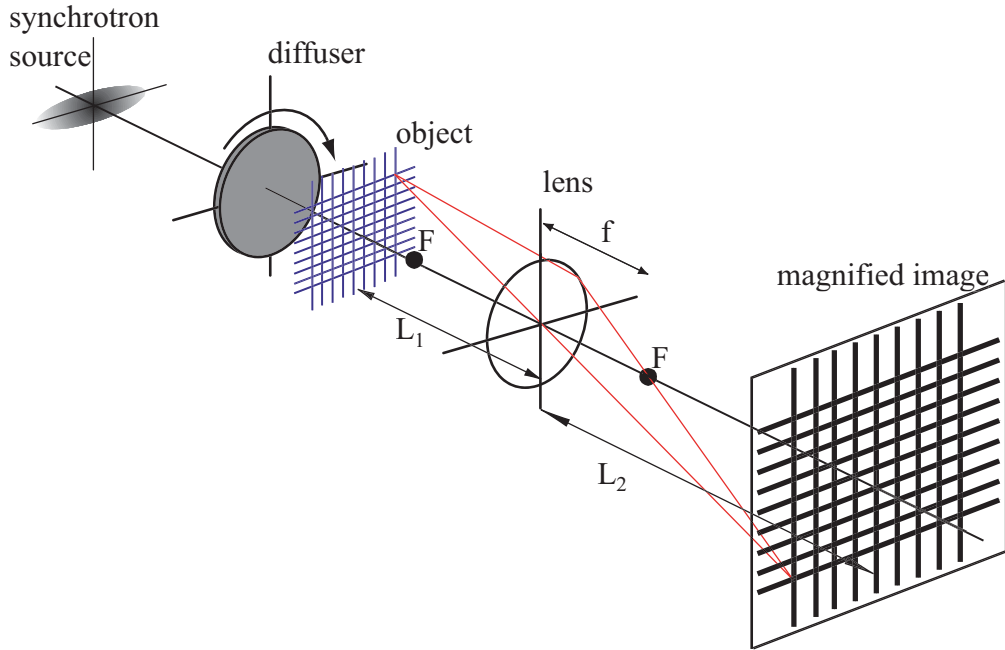
Figure 5.1: Setup for a full field X-ray microscope.
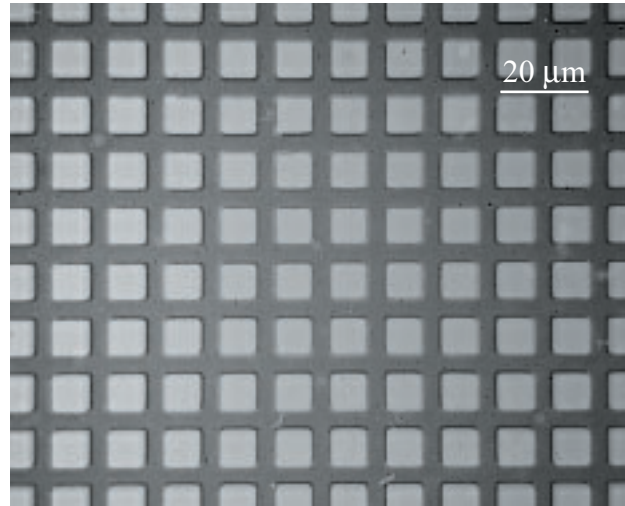


Figure 5.2: Image of an Ni 2000mesh ten times magnified on an high resolution X-ray film (inverted contrast). The absence of spherical aberration demonstrates the parabolic shape of the Be lenses, [Parameters: energy $= 12\,\mathrm{keV}$, 91 Be lenses, $\mathsf{L_1} = 41\,\mathrm{m}$, $\mathsf{f} = 495\,\mathrm{mm}$, $\mathsf{m} = 10$].

Hard X-ray microscopy is comparable to microscopy with visible light. However, the large penetration depth of hard X-rays in matter allows to investigate opaque samples. This was demonstrated with parabolic refractive lenses of aluminium on a double gold mesh with different periods [21]. Due to their high absorption Al lenses reach only moderate resolution. On the other hand, the minimal resolution for Al lenses of 180 nm is improved to an expected resolution for Be lenses of 50 nm. The values based upon the current design of the rotational parabolic refractive lenses are shown in figure 4.5. The better field of view, stronger transmission, and the use of different wavelength are additional arguments to build an X-ray microscope with beryllium parabolic refractive lenses.

An image generated by a hard X-ray microscope with an objective composed of beryllium lenses is shown in figure 5.2. The sample is a nickel mesh designed for transmission electron microscopy. Its pitch is $12.7 \, \mu m$ ($\equiv 1/2000$ inch) and its regular structure can easily reveal distortions generated by the imaging. Here, the image does not show spherical aberration and therefore, it proves the correct parabolic shape of the lenses. Flaws in the mesh are imaged, demonstrating the high quality of the lenses.

The diffuser in front of the sample ensures an incoherent illumination of the object. Otherwise some fringes caused by the sharp edges of the mesh would show up. To visualize the difference, figure 5.3(left) is a part of the Ni-mesh without the diffuser. To allow a direct comparison a part of the image in figure 5.2, which was generated with the use of a diffuser, is shown again in figure 5.3(right).
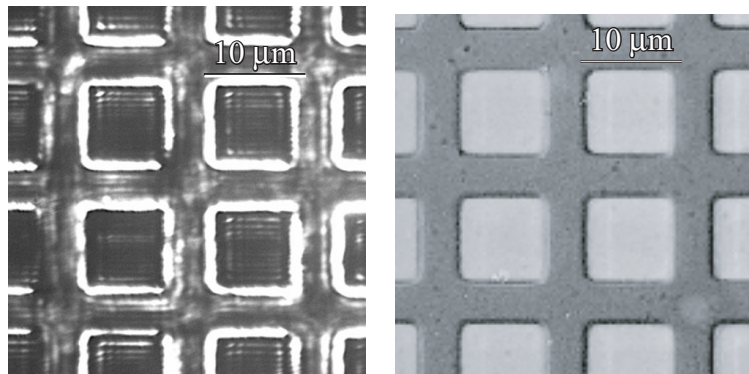


Figure 5.3: Images of the Ni mesh with partial coherent (left) and with incoherent (right) illumination of the object. A rotating $B_4C$ diffuser was used, all other experimental parameters are the same.

The vertical coherence length of the beam was changed by the diffuser from about $70 \, \mu m$ to $0.5 \, \mu m$. A more detailed consideration of the effect of the diffuser will be given in [30].

The main parameter for the quality of an image is its resolution. The improvement achieved is demonstrated next. Figure 5.4 compares the images of a grid of gold lines ($2 \, \mu m$ thick, $\sim 1 \, \mu m$ width, and with a $2 \, \mu m$ pitch) deposited electrolytically on an Si wafer, which is transparent for hard X-rays. On purpose, an area of the Au grid with many flaws was chosen, in order to visualize fine details. Figure 5.4(a) is a projection image, without lens, detected with the high resolution detector FReLon2000 [32] from 2 mm distance. Its pixel size of 680 nm is not sufficiently small to directly image the structure in all its details. The object has to be magnified to achieve a better resolution with this detector.
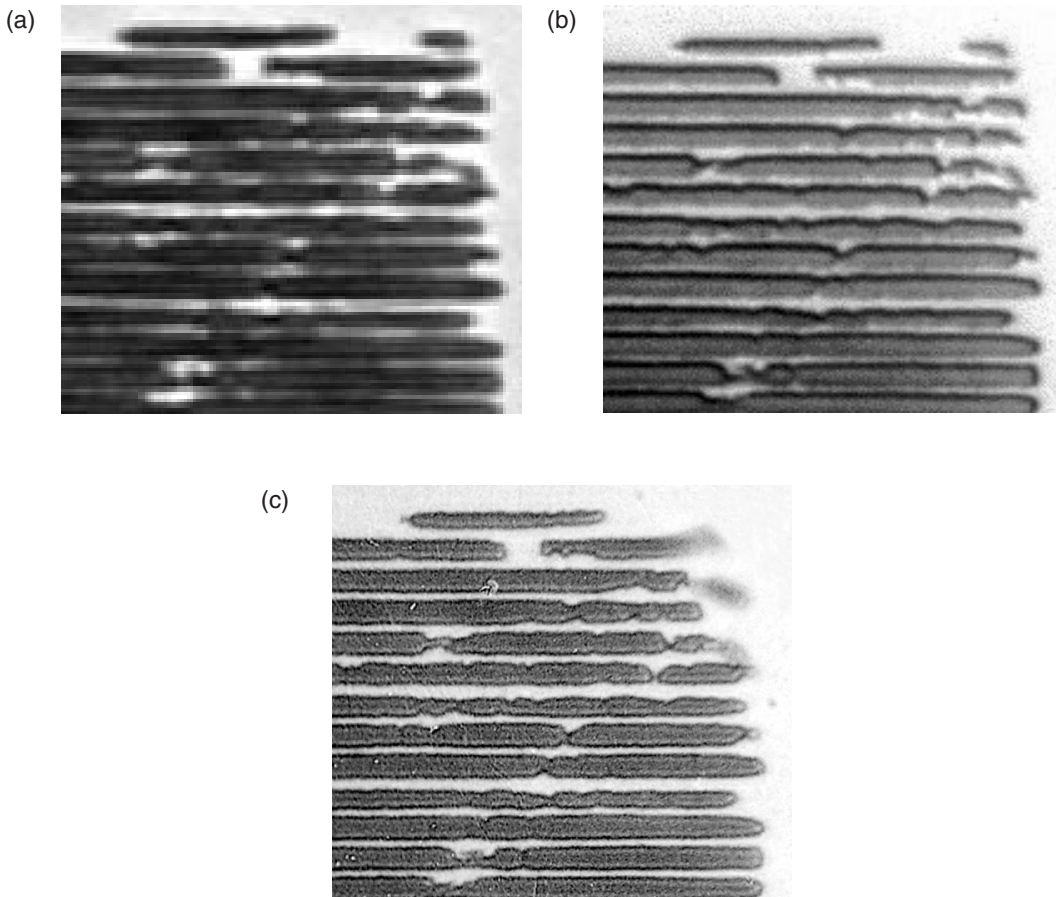
Figure 5.4: Hard X-ray microscope images of the same Au test structure [24]:
(a) Projection image on a FReLoN2000 camera without lens.
(b) 120 Al lenses magnified the image 21 times on the same camera.
(c) A Be objective improves the resolution with a magnification of $m = 10$ on a high resolution X-ray film.

A full field microscope setup was build to magnify the sample 21 times. The objective of the microscope was realized with $N = 120$ Al lenses with a focal length of $f = 1.098$ m at an energy of 24.9 keV. It should be noted that image (b) was taken with the same camera as image (a). Further improvement in resolution is achieved by a change to beryllium as lens material. At the optimal energy for Be, 12 keV, a magnification of $m = 10$ was achieved (image c). The focal length for 91 Be lenses was $f = 0.493$ m. The image was taken on an high resolution film. In order to quantity the visible improvement in resolution a line profile was taken in a region with strong contrast. Figure 5.5 depicts such a line profile. The intensity values fit an error function, with a width of 138 nm. More than 1000 line profile were analyzed. The histogram of the resolving FWHMs shows a gaussian distribution, illustrated in figure 5.5. Its maximum at FWHM $= 142$ nm $\pm 1.7$ nm corresponds to the spatial resolution of the image. Its r.m.s width of 46.15 nm, which is equivalent to a FWHM of 109 nm $\pm 2.5$ nm, is generated by the grain size of the high resolution film. Considering the magnification by a factor of 10, the grain size of the film is $1.1\,\mu$m. The ideal resolution would have been 84 nm for the given geometry.
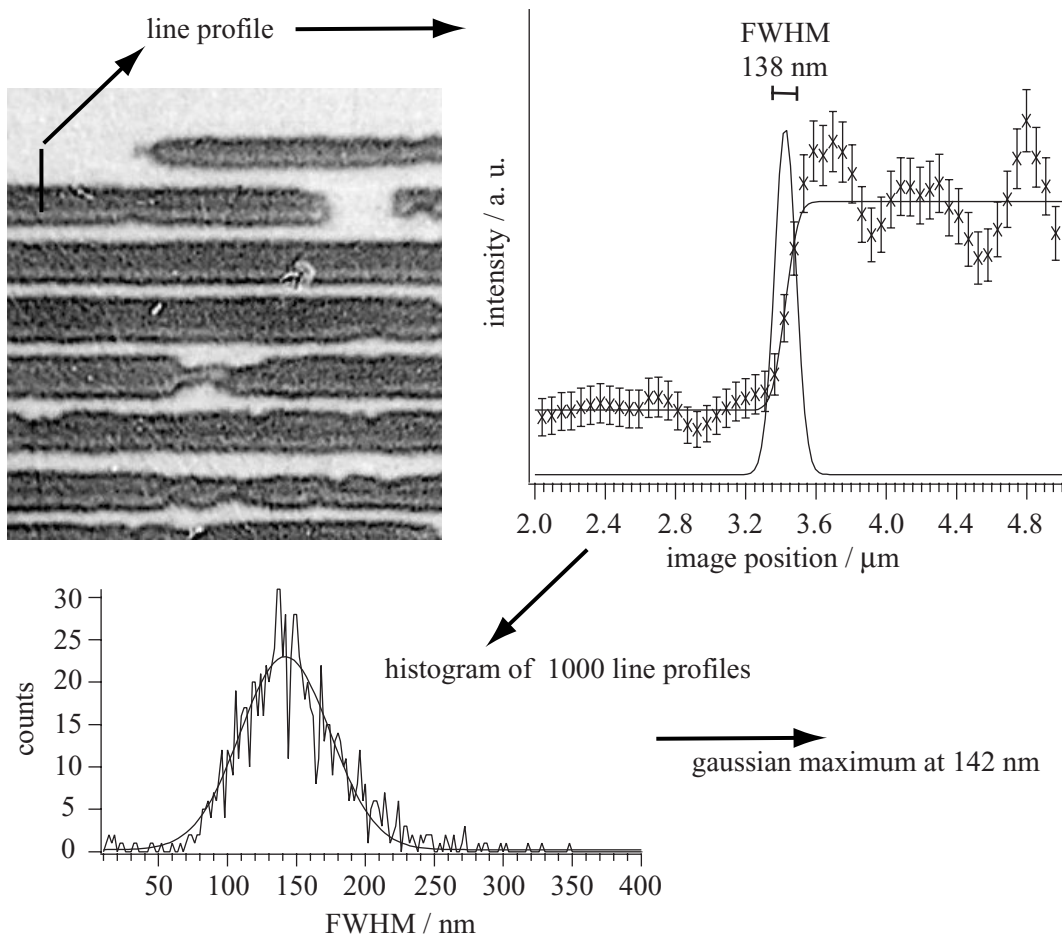
Figure 5.5: Magnified part of the Au test structure with a line profile and a histogram of many line profiles, resulting in a spatial resolution of 142 nm.

A compact microscope was set up with rotationally parabolic refractive beryllium lenses. Distortion free images were reported. Under the given experimental circumstances the objective reproduces the desired magnification of 10 times with an overall resolution of less than 200 nm over a field of view of at least 450 $\mu$m.

## 5.2    Focusing and Microprobing

Many analytical techniques need a high spatial resolution. This requires a microbeam in the $\mu$m range and below. The simplest solution would be a pinhole with the desired size, but this suffers from high intensity loss. A much better solution is an optic which images the source on the sample in a strongly demagnifying mode. So, the incident intensity is focused rather than thrown away. The quality of such an optic is characterized by its spot size and by the gain.
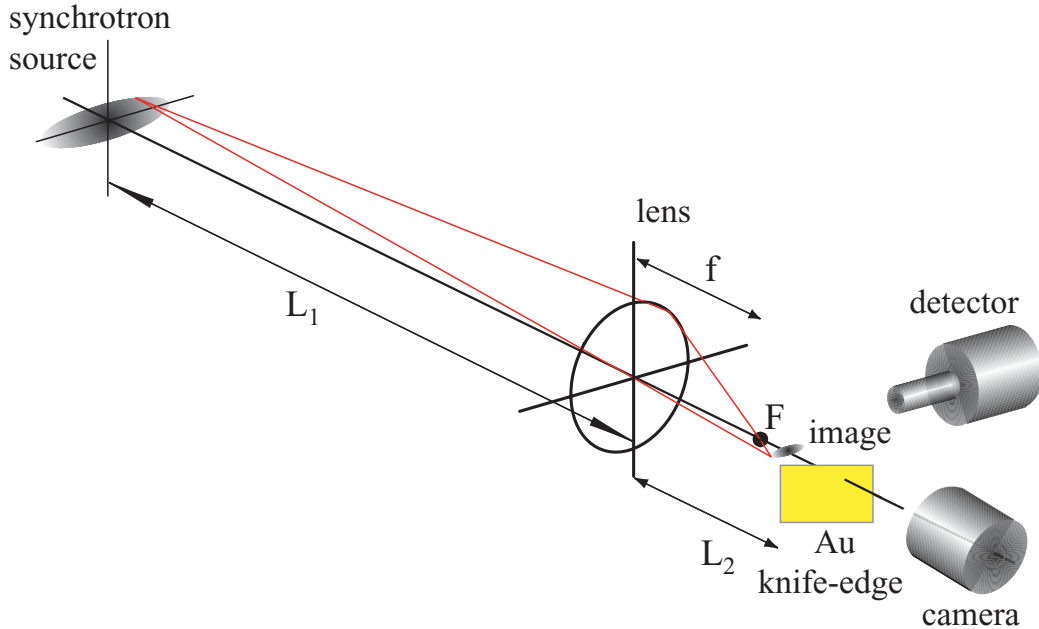


Figure 5.6: Microprobing setup with fluorescence detection.

In figure 5.6 is sketched a microprobing setup. The source size and the beam divergence differ for each synchrotron radiation beamline. For best resolution the image of the source has to be demagnified as much as possible. This needs a large value for $L_1$ (typically 30 m to 75 m) and a small value of $L_2$ (dictated by the focal length of the lens).

Here, the microbeam is characterized by knife-edge scans. A sharp edge was moved through the beam and the transmission or, as in our case, the fluorescence is recorded. The examples in figure 5.7 were measured at beamline ID22 / ESRF. The source size was 0.06 mm in the vertical and 0.7 mm in horizontal direction. For a demagnification $N = 91$ Be lenses were used at $E = 12$ keV. The intensities were measured with a PIN diode.

The flux recorded were:

$$\begin{array}{rll}
I_0 = & 3.05 \cdot 10^{12} & \text{ph/(s\,mm}^2) \quad \text{[incident radiation]} \\
F_L = & 1.05 \cdot 10^{11} & \text{ph/s} \qquad\qquad \text{[through the lenses]} \\
F_f = & 7.98 \cdot 10^{10} & \text{ph/s} \qquad\qquad\quad \text{[in the spot]} \\
\equiv & 4.35 \cdot 10^{15} & \text{ph/(s\,mm}^2)
\end{array}$$

The scans of figure 5.7 can be fitted as error-function. It appears that the measured data are fitted best by the sum of two error functions. The broad one describes a background.
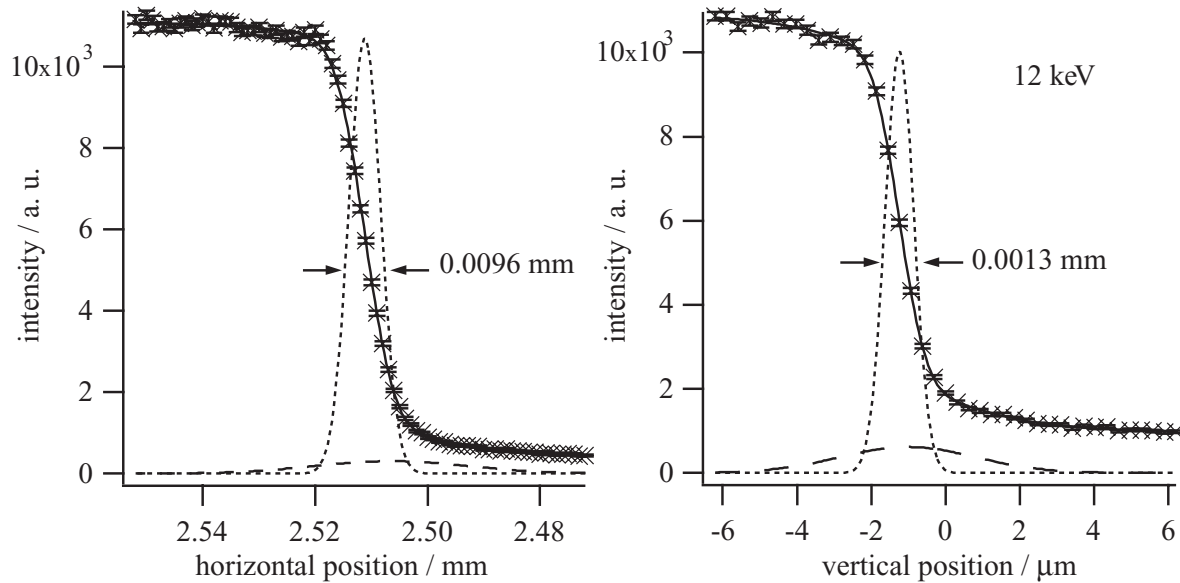
Figure 5.7: Au L$\alpha$ fluorescence knife-edge scans with a Be lens objective. The sharp edge of the knife was moved in horizontal and vertical direction through the synchrotron radiation beam.

Partly, it is formed by an image of a virtual source caused by other beamline optics (e. g. the monochromator or mirrors) and/or beam instabilities. Furthermore, small angle scattering in the lens material can increase the background. The scans of figure 5.7 show a background of 28.7% vertical and 13.7% for the horizontal knife edge scan. Adding the squared Gaussian widths results in a spot size of $1.7\,\mu m \times 10.9\,\mu m$. The flux measurement gives $7.98 \cdot 10^{10}$ photons per second in the focal spot ($\mathsf{F}_f \simeq 76\% \,\mathsf{F}_L$), which corresponds to a gain of $\mathsf{g} = 1425$, in comparison to a hypothetical pinhole in the size of the spot.

Even the optimal resolution and the ideal gain were not yet reached, the improvements due to the use of Be lenses for analytical applications are already now outstanding.

Microscopy and microprobing are the most important fields of application of the parabolic refractive lenses. The following sections describe applications relaying on this two techniques.

## 5.3   Tomography

Tomography is a 3-dimensional imaging of opaque media without the need for cutting the object. For that purpose, projection images at different sample orientations are recorded. Different analytic techniques can be used to generate these projection images. Invented for medical X-ray analysis, the method has developed beyond that. Magnetic resonance, ultrasound or radioisotopes produce common tomographic images.

Both lens geometries, focusing and imaging, can be used in a tomographic setup. A magnifying setup results in increased resolution. In a scanning approach, the microbeam setup improves the spatial resolution of analytical tomographic applications.

### 5.3.1   Scanning Tomography

As outlined in figure 5.8(a), an opaque sample is scanned step by step with the focused beam
at equidistant positions (dashed lines). After such a translational scan, the sample is rotated
by an fraction of the full rotation and the translation scan is repeated. When the sample
has completed a full rotation all points of the scans lie on a virtual slice through the sample,
figure 5.8(b). The probe, in our case the X-ray microbeam, samples in each beam position
an integral of the real or of the imaginary part of the index of refraction in the plane (x,y).
We call $\mu$(x,y) or $\delta$(x,y) by f(x,y). Let us first consider tomography in absorption contrast:
f(x,y) $= \mu$(x,y).
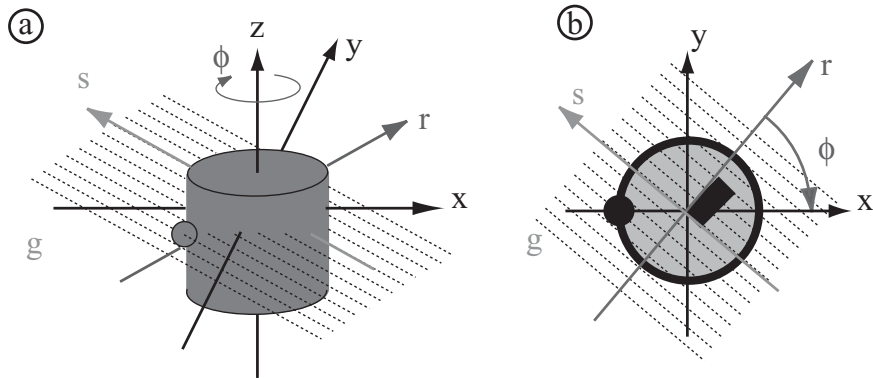


Figure 5.8: The space coordinates of a virtual slice through a symbolic sample in scanning
tomography.

In figure 5.9(a) the absorption coefficient $\mu$ is displayed for a single translation scan. The
values are calculated from the measured intensity by correcting for dark current and by
dividing the incident intensity. The results are presented in two different ways, as the standard
graph of $\mu$ versus the scanning position $r$ or as $\mu$ being color scaled as a function of r. This
parallel projection of $f(x, y)$ is the Radon transform $p_\phi(r) = \int_g f(x, y)ds$. It is the integration
over each scanned paths g at position r and at angle $\phi$ [33]. In figure 5.9(a) the result of the
first scanning at the angle $\phi = 0°$ is shown. Figure 5.9(b) illustrates the situation after 10 steps
of rotation, when the sample was rotated to 116°. The results for $\mu$ at each scanning position
build up a sinogram. The inverse radon transform reconstructs the desired information from
such a sinogram. It can be implemented as the filtered back projection algorithm [34]. This
is based on the Fourier slice theorem that links the Fourier transform $\tilde{p}_\phi$(r) of a projection
$p_\phi$(r) to the two-dimensional Fourier transform $\tilde{f}(k_r \cdot \cos\phi, k_r \cdot sin\phi)$ of the object on the
virtual slice:

$$\int p_\phi\left(r\right)e^{irk_r}dr \quad = \quad \int f\left(x, y\right)e^{i(xk_r cos\phi + yk_r sin\phi)}dxdy \tag{5.2}$$

$$\tilde{p}_\phi(k_r) \quad = \quad \tilde{f}(k_r \cdot \cos\phi, k_r \cdot sin\phi) \tag{5.3}$$

The Fourier transformation of the object function is given in polar coordinates ($k_r, \phi$)). To
avoid difficulties with resampling the Fourier components onto a regular lattice, the Fourier
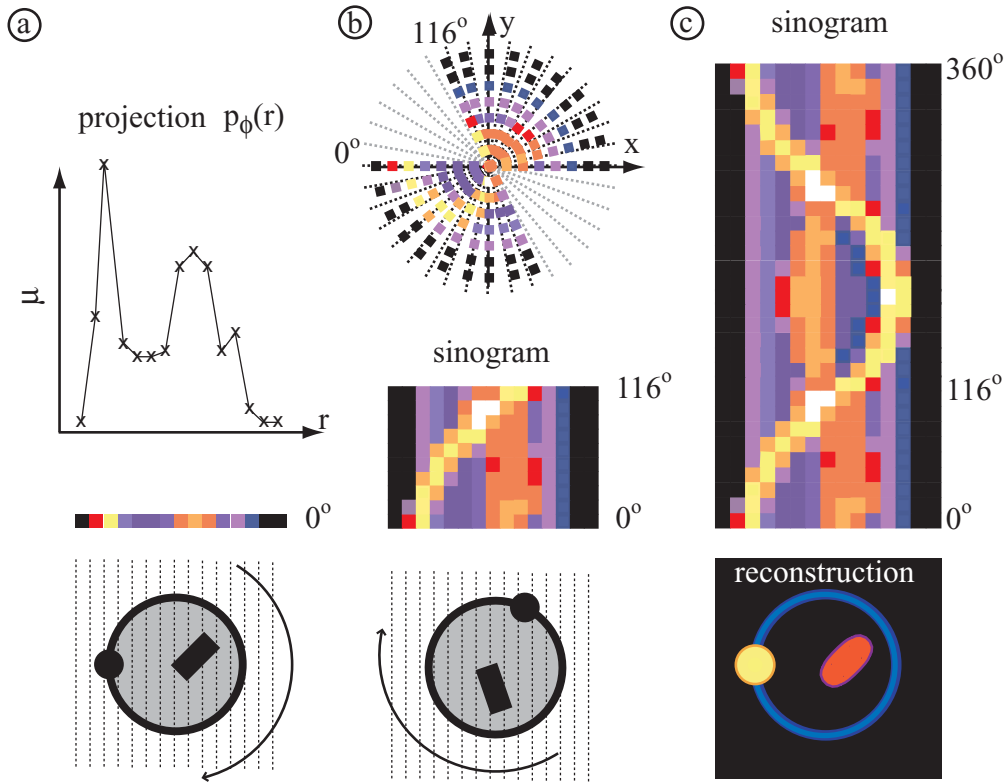
Figure 5.9: Information processing in scanning absorption tomography.
(a)Measurement of the first projection at angle 0°.
(b)The sinogram and its representation as Fourier transformation.
(c)The complete sinogram and its reconstruction.

backtransformation is usually done in polar coordinates. This backtransformation is part of the 'filtered backprojection algorithm':

$$
\begin{aligned}
f(x,y) &= \frac{1}{(2\pi)^2} \int_0^\pi \int_{-\infty}^\infty \tilde{f}\left(k_r\cos(\phi), k_r\sin(\phi)\right) \cdot e^{ik_r(x\cos(\phi)+y\sin(\phi))}|k_r|dk_r d\phi \\
&= \frac{1}{(2\pi)^2} \int_0^\pi \int_{-\infty}^\infty \tilde{p}_\phi(k_r)e^{ik_r r}|k_r|dk_r d\phi
\end{aligned}
\tag{5.4}
$$

$|k_r|$ is called the filter in Fourier space.

The projections build up a sinogram as illustrated in figure 5.9(c). Each single part of the object follows a sinusoidal path during a full sample rotation. This rotation of 360° is not necessary for a measurement in a transmission mode because all necessary information is recorded within 180°.

According to the sampling theorem (Nyquist theorem) the optimal step size is half the spot size of the microprobe, $n_t$ translation steps, and in addition the sample has to be rotated $(\pi/2 \cdot n_t)$ fractions of the full rotation [34]. These considerations are contradicting requirements for a short acquisition time. In figure 5.9 the sampling is too coarse. Therefore, all structures
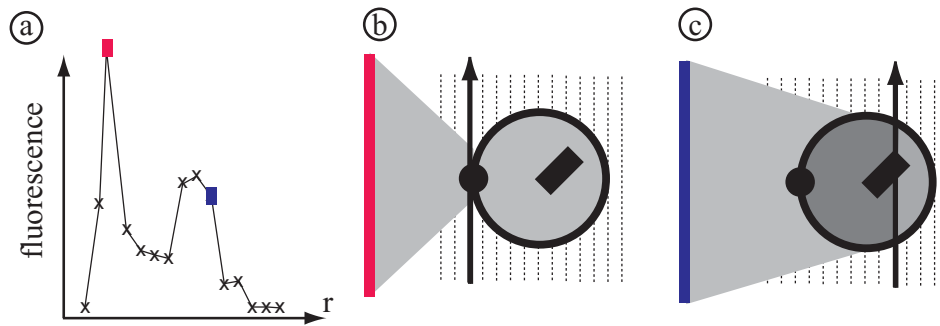
Figure 5.10: Illustration of the selfabsorption effect in fluorescence microtomography.

appear bigger than they are and they are washed out. The sharp edges of the quadrangle are not resolved. All these aspects have to be considered in the planing of an experiment and in the interpretation of the reconstructed tomograms.

Tomography can also be done in a fluorescence mode. For that purpose, the fluorescence radiation emitted by the sample is detected by means of an energy dispersive detector. The detector is located, in general, perpendicular to the X-ray beam, in order to minimize the elastic X-ray scattering. Fluorescence tomography is important for the localization of trace elements and for element distribution. The energy of the fluorescence radiation is lower than the exciting energy. Also the absorption inside a sample must be taken into count. Figure 5.10 illustrates this selfabsorption. When the beam hits the sample on the detector side the fluorescence radiation is barely reduced in intensity by absorption in the sample (b). Unfortunately, if the beam hits the sample on the far side from the detector, strong absorption may occur (c). A correction algorithm for self-absorption was developed [35]. However, a full rotation of the sample in unpair equidistant steps is required.

A microbeam generated by a beryllium refractive lens has more intensity than that by an aluminium lens. As a consequence, the long data acquisition times in tomography can be reduced and/or the density of the sampling points can be increased in order to optimize the resolution. Examples of XANES microtomography and high resolution fluorescence tomography are given in the chapters 5 and 6.

### 5.3.2   Magnifying Tomography

Magnifying tomography requires the same experimental setup as the microscopy setup shown in figure 5.1. The principal differences in figure 5.11 are a fully rotatable sample and a computerized reconstruction algorithms of the measured data.

For each equidistant angle position of the sample one X-ray micrograph is recorded. Due to the small beam divergence the micrographs can be considered as parallel projections. A sample rotation of 180° provides complete information, which will be reduced by insufficient sampling, mechanical instabilities and lens aberrations. The sampling requirements defined by the Fourier slice theorem are the same as for scanning tomography. Also flat field and dark field corrections are required. A flat field is a micrograph without sample to document intensity variations of the incident beam. On the other hand, dark fields taken without incident radiation document the detector performance, e.g. its dark current. Due to the long

acquisition times the flat fields are recorded at regular intervals in order to correct for time dependent beam stabilities.
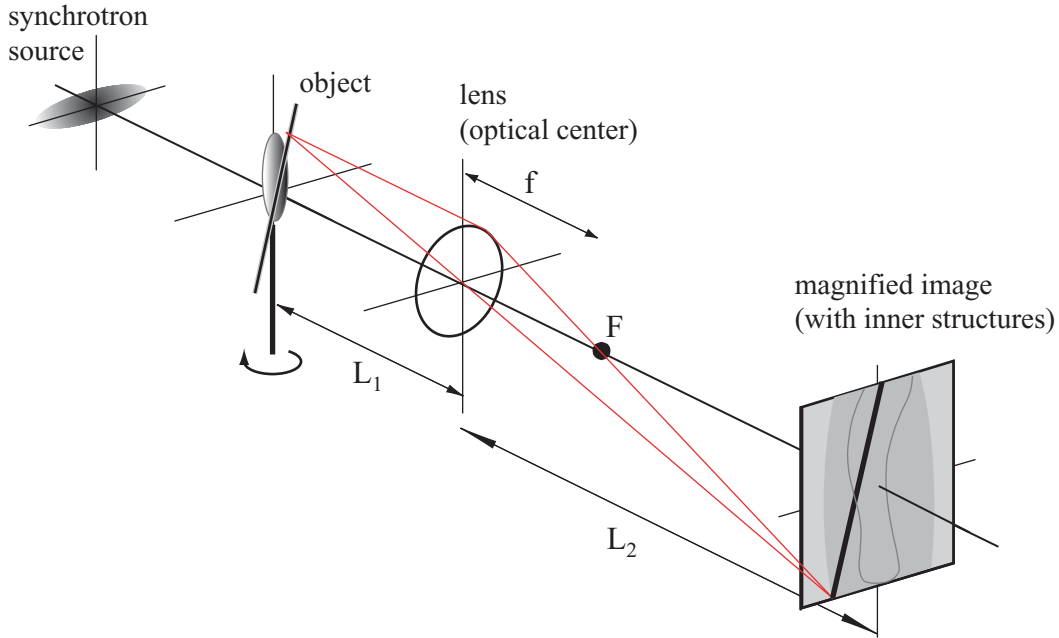


Figure 5.11: Setup for magnifying tomography.

Some samples, especially biological ones, are not sufficiently absorbing to get a contrast based on absorption. Therefore, the highly coherent radiation from a synchrotron source provides an other possibility: tomography in phase contrast. A change of the refraction index disturbs the free propagation of the wavefront. This leads to interference fringes. For a quantitative analysis with phase contrast at least two tomograms have to be recorded, one of them in a defocused plane, in order to reconstruct the phase and the amplitude of the transmission function.

The need of many projection for the reconstruction of a tomogram leads to hours of acquisition time. In reference [31] the reconstruction is shown of a AMD K6 microprocessor. The data were taken with Al lens ($N = 120$). The resolution achieved was $420\,nm \pm 100\,nm$. Each projection was recorded in $40\,s$ and 500 projections were required. The total acquisition time was $5.5\,h$ (without motor movements and readout times!). The better transmission of a Be objective and its larger aperture improve the experimental conditions. A resolution below $100\,nm$ is expected. The larger field of view which can be achieved with Be lenses allows for larger samples to be analyzed by tomography.

In summary, parabolic refractive lenses, their flexibility and easy alignment, have made magnifying and microprobing hard X-ray tomography feasible. The use of beryllium lenses extends the accessible energy range. Their better transmission is extremely helpful in reducing the time of data acquisition. The full field microscope describe in section 5.1 reaches a resolution of at least $145\,nm$. It is planned to transfer this into tomography during a high resolution magnified tomography experiment at an undulator source.

The scanning tomography with Be lenses from chapters 5 and with Si lenses from chapter 6

illustrate the new techniques and samples which can now be analyzed. XANES microtomography can be performed with sufficient intensity. Fluorescence tomography is recorded in record resolution. In principle other analytical methods like diffraction, small angle scattering, etc. could be likewise implemented in a tomography experiment.

## 5.4  Hard X-Ray Lithography

Lithography is a method for micro structuring. A resist is partially illuminated and changes its structure at the exposed spots. Well established processes based on UV-light, soft X-rays or electron beam lithography allow the manufacturing of fine structures with a high aspect ratio. In that regard, refractive X-ray beryllium lenses find some promising applications.

- Demagnifying the image of an X-ray mask may alleviate some of the problems with the production of contact masks.

- The large penetration depth of hard X-rays into the resist allows thick layers and high aspect ratios (deep X-ray lithography) which are required, for example, for Fresnel zone plates, section 2.2.

- The higher photon energies reduces disturbing proximity effects due to scattering, photoelectrons, and fluorescence which have direct impact on the quality of the imaging.
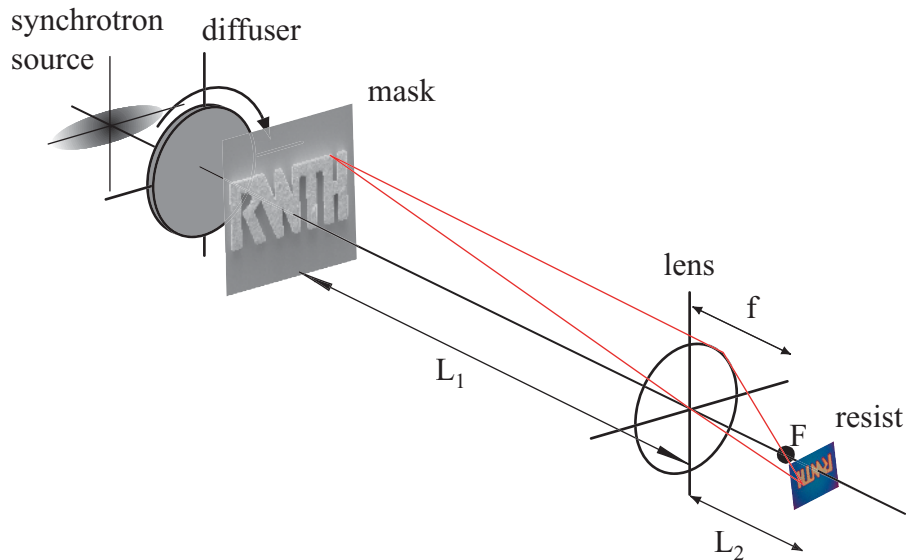


Figure 5.12: Setup of a hard X-ray lithography experiment using rotational parabolic refractive lenses.

As mentioned above, the typical experimental setup for hard X-ray lithography in figure 5.12 is comparable to the imaging method of full field microscope in figure 5.1. To get a demagnification, the image distance $L_2$ has to be smaller than the distance $L_1$ to the object.

Demagnified imaging for lithography requires high quality optical components. Be lenses for hard X-ray lithography are highly recommended because of the large aperture and high transmission which are needed to get a reasonable X-ray dose in the resist.

The first experiment with Be lenses was a feasibility test of hard X-ray lithography. The synchrotron radiation was collimated by a Be condenser lens (16 single lenses). Then the coherence of the beam was reduced by a $B_4C$-powder diffuser (1 mm thickness), to avoid interference fringes due to the sharp edges of the mask. The mask composed of $\sim 20\,\mu m$ thick gold on a transparent substrate (e.g. Si or Be). The distance $L_1 = 3.66$ m between the mask and the objective lens was chosen as large as possible within the boundaries of the experimental hutch. An undulator harmonic ('pink' beam) at 20 keV was used without loss of focusing (section 3.8). During this experiment at the ID22/ESRF an objective with $N = 108$ single Al lenses was used. A demagnification of 4 times was generated (focal length $f = 0.714$ m and $L_2 = 0.89$ m). The image projection was verified with the FReLon2000 CCD camera at the position the sample.

The first mask was a 'wagon wheel' of $22\,\mu$m thick gold on a beryllium wafer. The 'wagon wheel' consists of well defined spokes which get thinner at the center. This structure allows, even at partial illumination, to estimate the resolution and field of view. Figure 5.13 illustrates the need for all optical components. Whereas image (a) is the result with $N = 108$ Al lenses, image (b) was taken with 16 Be lenses as condenser lens in front of the mask increasing the
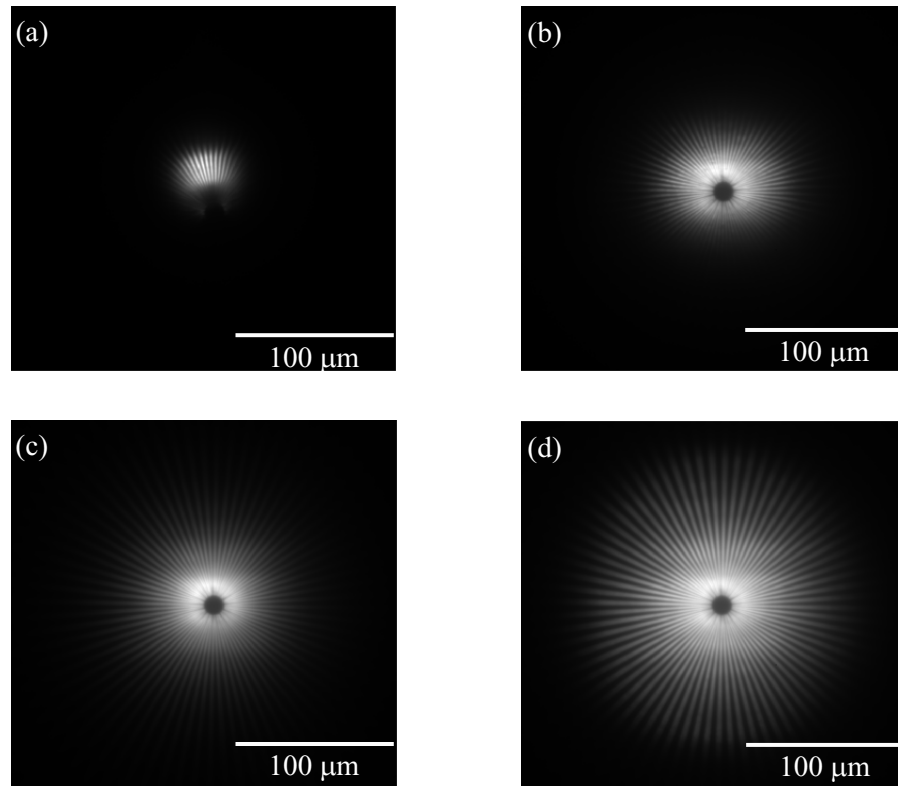


Figure 5.13: Comparison of the image size with different optical tools. A wagon wheel imaged by (a) an Al lens objective, (b) with a Be field lens, (c) with a $B_4C$ diffuser, and (d) with Be field lens and with diffuser.

size of the image from $54\,\mu$m to $128\,\mu$m. The influence of the diffuser is displayed in image (c). The best image (with $204\,\mu$m in size) is achieved when all 3 components are installed (image d).

| | |
|---|---|
| only Al lenses | $54\,\mu$m |
| Al and Be lenses | $128\,\mu$m |
| Al lenses + diffuser | $175\,\mu$m |
| Al and Be lenses + diffuser | $204\,\mu$m |

The listed values were measured on the camera with a four fold demagnification. Therefore, with the help of the diffuser and the Be field lens the Al objective generates a field of view of $616\,\mu$m.

To optimize the optic for hard X-ray lithography is the first step. To transfer the imaged structures into a resist is a second more complicated step. The resist itself, its thickness, exposure time, and the characteristics of the developer in time and concentration must be evaluated and optimized, too. 'Demagnifying X-Ray Lithography' is the theme of the PhD thesis by C. Zimprich (RWTH), which should be refered for further information [36]. Here, we confine in figure 5.14 to illustrate the transfer of a structure into the negative resist AR-N 7700 by 'Allresist'. The mask was gold with a thickness of $15\,\mu$m on a silicon wafer. The generated demagnification correspond to a 2.8x reduction [parameters: $\mathsf{E} = 25\,\mathrm{keV}$, $\mathsf{N} = 130$, $\mathsf{L}_1 = 3.62\,\mathrm{m}$, $\mathsf{L}_2 = 1.28\,\mathrm{m}$].

It is unlikely that hard X-ray lithography will replace the well established electron beam, soft X-ray, and/or UV lithography. But creating mask for these methods could be accomplished by hard X-ray lithography. Special resists, for example doted with Pd, could reduce the proximity effects which now blur the image. The possible high aspect ratios are certainly worth mentioning.

Beryllium parabolic refractive lenses made it possible to implement hard X-ray lithography. Their good transmission allows reasonable exposure times. The large field of view may be beneficial for further development in hard X-ray lithography and for other imaging applications.
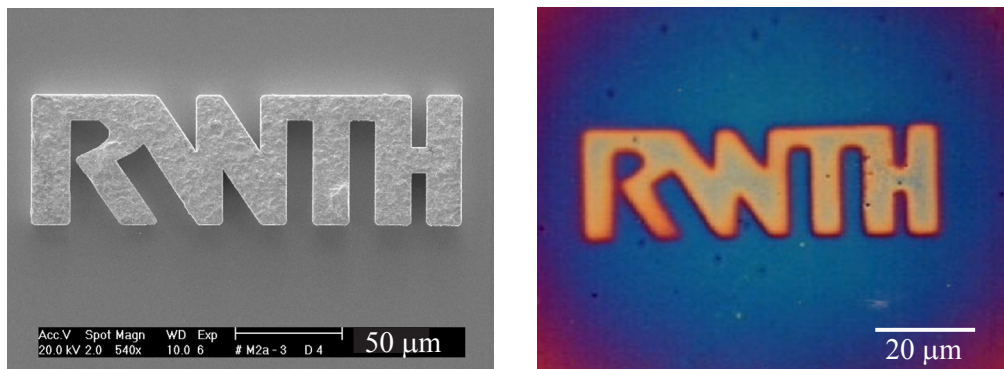


Figure 5.14: (Left) SEM image of the mask, gold deposited by electroplating on silicon. (Right) Demagnified lithography of the RWTH logo, reduction 2.8x.

## 5.5 Micro Small Angle X-Ray Scattering

The origin of the common analytical method small angle X-ray scattering (SAXS) is described in section 2.1. A microbeam allows for the combination of SAXS with a high lateral resolution. SAXS requires a small beam divergence. This can be achieved with refractive lenses when the focal length is not too small. The following test experiment was executed with 5 single parabolic refractive Be lenses. The design of the microfocusing beamline ID13 / ESRF allows a lens positioned between 34 m and 44 m distance from the low-$\beta$ undulator source, which is typical $150\,\mu m \times 50\,\mu m$ FWHM in size. At an energy of 12.7 keV and at a source-lens distance of 34 m the image is generated at 13 m behind the lens. A theoretical depth of focus of 41 cm indicates the small divergence. For the first time, the possible effective aperture in this geometry $D_{eff} = 1.05$ mm was larger than the manufactured geometrical aperture of the refractive lenses with $2R_0 = 850\,\mu m$. In the present setup, the lens performance was not fully exploited, because the focal spot was defined by the same aperture in front of the sample in both experiments. So the main improvement in using the Be lenses was an increase in flux. To demonstrate the small angle resolution of the whole setup a collagen test sample was analyzed. The central part of the small angle scattering pattern is shown in figure 5.15 (right). It is fully comparable with a former experiment, which used ellipsoidal mirrors instead of the Be lenses as focusing optic and the same aperture-collimator setup figure 5.15(left) [37]. Both
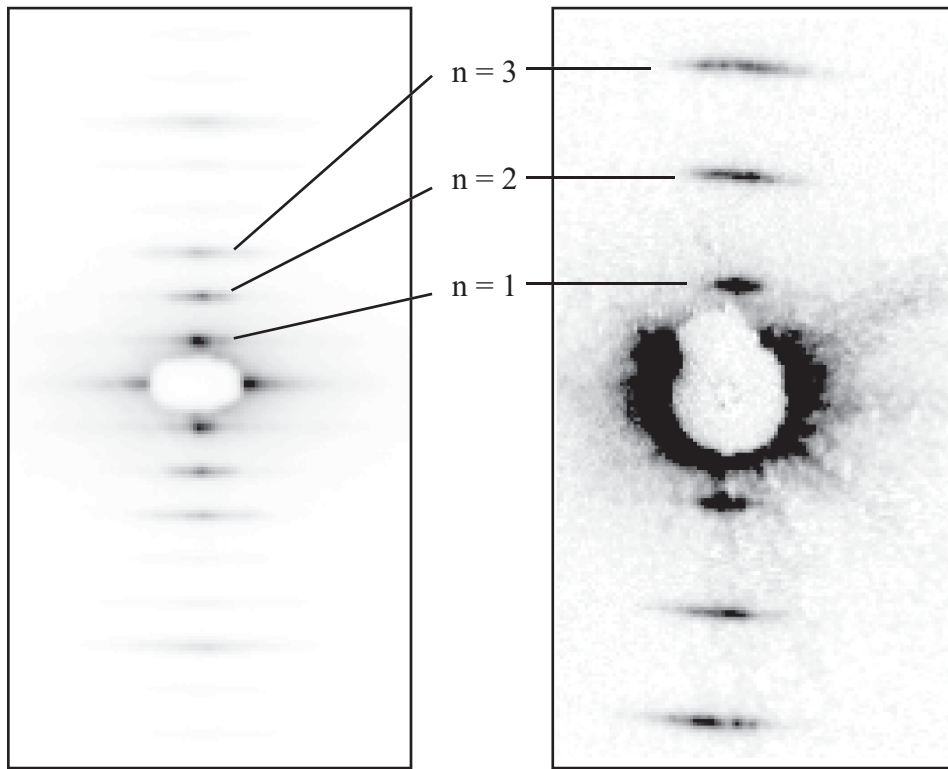


Figure 5.15: Small angle scattering of a collagen test sample from a rat tail. (Left) Experiment without refractive lenses. (Right) Using 5 parabolic refractive Be lenses in the same experimental setup. The images show the same area of the detector.

images show the same detector area. During the micro small angle scattering experiment with refractive lenses the detector and the beamstop were positioned in a larger distance from the sample. This results in the better resolution in the right image of figure 5.15. Detailed calculations during the following experiment by S. V. Roth (ESRF) were able to evaluate the changed experiment parameters. The maximal resolvable particle size increases from 110 nm to now 140 nm. As described in section 2.1, the better the resolution of the forward scattering angle is the larger the structures are which can be resolved.

Also, more flux by a factor of 1.4 was measured. However, the most important improvement is in the marginal divergence of the probing beam. Focused by ellipsoidal mirrors a divergence of 0.2 mrad was recorded. The same experimental setup with Be parabolic refractive lenses reported a divergence of 0.05 mrad.

The lenses were not optimized for the SAXS experiment, nor was the experimental setup optimized for the use of refractive lenses. Again, there is ample room for improvements in the future. Lenses with a geometrical aperture larger than 1 mm can be used to improve the flux, further. The additional aperture in front of the sample should match with the spot size produced by the refractive lens which was not realized here. The radius R of the refractive optics and of the relative positions of the final aperture and the parabolic refractive lenses should be optimized. In addition, a nanofocusing setup, as described in chapter 7, and tomographic approaches can be carried out in combination with small angle scattering. Even an additional specially designed refractive optics for parallelization of the synchrotron radiation is a possibility.

## 5.6   Beam Conditioning

Microanalysis applications with beryllium lenses were presented with best performances in resolution, magnification, or gain. But often there is no need to use extreme geometries. Slight changes in the beam path can be the key for improvement of standard experiments. One single lens in a distance from the source equal to the focal length reduces the beam divergence. Under ideal circumstances parallelism can be achieved, without reduction of the coherence of the beam. A one-to-one imaging geometry can be established at most beamlines of 3rd generation synchrotron radiation facilities due to the highly flexible concept of refractive X-ray lenses. The benefit would be an increase in intensity per area and a control element for the beam divergence, already under development at the sub-picoscecond pulse source SPPS at the Stanford Synchrotron Radiation Laboratory SSRL. Since refractive lenses keep the direction and the position of the beam their installation in a beam line has little influence on the positioning of other optical components. This clearly demonstrates the flexibility in using refractive lenses. Furthermore, the ability to reproduce the lens position with standard lateral stages is helpful. Also, the lenses can withstand the white beam of an undulator source of a third generation synchrotron radiation facility without degradation [21, 38].

## 5.7   Refractive Lenses for X-Ray Free Electron Lasers

The next generation of synchrotron radiation sources will be the X-ray free electron laser, XFEL. Linac-based XFELs use self-amplified spontaneous emission (SASE). The expected time-average brilliance will be up to 6 orders of magnitude higher than for 3rd generation synchrotron storage rings. The peak brilliance can increases even by 10 orders of magnitude.

A highly spatial and temporal coherent beam with intense and short pulses promises unique scientific opportunities. Analysis in the timescale of chemical reactions and Coulomb explosion should be realizable. Diffraction by single molecules is discussed. Plasmas can be generated in unexplored quality. The melting and crystallization processes of clusters may be observed. The parameters for the following argumentation were taken from the TESLA Design Report and supplements of it [39, 40]. The energy range available will be 0.2 keV to 12.4 keV with the possibility to reach 100 keV in the final phase of the construction. The use of Be lenses would be useful at energies above 5 keV. The typical source size at an XFEL undulator source will be 65 $\mu$m - 110 $\mu$m FWHM. The divergence of the synchrotron radiation beam will be 0.8 $\mu$rad to 27 $\mu$rad. Despite these excellent parameters the intensity and the beam size will not be good enough for certain experiments. For example, the experimental designs in plasma physics were calculated with spot sizes of 6 $\mu$m in diameter and smaller [39]. Rotational beryllium parabolic refractive lenses are introduced an optical element for microanalysis at XFELs [38, 41].

Normally, refractive lenses are installed at 40 m to 70 m from the source. The TESLA-XFEL lay-out will make it possible to put the lenses in more than 500 m distance from an undulator source, where beam size will be about 910 $\mu$m in diameter. Therefore, the current refractive lens design exactly matches the size of the X-ray beam.

The average power density of an XFEL is still moderate, $\sim 28$ W/mm$^2$, whereas the peak power is not! The expected peak power in this energy region is 24 GW. In addition, it is assumed that close to the exit of a SASE undulator all condensed matter will be destroyed when it is exposed to the radiation. At a distance of some hundred meter from the source low Z elements, like Be, may withstand the beam [42]. A Be lens in the current design absorbs 6.4 % at 12 keV. This corresponds to 4.6 W absorption in the first lens and to 72 W for an ensemble of 100 single lenses. The peak power in the whole geometric aperture of the first Be lens is still below the safe level of 0.01 eV/atom [42]. The cooling of a complete Be lens system can be accomplished. All main parts are of metal with high thermal conductivity. A slightly different design for the lens holder which includes vacuum, water cooling, and connections for thermocouples, is in fabrication. Experimental test in the white beam of a 3rd generation synchrotron radiation facility will be performed in cooperation with the ESRF at ID13.

An other key parameter of XFEL radiation is the time structure of the synchrotron beam. Light pulses of 80 fs are expected. This fantastic time resolution is important for the analysis of fast dynamics in life science or atomic processes. Furthermore, the XFEL promise to be the X-ray source with the best coherence ever achieved. New analytical experiments are thinkable. Perfect Be lenses do not deteriorate the time structure nor the beam coherence. Summarizing, beryllium parabolic refractive lenses are promising candidates for microanalysis at an XFEL facility.

## 5.8  Comparison and Outlook

Hard X-ray microscopy, scanning tomography, hard X-ray lithography, and micro small angle scattering were implemented with rotational parabolic refractive lenses made of aluminium. Beryllium parabolic refractive X-ray lenses are a high quality optic device. The energy range from 5 keV to 25 keV can be covered in an optimal way. The improvements for the optical parameters like resolution, field of view, field of depth, transmission, beam divergence, magnification, and coherence maintenance are useful for the applications considered here. The great variety of techniques and applications is a result of the lens design. It is easy to

adapt the number of lenses to the need. In the near future, the beryllium lenses will be even improved.

- The number of lenses must be increased for shorter focal lengths, which would be responsible for higher magnification factors. In that way, the resolution of hard X-ray microscopy can be enhanced.

- More time will be spent in the development of additional manufacturing steps to improve the optical quality of the lens material and surfaces. Because of the desire to reach the theoretical limits of each application even less important items of the parameters of refractive lenses have to be improved, e. g. roughness, thickness, or material inhomogeneities.

- The possible aperture will be expanded to more than 1 mm for some single lenses. Such an objective would capture more divergent synchrotron radiation beams than is possible up to now. With a focal length of about 5 m to 10 m, a more intense beam with less divergence will be generated for direct use, e. g. in small angle scattering or in nanofocusing.

The refractive lenses themselves are just optical elements. Their scientific benefit is due to the wide spectrum of applications. The experiments described here were built up to implement the methods and to demonstrate possible improvements due to Be lenses. Now, specific questions from physics but also from material and environmental science as well as from biology are envisaged.

**Magnifying Tomography:**  the Be lenses will be used to carry on the development of this method; the aim is a resolution below 100 nm.

**XFEL optics:**  the development of the parabolic refractive X-ray lenses is connected to improvements in synchrotron radiation sources. Only the brilliance of 3rd generation synchrotron radiation facilities showed the usefulness of refractive X-ray lenses. The next step on this way will be the X-ray free electron laser, XFEL. This will be the ultimate test for the performance of Be lenses.

**Other applications:**  in the last years, more and more scientists become used to refractive X-ray lenses and more ideas to use them will show up. Methods will be implemented, taking care of the specialities of Be lenses. Micro diffraction tomography can benefit from higher intensities and from an easy alignment. Micro small angle scattering will profit from refractive lenses.

# Chapter 6

# XANES Microtomography

X-ray absorption near edge structure, XANES, is a well established analytical method for the local and atomspecific electronic structure in condensed matter with the emphasis in bond angles and coordination geometry. As part of X-ray absorption fine structures, XAFS, its theory is sketched in the following section. Scanning tomography was introduced in chapter 5.3 as non destructive analytic method which benefits of the current developments of parabolic refractive lenses. The local sensitivity of XANES and the spatial mapping of tomography are combined with a micro probe technique to improve the spatial resolution. In particular, heterogeneous and/or small sample textures can be analyzed. The experimental realization in section 6.3 describes the complexity of this new combination. Finally, the achieved results, partially published in [43], will demonstrate the significant improvements in XANES and scanning tomography.

## 6.1   X-Ray Absorption Fine Structure (XAFS)

A sample is illuminated with monochromatic X-rays, whose energy is tuned around the absorbtion edge of a specific chemical element. The transmitted intensity is given by the Lambert-Beer law

$$\mathsf{I}_{Abs}(\mathsf{E}) = \mathsf{I}_0(\mathsf{E}) \cdot e^{-\mu(\mathsf{E}) \cdot \mathsf{d}} \quad . \tag{6.1}$$

The measured intensity $\mathsf{I}_{Abs}$ is exponentially attenuated with the thickness $\mathsf{d}$ of the material, and with its attenuation coefficient $\mu$, which is a function of the energy.

Absorption dramatically increases at an absorption edge. The energy of the edges is increasing with higher $\mathsf{Z}$ and decreasing with higher shells. Figure 6.1 illustrates these effects. The attenuation coefficient $\mu$ is plotted versus the energy in the vicinity of the K-absorption edges of atomic Cu ($\mathsf{Z}$=29) and Zn ($\mathsf{Z}$=30) as well as the K- and L-edges of Pd ($\mathsf{Z}$=46). The location of the edges is element specific. The K-edges of the neighboring elements Cu and Zn are clearly distinguished.

After absorption of a photon, the atom is excited. Depending on its kinetic energy, the electron will be excited into the continuum or it may occupy an empty valence orbital. After absorption, the excited atom will return to the ground state by Auger emission or by fluorescence emission. Auger emission dominates for small excitation energies, whereas fluorescence dominates for deep core excitation. Absorption edges in atoms are marked by an abrupt increase in absorption when the photon energy exceeds the edge energy. At the same time, Auger yield and fluorescence increases dramatically. In condensed matter and molecules a
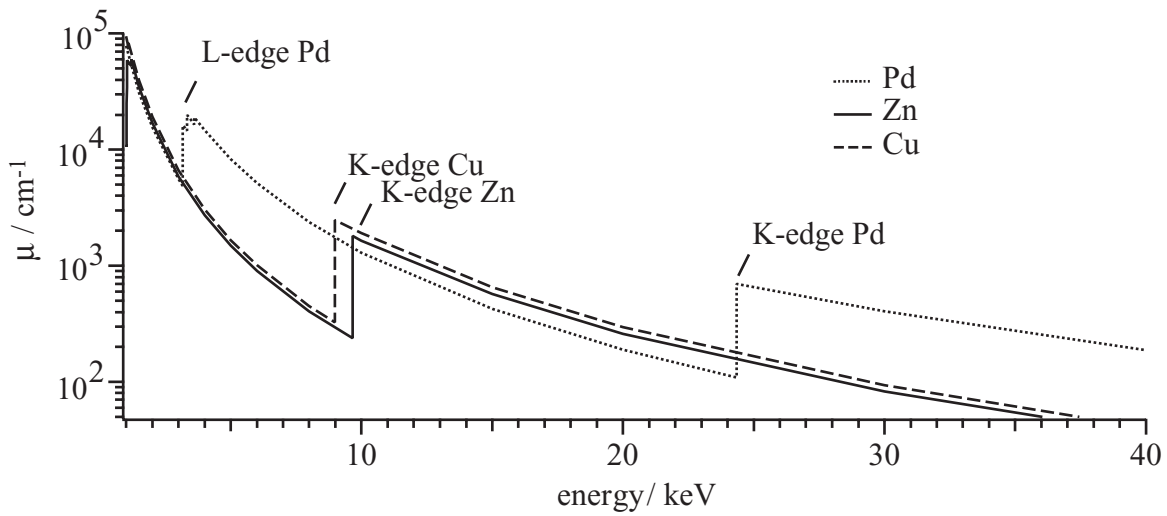
Figure 6.1: Absorption edges of the atomic elements Cu, Zn, and Pd within $1\,\mathrm{keV}$ - $40\,\mathrm{keV}$ (data taken from [44]).
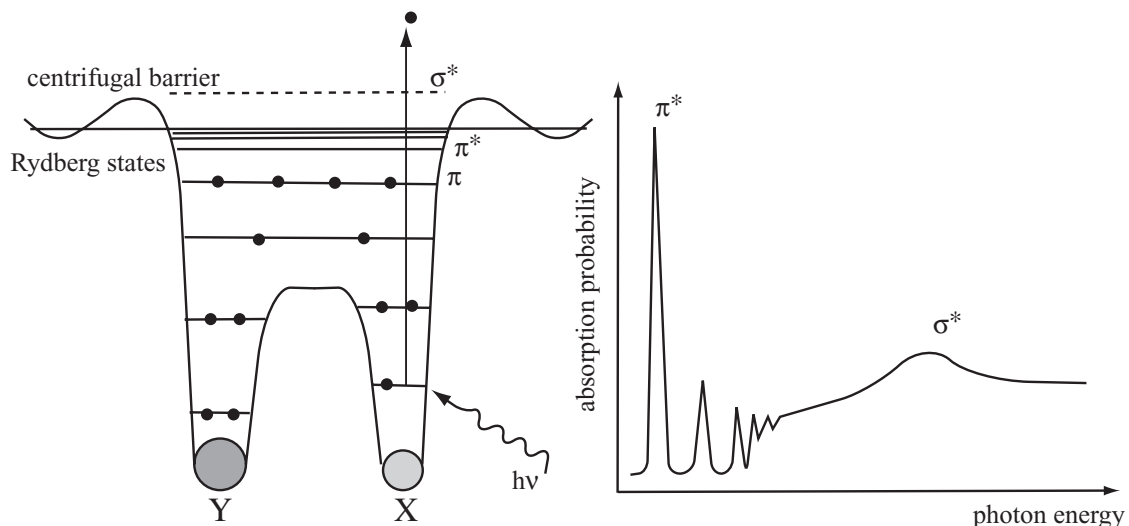


Figure 6.2: XANES in a simple two atomic molecule (according to [45]).

fine structure is observed in the absorption at the edge and above it. Figure 6.2 demonstrates the origin of a XANES spectrum for a simple two atomic molecule. The K-edge of atom X is exceeded by the exciting photon $h\nu$. With increasing photon energy the first empty electronic states will be occupied by the photoelectron. They give rise to sharp features in the absorption. In the case of figure 6.2, the molecular $\sigma^*$ anti bonding state is the highest bound end state before the excitation occurs into free states. XANES can study the local order in complex systems. As a matter of fact, molecules, clusters, surfaces and heterogeneous solids can be analyzed, because no periodic structures are needed. Later in this chapter this will be shown by the analysis of biological samples and porous catalyst grains.

In condensed matter an extended X-ray fine structure (EXAFS) is observed which may be extend to 1 keV above the edge. It is due to interference of the outgoing and backscattered photoelectron wave which is scattered by atoms in the neighborhood of the absorbing atom. Figure 6.3 illustrates constructive and destructive interference. For constructive interference the probability for finding the photoelectron outside of the absorber is larger than without neighboring atoms. The absorption shows a maximum. On the contrary, for destructive interference the probability to detect the photoelectron outside the absorber is lower than without neighbors; $\mu(\mathsf{E})$ has a minimum. In general, $\mu(\mathsf{E})$ varies between these two extremes as a function of the photoelectron wave vector $\mathsf{k}$ which is linked to the photoelectron energy $\mathsf{E}_p = \mathsf{E} - \mathsf{E}_0 = (\hbar^2 \mathsf{k}^2)/(2m)$. Here $\mathsf{E}$ is the photon energy and $\mathsf{E}_0$ is the binding energy of the photoelectron prior to absorption.

In the following sections XANES spectra are analyzed in detail, whereas the EXAFS oscillations are considered in regard to their disturbing influences on them. Therefore, the EXAFS theory is left to the textbooks [46, 47].

Here, only K-edges of different atoms will be analyzed. These edges are preferred due to the clearer evidence they provide. In the first place this is because the edges with higher energies are well separated from other edges resulting in little disturbances from other absorbers. The overall absorption cross section for hard X-rays is weak and follows a decreasing Victoreen function with increasing energy [45]. A higher sample transparency due to a high X-ray energy is an advantage. The use of beryllium as lens material makes more K-edges accessible compared to a refractive lens optics made of aluminium. In particular, within the energy range from 5 keV to 20 keV the K-edges of the element Cr to Mo can be analyzed.

A measured Cu K-edge spectra is shown in figure 6.4. The attenuation coefficient $\mu$ is displayed versus increasing photon energy. The different analytical energy regions are specified within the figure. As definition of the edge, we use the position of the first inflection point of the edge jump, which is marked by a dashed line at 8.979 keV. The edge region and the first peak are formed by the orbital transitions 1s to 4p. It is noteworthy that the edge structure and the edge position vary with the valence and the type of coordination of the absorber atom. For instance, they differ substantially between copper metal and the different copper oxides. The strong XANES peaks are followed by the EXAFS structures which are measurable beyond the Zn K-edge at 9.565 keV.
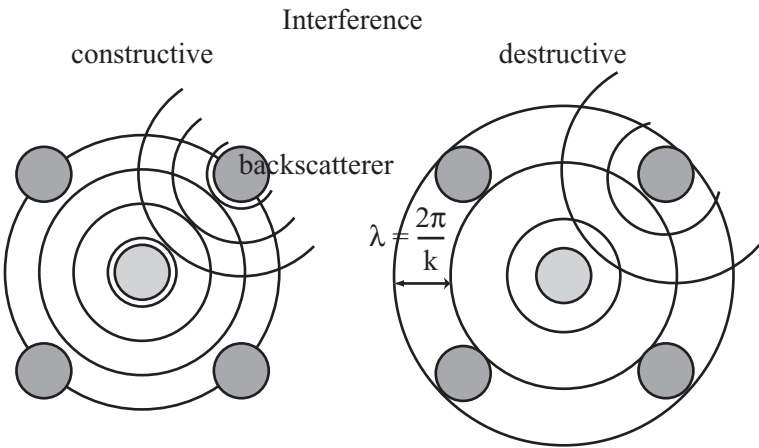
Figure 6.3: EXAFS due to the interference of outgoing and backscattered photoelectron waves.
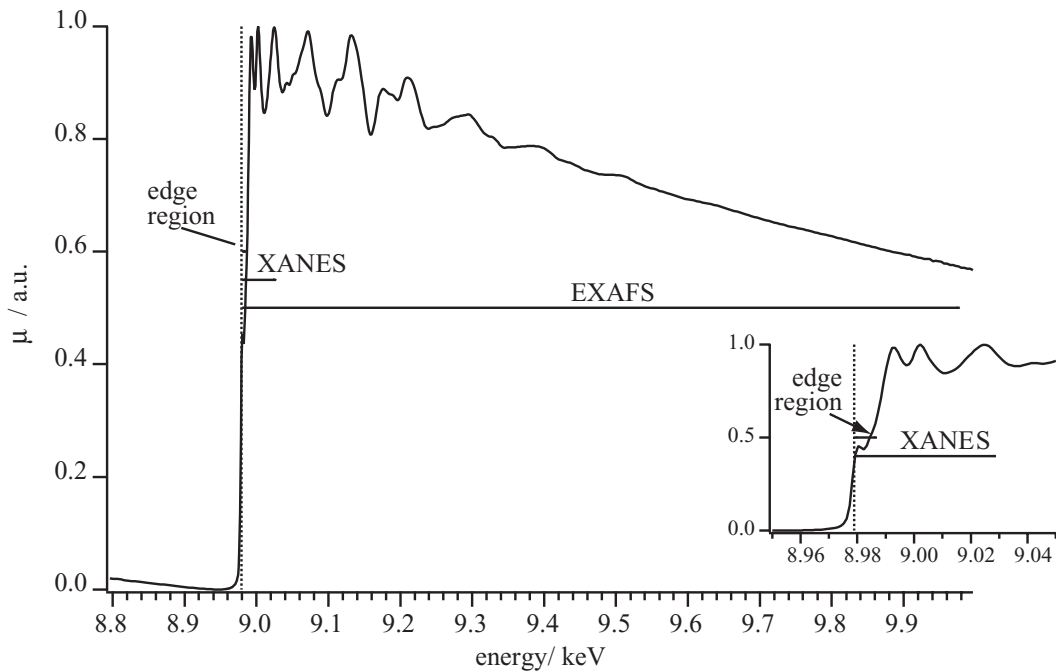


Figure 6.4: Full EXAFS spectrum of a copper foil at the Cu K-edge (8.979keV). The different analytical energy regions are specified. The XANES range is stretched, (inset right-bottom).

## 6.2 The Goal: XANES Microtomography

The goal is to get a virtual slice through a sample by means of a tomographic reconstruction based on XANES spectra.

The resolution of a full XANES spectrum should be ~1 eV and at least 50 eV of the edge region are needed to analyze it. The number of pixels of a tomogram depends on the sample size and on the desired resolution. A sample of $500\,\mu$m in diameter which is scanned in $10\,\mu$m steps can be recorded with $56$ translations $\times 101$ rotations. If one needs only 1 second for each measurement, the acquisition would unrealistically take over 3 days. These minimal considerations include no time-outs for motor movements, and no darkfield (detector laps), or no flatfield (background scattering) corrections are considered, both being needed. The inner circle in this experimental setup is the monochromator movement. In that respect the key to realize XANES microtomography is a Quick EXAFS monochromator, which in the first case was designed for fast *in situ* analysis. Using a cam-driven monochromator, which is developed by the University of Wuppertal, scans over $1\,$keV with $10\,$Hz are feasible, with best energy resolution. The fast monochromator movement dictates the data acquisition rhythms and is synchronized with the scanning tomography setup. The use of beryllium lenses increases the signal intensity in a manner that only a few seconds of acquisition time are needed for each measuring point. XANES Microtomography is feasible with this strategy, only.
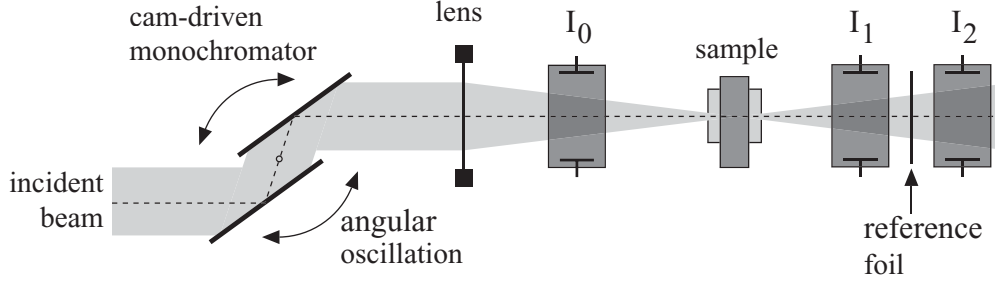
## 6.3 Experimental Implementation

The general experimental setup of XANES microtomography is illustrated in figure 6.5. The white beam of a synchrotron radiation source is monochromatized in a cam-driven monochromator. Higher harmonics are rejected by external total refection on a mirror or by slightly detuning the Si(111) or Si(311) crystals of the monochromator. The monochromatic energy values describe a full sinusoidal path over a range of $2.5\,$keV. It is the newest development based upon the first QEXAFS monochromator introduced by Frahm [48]. The fast scanning monochromator is fully characterized in the PhD thesis of Matthias Richwin, University Wuppertal, [49, 50].

At a bending magnet no cooling of the monochromator crystal is necessary. A tapered undulator source with 10 times higher flux demands a liquid nitrogen cooling. There was no need for a fixed exit monochromator, since the fixed optical axis of the parabolic refractive lenses compensates for the beam movements over the lens aperture; possible intensity variations are continuously recorded.

In the present experiment 59 Be lenses were used, with a transmission of 4.5% and a gain over 10 000. The incident intensity $I_0$ is measured with an ionization chamber (15 cm long) right in front of the sample, which is positioned on a tomographic stage. The main concerns here are the eccentricity of the rotational axis and the synchronization with the fast scanning monochromator. This is realized by a continuously moving monochromator and an acquisition system waiting for the stage movements. False spectra, due to still existing deadtimes, are eliminated during the data analysis. The transmitted intensity $I_1$ is also recorded by an ionization chamber, positioned right behind the sample. A metal foil of the analyzed element is used as reference sample to verify the energy. The transmitted intensity $I_2$ of the reference is measured in the last ionization chamber which is twice as long (30 cm). The detection with ionization chambers was chosen because it allows for fast data acquisition. The fluorescence

Side view:



Top view (sample region):
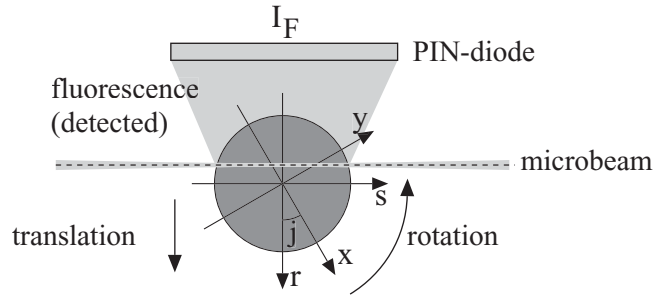


Figure 6.5: Setup of the XANES Microtomography experiments [43].

$I_F$ is recorded by a PIN diode perpendicular to the direct beam to minimize the disturbing effect of the elastic scattering. A wavelength dispersive detector was not implemented, as the required readout times would unacceptably slowdown the whole measurement.

The following examples will describe the high potential of the combination of tomography and XANES spectroscopy.

## 6.4   Results of XANES Microtomography

The following examples should demonstrate the various applications and problems for this method. First, the results at the bending magnet beamline BM5 of the ESRF showed the feasibility of XANES microtomography. A CuO/ZnO catalyst was analyzed at the 1-ID (APS, SRI-CAT) station. Problems encountered with the neighboring Cu K-edge and the Zn K-edge in a tomographic reconstruction will be discussed. Finally, the need of an undulator beamline is emphasized for biological and environmental science experiments, in particular for a XANES microtomogram of a tomato root.

### 6.4.1   Feasibility Test

The bending magnet beamline BM5 at the ESRF is a low-$\beta$ station with a source size (FWHM) of $240\,\mu$m in horizontal and $80\,\mu$m in vertical direction. It generates a maximum flux of $2.7 \cdot 10^{13}\,$ph/s/mrad$^2$/0.1%BW. In our experimental setup the monochromatic beam passes through the lens at $38\,$m distance from the source. The basic setup for XANES microtomography was discussed in the last section and is shown in figure 6.5. As optical element 29 single Be lenses were used which generate a $6\,\mu$m $\times\,2\,\mu$m microspot at a focal length of $0.8\,$m.
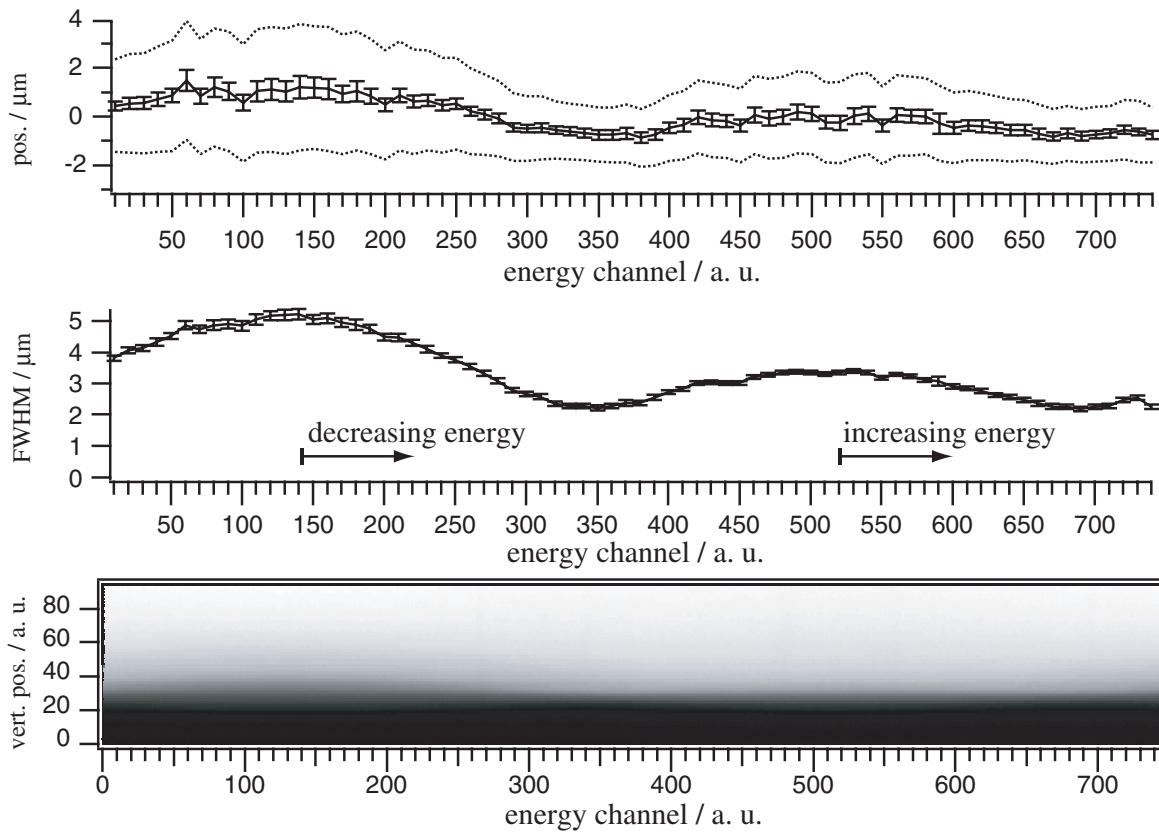
Figure 6.6: Presentation of knife-edge scans with varying energy. (Bottom) Knife-edge scans at all energies of a full period of the cam driven monochromator. The measured intensity is coded in gray scales. (Middle)The knife-edge scans are fitted by error functions. The FWHM of their gaussian derivation at equidistant energy steps is plotted, demonstrating the energy dependent focal length of the refractive lenses. The minimal spot size is given by the minimal FWHM as a function of the energy. (Top) The stability of the monochromator-lens is system analyzed by the position of the focal spot. The relative edge position with its fitting error and the corresponding size of the focal spot are displayed.

A microfocus is characterized by knife-edge scans. The spot size for a given photon energy is measured at different distances from the lens to find its minimum. Here, the fast scanning monochromator is extremely helpful to align the lens. A common knife-edge scan is measured while the QEXAFS monochromator rocks its full period, generating a sinusoidal path with increasing and decreasing energy. The results of the knife-edge scans are shown in figure 6.6(bottom). For each energy channel the movement of the knife-edge through the beam was measured. First, the full beam is detected, light points. When the edge is moved into the beam the spot is more and more covered until the beam is totally blocked by the sample, dark points. In this way, the focal length of the refractive lens is directly measured. The energy of the minimal width of the knife-edge scans can be translated into the correct focal length of the experiment. In figure 6.6(middle), where the fitted FWHMs are plotted for every tenth scan, the minimal spot size is $2.2\,\mu\mathrm{m}$.

Another characteristic of the microspot can be demonstrated by means of such knife-edge scans at various energies. It has been mentioned that any displacement of the beam by the QEXAFS monochromator parallel to the optical axis will be compensate by the refractive lens. Any angular change of the beam at different energies would lead to a not tolerable change in the analyzed volume of the sample. Information of the stability of the microspot is needed. Therefore, the fitted positions of the knife-edge scans are analyzed, figure 6.6(top). The center positions of the fits are plotted and the fitting errors are displayed, the corresponding spot size is shown as envelope of dotted lines. To understand the results it has to be mentioned that the used knife-edge had wedge shape. So the gaussian profile of the beam was convoluted with the increasing absorption of the knife-edge. This results in the relative shifts of the beginning of the edge and of its center. Whereas the position of total absorption of the beam is stable over the complete energy range by at least $\pm 0.1 \, \mu$m. The artefact due to the design of the knife-edge is negligible for this value. The excellent beam stability documents the performance of the monochromator and the optic.

The technique is now applied to a partially oxidized copper wire $50 \, \mu$m in diameter. In figure 6.7(1) the object is shown in magnification. Obviously, the image suffers from the poor depth of sharpness of light microscope images. Nevertheless, one can clearly distinguish between the red copper(I)oxide [$Cu_2O$] and the black copper(II)oxide [$CuO$]. A scratch in the oxides reveals the metallic copper core. These copper species have only slight differences in their XANES spectra and were chosen as test material for that reason. The differences in the full XANES spectra allow to distinguish between the Cu species, but there are no energies at which single measurements would be likewise sufficient.

A scanning tomogram is recorded at a virtual slice through the sample. A XANES analysis is carried out for each combination of a rotation angle and a translation position. The incident intensity $I_0$, the transmitted intensity $I_1$, the intensity $I_2$ behind a $12 \, \mu$m thick reference Cu foil and the fluorescence radiation $I_3$ are measured 300 times when the QEXAFS monochromator rocks back and forth through an energy range around the Cu K-edge. Figure 6.7(2) shows a typical scan. The edge region is covered twice, once with increasing and once with decreasing energy. Each spectrum is energy calibrated relative to the Cu signal. 32 projections with 25 translation steps were recorded for $60 \, \mathrm{s}$, in order to get the required data statistics. The reconstruction of the tomograms is as described in section 5.3, however the data for the whole XANES region have to be processed. As a consequence, a sinogram is generated for each energy step. In the actual example there are 380 energy steps within an edge region and a total of 950 energy points were measured. Figure 6.7(3) presents two sinograms. The first below the Cu K-edge and the other above the edge. The diagrams illustrate in their colors the attenuation coefficient. The striking differences in the images of figure 6.7(3) reflect the composition of this test sample. Finally, part (4) of figure 6.7 shows reconstructed tomograms. The first tomogram belongs to an energy above the Cu K-edge. Obviously, the sample was too absorbing so that artifacts were introduced into the reconstruction resulting in a darker center in the absorption image. The tomograms of figure 6.7(4) illustrate that the metallic copper core inside the sample was detected, but only the $Cu_2O$ surface layer was found. Due to the resolution of $5 \, \mu$m per projection, due to the high total absorption, and due to insufficient data statistics existent CuO at the surface was not detected. A better resolution in the tomogram can be achieved but only if the photon flux in the focal spot can be increased. This required an undulator beam line. The intensity from a bending magnet is not sufficient.
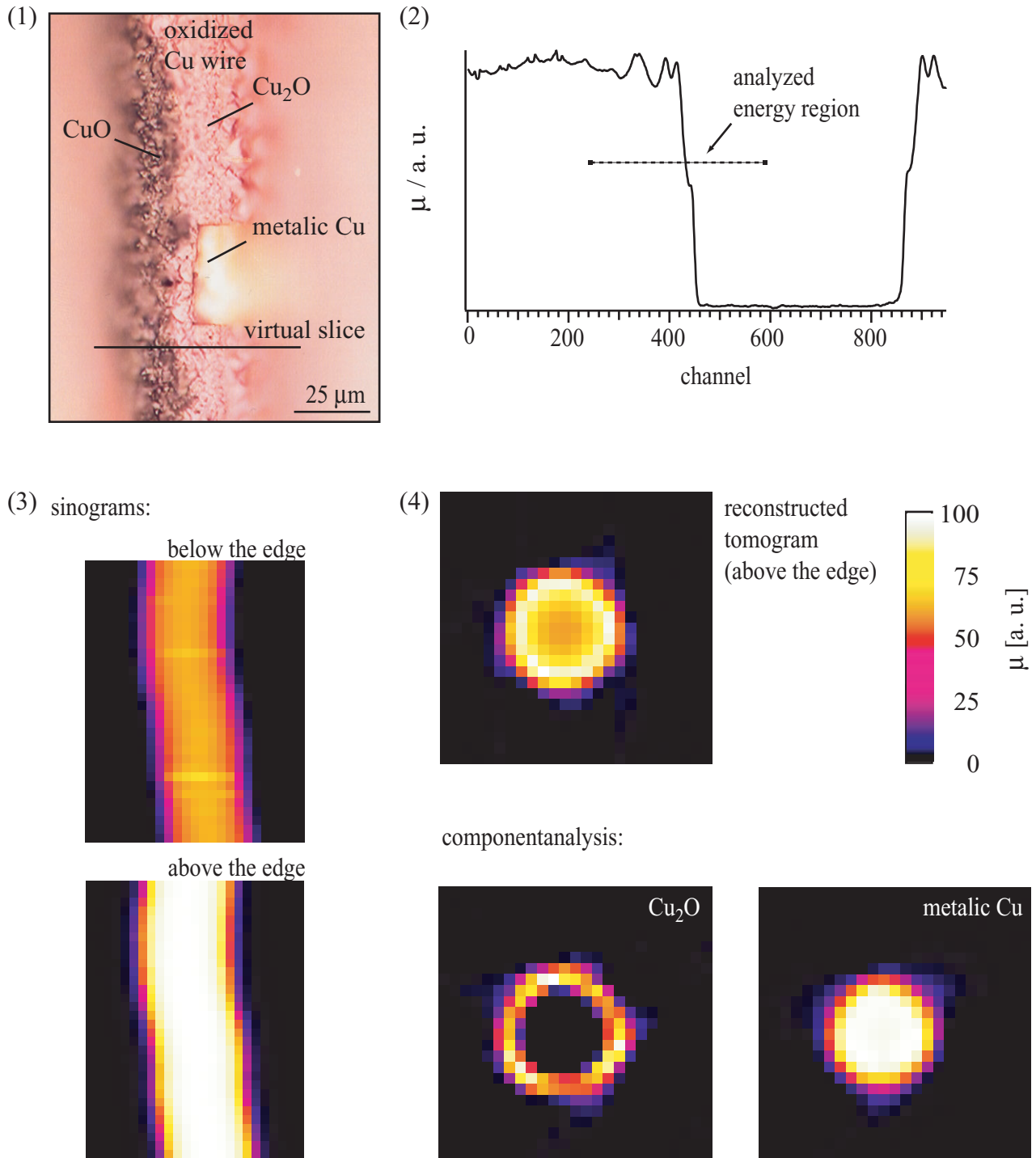
Figure 6.7: XANES microtomography analysis of an oxidized Cu wire.
(1) Microscopy of the oxidized Cu wire illustrating the different Cu species.
(2) A measured single XANES spectrum
(3) Recorded sinograms above and below the Cu K-edge.
(4) Tomogram above the Cu K-edge and the component analysis based upon reference spectra.

### 6.4.2   Catalyst Science

The search for effective catalysts is an important task in chemistry and chemical technology. X-ray absorption spectroscopy, and in particular XANES, is an excellent analytical tool for studying heterogeneous catalysts. As an example, we consider a CuO/ZnO catalyst used in methanol synthesis. XANES studies have been reported for this system [51, 52]. The Institute of Chemistry and Bioengineering of the Swiss Federal Institute of Technology has built a reactor to control the environment of the catalytical reaction. *In situ* experiments were carried out, in particular with EXAFS studies [50, 53]. The central part of this reactor is a glass capillary filled with a granular catalyst embedded in a boronnitride matrix. For our XANES microtomography we have chosen such a reactor capillary. The capillary was filled with a 30% CuO/ZnO catalyst that was twice reduced and reoxidized by 4% $H_2$/He and 2%$O_2$/He at 200°C - 300°C. The reduction/reoxidation was checked by QEXAFS. After the final reduction the grown Cu-particles on ZnO were reoxidized at room temperature.

### ... at the Cu K-edge

First the beam was tuned to the Cu K-edge at 8.979 keV. A slice through the capillary was scanned at 90 equidistant lateral positions. We have used a beryllium refractive lens with $N = 51$ and a focal length of 0.479 m. Two reconstructed tomograms, one above and one below the edge, are shown in figure 6.8(1a,b) [25]. The perfect circle of the glass capillary is visible. Since the glass contains no copper the signal from the capillary is the same below and above the Cu K-edge. On the other hand, the Cu and Zn catalyst, inside the glass tube, show strong variations in absorption below and above the edges. In a XANES microtomography a full X-ray energy scan is taken at each tomographic position. A total of 90 000 XANES spectra have been taken. Reconstruction allows to calculate the XANES spectrum for each pixel in the sample. Examples are given in the figure 6.8(1c): pixel 5 in the glass capillary shows no edge structure near the Cu K-edge, since it contains no copper. The pixel 1, 2, 3, 4, and 6, on the other hand, all show a Cu K-edge. In order to identify the type of Cu in the catalysts, three Cu reference samples have been measured under identical conditions as the catalyst: metallic Cu, monovalent copper oxide $Cu_2O$ and divalent copper oxide CuO. It turned out that all of the spectra for the catalyst were mixtures of the three reference spectra with different fractions for different pixels. For instance, pixel 2 contains 48% Cu and 52% $Cu_2O$, while pixel 6 contains 37% Cu and 63% $Cu_2O$. The overall result is shown in figure 6.8(part 2). Figure 2a gives the metallic Cu content whereas figure 2b gives the $Cu_2O$ contribution. The fraction of CuO was always below the detection limit due to the fitting errors (about 2%).
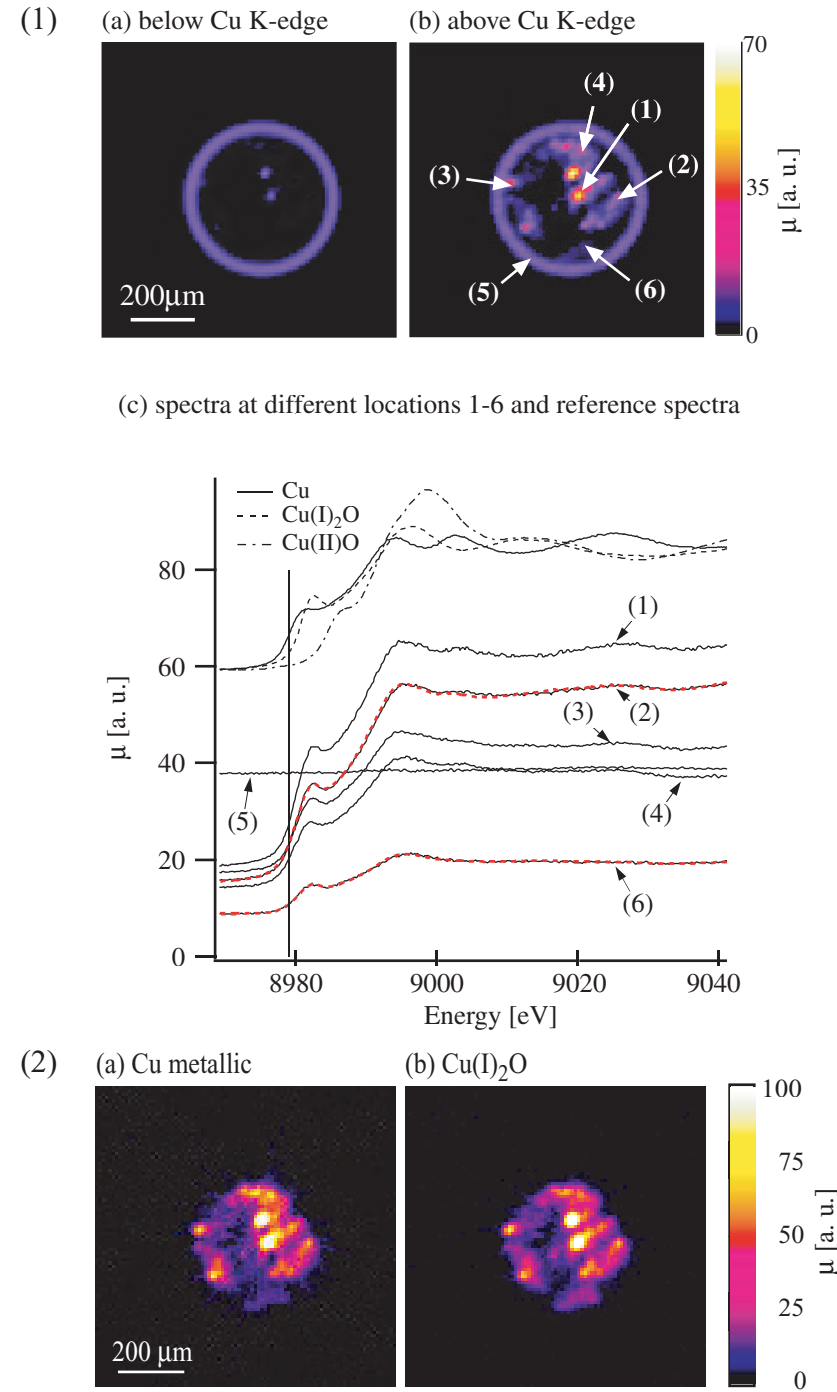
Figure 6.8: XANES Microtomography of a CuO/ZnO-Catalyst at the Cu K-edge: (1) recorded tomograms (1a) below and (1b) above the edge. The spectra measured in the different pixels 1-6, (1c), turned out to be combinations of the spectra for Cu (2a) and $Cu_2O$ (2b) with different fractions of both in different pixels. [43]
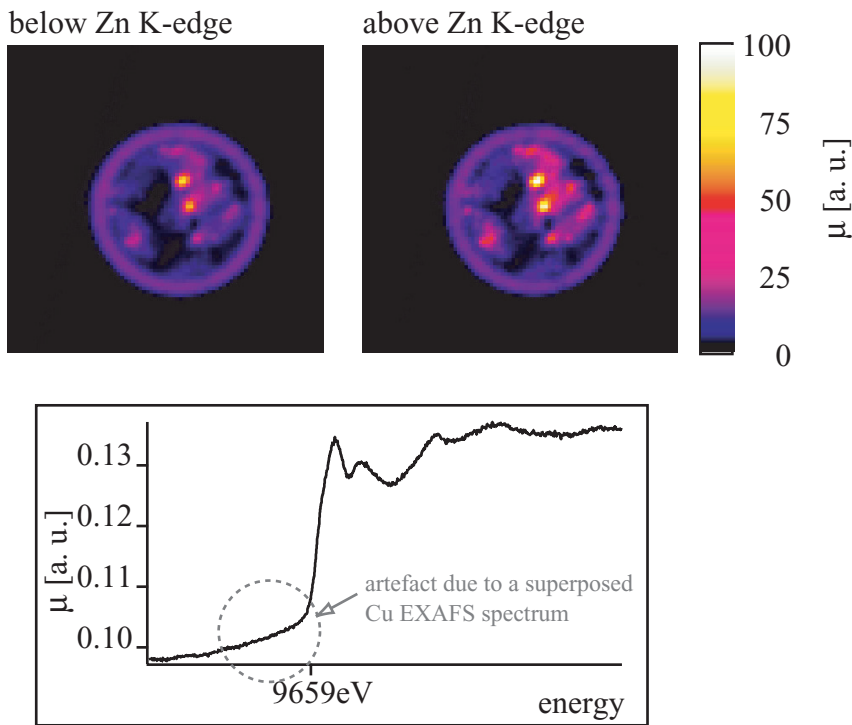
Figure 6.9: (Top) Recorded tomograms of the CuO/ZnO-Catalyst above and below the Zn K-edge. (Bottom) Reconstructed XANES spectrum at the Zn K-edge demonstrating the influence of Cu species therein.

### ... at the Zn K-edge

The Zn K-edge is located $680\,\mathrm{eV}$ above the Cu K-edge. In order to keep the experimental setup as similar as possible for the Cu and Zn XANES measurements 8 additional Be lenses have been added to the stack so that the focal length is kept identical at both edges. All other parameters were also kept similar: 101 rotation over $360°$, $10\,\mu\mathrm{m}$ horizontal step size, monochromator scanned with $10\,\mathrm{Hz}$, data points recorded at $0.037\,\mathrm{eV}$ step size, total measuring time about 6 hours.

Figure 6.9(top) shows the tomograms below and above the Zn K-edge, at $9.659\,\mathrm{keV}$, for the same virtual slice as in figure 6.8. A few points are noteworthy: (1) it is possible to probe the same cross section of the sample at different energies; shifts in beam position are negligible. (2) The cross section under investigation contains Zn, as indicated by the increasing signal above the Zn K-edge. However, at the Zn K-edge, copper is still contributing to the signal.

### 6.4.3   Biological and Environmental Science

Zinc (Zn) is a very common trace element in plants. However, the natural concentration of free Zn is typically below 1 ion per cell. It is needed as receptor and for transport processes in a plants. However, in higher concentrations Zn is a heavy metal pollutant.

In our case the sample was a root of a tomato plant living in symbiosis with the fungus mycorrhyzal. The plant was grown on a soil, which was polluted with zinc and lead and which was also inoculated with the fungus. This biologic system is studied by W. Schröder at the Institute of Chemistry and Dynamics of the Geosphere III: Phytosphere, Research Center Jülich. It is investigated how such symbiotic plants are able to withstand the polluted environment. This understanding is essential to renaturalize areas with destroyed ecological system. The overall concentration of Zn in the root of the tomato plant was below 100 ppm. This still low concentration was analyzed with XANES microtomography in order to determine the spatial composition of the Zn in the root and to additionally examine its chemical state.
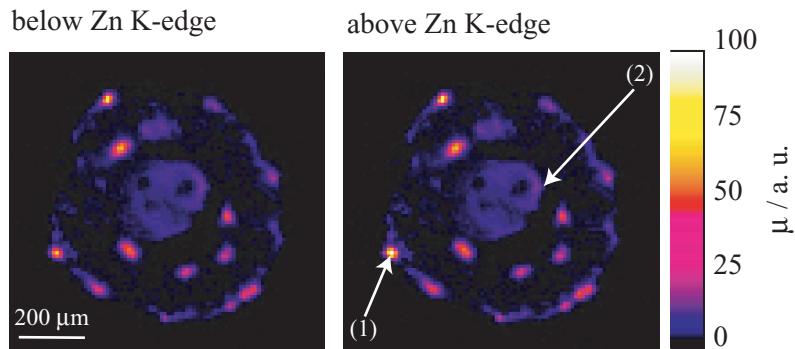
The analyzed section of the root is about 700 $\mu$m in diameter. For the XANES microtomogram the root was scanned with 87 translations and 101 rotations over the full 360°. Therefore, a resolution of 10 $\mu$m was achieved for the tomograms shown in figure 6.10(a). The measured distribution of Zn was already known from former scanning tomography experiments [23]. The Zn concentration is high at the border of the root. Zn is the strongly absorbing species in an otherwise low absorbing biological matrix. Inside the sample, some pixels show significant absorption at photon energies above the Zn K-edge. This region is of interest in terms of transport processes in the tomato plant. The difficulties with the dilute concentration, which is typical for biologic samples, becomes visible in the reconstruction of the absorption measurements. Whereas the tomograms of figure 6.10(a) below and above the Zn K-edge, at 9.659 keV, detected an increase in absorption, it was not possible to reconstruct XANES spectra for all pixels of interest. To illustrate this, two pixels are analyzed in detail. For pixel (1) the highest Zn concentration was measured, and the reconstructed XANES spectrum shows an edge structure, figure 6.10(c). On the other hand, for pixel (2), positioned inside the root, no edge structure occurs, figure 6.10(d). Both pixels are typical therein for the regions at the border and inside the root, respectively.

Based only on the information of the absorption measurements the aim of the experiment, the determination of the Zn species for a virtual slice of the root, would not be accomplished. Hence, the fluorescence emitted by the sample is needed. In figure 6.10(b) the fluorescence data are illustrated for the same incident photon energies as for the absorption. In general, the measured intensity of fluorescence is less than the transmitted intensity. But the disturbances due to more absorbing components (here Pb in respect to Zn) are less, too. Therefore, the fluorescence tomograms of figure 6.10(b) were recorded. They show a significant increase of the fluorescence intensity above the Zn K-edge.
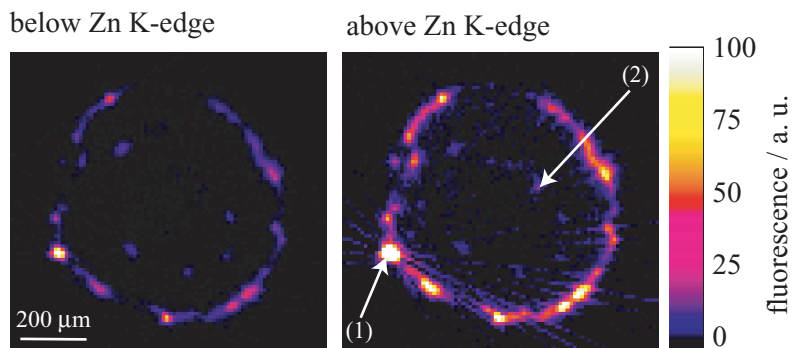
The fluorescence intensity inside the root is very weak. Nevertheless, for one region inside the sample, 12 connected pixels around the marked pixel (2), a Zn XANES structure was reconstructed.

Because of the different origin of fluorescence in respect to the absorption the reconstruction algorithms slightly differ in both cases [54, 35]. Further, selfabsorption effects have to be considered in the fluorescence signal. Since the sinogram of the tomato root in figure 6.11 shows no significant intensity fading the selfabsorption correction was not implemented in this case. An algorithm to correct the selfabsorption for fluorescence tomography was introduced in [35], but it considers incident radiation away from the absorption edges of the sample components. In the future, a correction algorithm for selfabsorption in the reconstruction of XANES fluorescence tomography will be implemented based on the simultaneously recorded absorption.
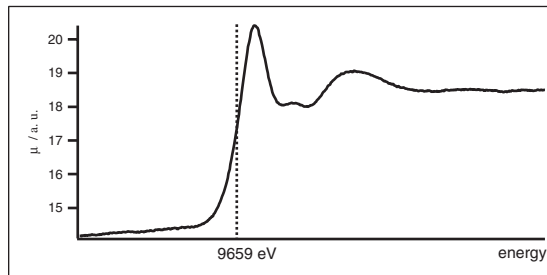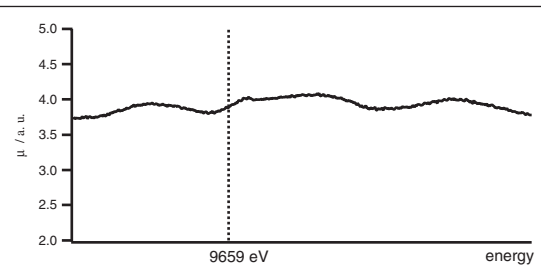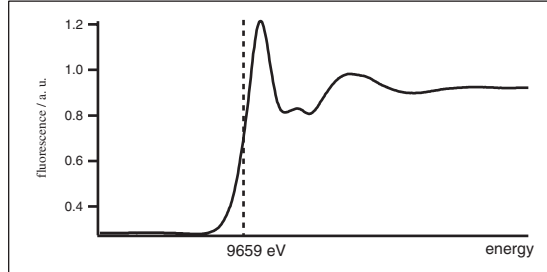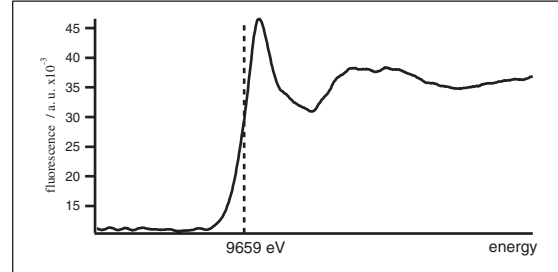
Figure 6.10: Reconstructed tomograms of a tomato root in (a) absorption and in (b) fluorescence, each recorded before and above the Zn K-edge. (c-f) For the marked pixels the reconstructed XANES spectra are plotted.
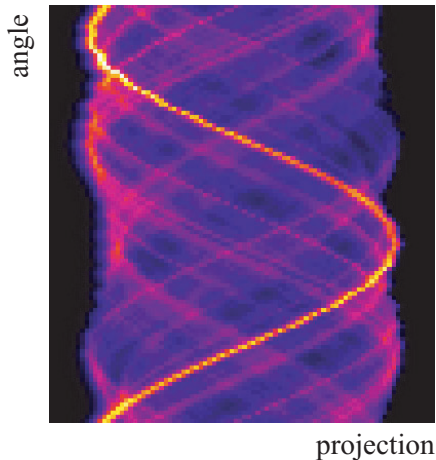
Figure 6.11: Sinogram for the fluorescence measurement of the tomato root, illustrating selfabsorption effects inside a sample.

A chemical analysis of the XANES fluorescence tomograms is possible, even though the signal intensity of pixel (2) in figure 6.10(e) shows only ~4% of the signal in the border region, figure 6.10(f). Whereas the edge position in both fluorescence spectra is the same the curves show different structures when the first peak decreases. These fine structures are not generated by one single Zn species which was verified by reference substances. A detailed component analysis will be carried out in the near future.

Up to now, it can be summarized that the high flux of the undulator synchrotron radiation source at beamline 1-ID/APS has made a chemical analysis possible. The dilute concentration of Zn in the root of a tomato plant can be analyzed by XANES microtomography in fluorescence mode.

## 6.5 Conclusions

XANES microtomography combines X-ray absorption spectroscopy with a high 3-dimensional resolution; indeed, a full XANES spectrum is measured for each pixel of a tomogram. This opens new opportunities in many field of research, as demonstrated for 2 applications in the field of catalysts and plant physiology. It was shown that neighboring elements in the periodic table, like Cu and Zn, can clearly be distinguished. No assumptions are needed in data acquisition and processing. The XANES spectra can be measured in absorption and in fluorescence. For chemical elements, present in the sample in low concentrations, as for instance in plants, fluorescence is the only adequate spectroscopy. The combination with absorption measurements is needed to correct for the selfabsorption.

Different extensions of the technique can be considered in the near future. X-ray absorption can be extended to a larger energy range in order to cover the EXAFS up to about $1\,\mathrm{keV}$ above the edge. The QEXAFS monochromator is sufficient for that purpose. As shown in [49] this setup is able to cover a range of more than $2\,\mathrm{keV}$ at the Cu K-edge. However, it must be taken into account that chromatic aberration of the refractive lenses generates some problems in large energy scans, due to the change in focal length and a variation of the volume probed in each energy scan. A possible solution is a large focal length of the refractive lens.

As a consequence, the depth of field becomes large and the change in focal length becomes less important. In order to keep the good spatial resolution the X-ray source must be very small, as in a low-$\beta$ undulator. An other approach is the use of achromatic mirrors as focusing optic. In such a case a QEXAFS fixed exit monochromator is needed and new concepts for the sample alignment have to be implemented.

# Chapter 7

# Nanofocusing

There is an increasing demand for analytical tools with submicrometer resolution. Biological cells are in the $\mu$m range. Nanotechnology is able to fabricate structure with 20 nm in size. Since most samples are inhomogeneous in structure X-ray probes should head for a lateral resolution of a few nanometers.

This chapter presents a second implementation of parabolic refractive lenses for hard X-rays. Planar parabolic refractive lenses with an extremely small radius of curvature. A micro/nano probe is the demagnified image of a synchrotron radiation source, which is defined by the design of the synchrotron radiation storage ring and which is fixed in its dimensions (section 5.2). Demagnification can be enhanced by different approaches: In a first approach, the X-ray source can be decreased by slits (Yun et al. [55]) or the source-optic distance $\mathsf{L}_1$ can be chosen very large. This second option can only be realized at special beamlines, the 1 km beamline at SPring8 [56] or the 140 m beamline ID19 at the ESRF [57]. Both solutions suffer from intensity loss.

Here, a different approach is presented which can be implemented in any synchrotron radiation source of the 3rd generation. In the thin lens approximation the minimal focal length of a parabolic refractive lens is

$$\mathsf{f}_{min} = \sqrt{\mathsf{f}_0 l} = \sqrt{\frac{\mathsf{RD}}{2\delta}}. \tag{7.1}$$

$\mathsf{D}$ is the length of an individual lens in the stack of total length l. For a given lens material and a given photon energy, the decrement $\delta$ is fixed. Also, $\mathsf{D}$ is fixed by the aperture of the lens. As a consequence, the radius of curvature $\mathsf{R}$ must be made small in order to get a strong demagnification of the source. A focal length of a few millimeter requires a radius of curvature $\mathsf{R}$ of below 10 $\mu$m. This can no longer be realized with a pressing technique. Therefore, a new design is implemented.

## 7.1 Design and Manufacturing of Nanofocusing Lenses

The fabrication of X-ray refractive nanofocusing lenses has benefitted from the microfabrication techniques developed in semiconductor technology. Aristov et al. [58] have manufactured planar silicon lenses in 2000. Their aim was to optimize the transmission by means of kinoform shapes [21, 16]. Here, the aim was to minimize the focal spot by choosing a value of $\mathsf{R}$ in the $\mu$m range [25]. These lenses are called NFL's nanofocusing lenses.
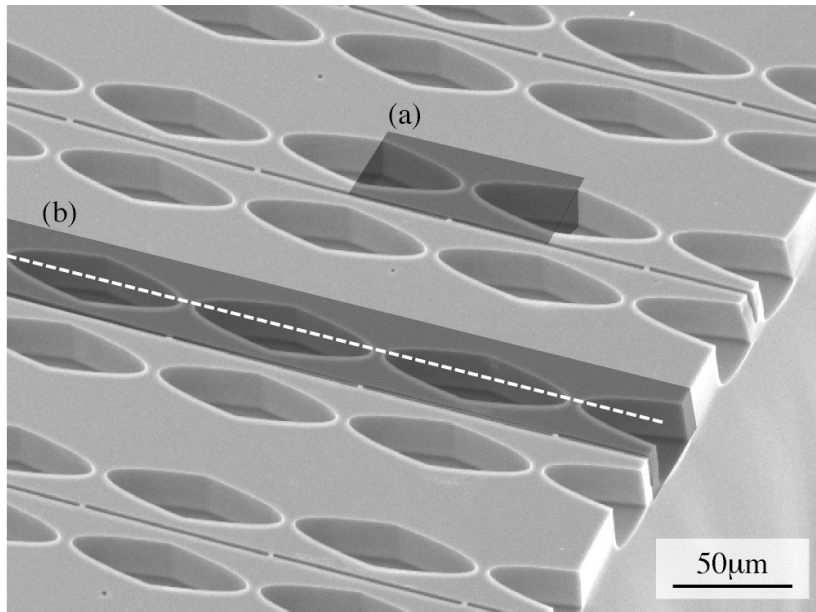
Figure 7.1: Scanning electron micrograph (SEM) of a arrays of silicon parabolic refractive X-ray lenses. The shaded area (a) is a single refractive lens, two complement concave parabolic shapes. Area (b) belongs to an NFL, the optical axis being parallel to the dashed line in the middle of the lenses.[25]

The scanning electron microscope image in figure 7.1 shows a small part of an NFL array. The shaded area (a) shows a single lens, comparable to a single pressed lens. The shaded area (b) belongs to the end of an array of lenses. Eight different NFLs are visible in the image. Manufacturing starts with a silicon wafer thermally oxidized (layer thickness of 300 nm). The next step is the physical vapor deposition of 30 nm chromium. Then the positive electron beam resist PMMA (poly methyl methacrylate) 'AR-P 659.04' is spin coated on top. Figure 7.2 illustrates the following structuring.

(1) E-beam lithography defines the starting structure. Thereby, proximity effects and the problems with underetching of masks during the whole manufacturing are anticipated upon an empirical base.

(2) The first transfer of the structure is done by chemical etching of the layer of chromium by ammoniumceriumIV-nitrate in perchloric acid. After perchloric etching, the Cr can serve as hard mask for subsequent $SiO_2$ etching.

(3) Reactive ion etching (RIE) of $SiO_2$ was done in a 'SENTECH' system. The process parameters were 20 sccm $H_2$ and 5 sccm $CHF_3$ under a pressure of 5 Pa and at a power of 200 W.

(4) When the silicon bulk was reached the Cr hard mask was completely removed by wet etching.

(5) The lenses themselves are etched by commonly available deep trench RIE (co-operation

(1)

e-beam lithography

resist

(2)

wet etching of Cr

(3)

reactive ion etching
of $SiO_2$

Cr

(4)

removing the Cr of
$SiO_2$ hard mask

$SiO_2$

(5)

deep trench etching
of Si

Si
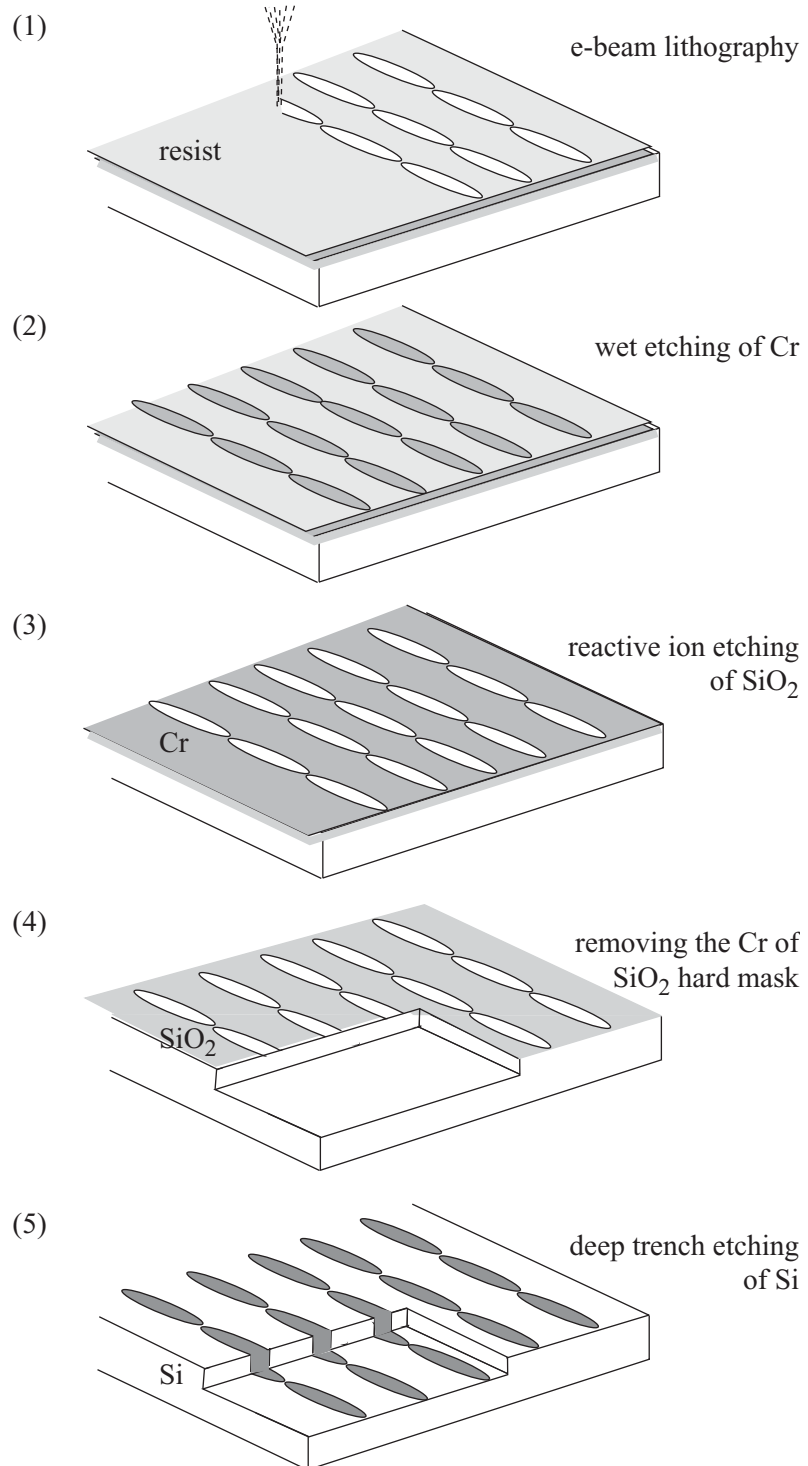
Figure 7.2: Form transfer during the microfabrication of an NFL.

with N. Zichner et al., Technical University Chemnitz).  The thickness of the $SiO_2$ allowed an etch depth of about $30 \, \mu$m.

A number $N$ of individual parabolic refractive lenses is aligned along an optical axis (figure 7.1(b)).  Since the number $N$ can no longer be varied, arrays of lenses parallel to one another with varying radius of curvature $R$, between $1 \, \mu$m and $3 \, \mu$m, provides the flexibility needed. So the NFLs can be adapted to different photon energies or to a different focal length. Figure 7.3 shows the effective aperture $D_{eff}$ versus the radius of curvature $R$ for silicon and boron as lens material. In the calculation, it was assumed that $N = 100$, $E = 12 \, $keV and $L_1 = 40 \, $m.  For $R$ between $1 \, \mu$m and $3 \, \mu$m in silicon the effective aperture is always smaller than $15 \, \mu$m. Due to the the lower absorption resulting in larger effective apertures, boron as lens material is far superior to silicon at $12 \, $keV.
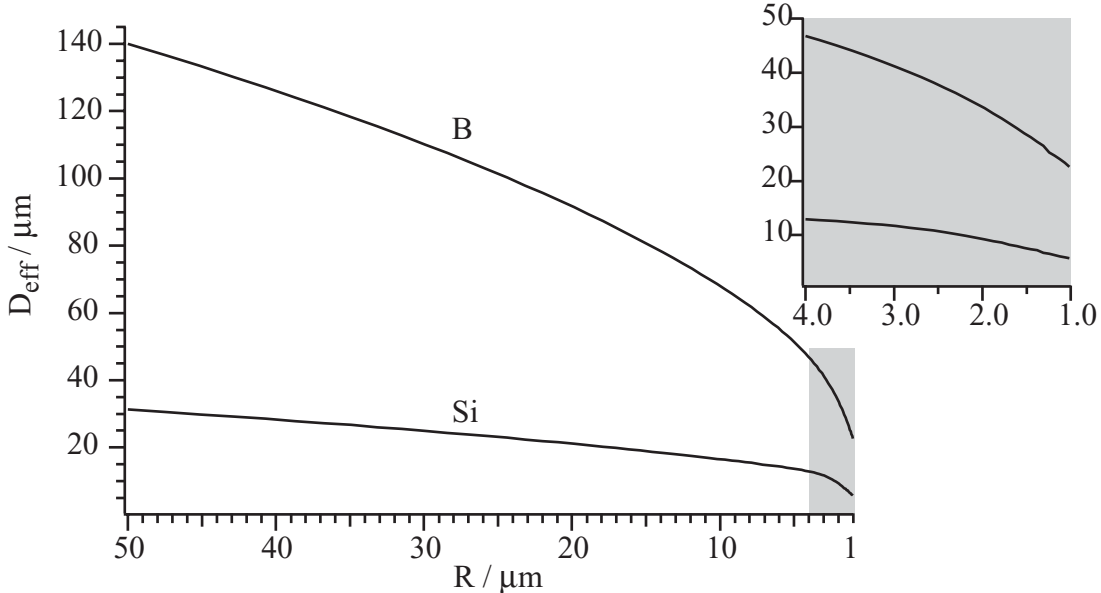


Figure 7.3:  The effective aperture in dependence of the parabolic radius $R$ for the lens materials Si and B. The implemented radii between $1 \, \mu$m and $3 \, \mu$m are shown as grey areas and in the inset.

Planar NFLs generate a line focus and two of them have to be crossed in order to get a point focus. This implementation is sketched in figure 7.4. Consequently, since both NFLs should focus in the same plane (perpendicular to the optical axis) they must have different focal length. This is achieved by NFLs with different a number of lenses, e. g. $N = 50$ vertical and $N = 100$ horizontal. Then the fine alignment is done by the different radii of curvature $R$ for the lens arrays. The specific values to be chosen depend on the X-ray energy and other experimental details.

Microfabrication techniques are best established for silicon, but silicon is not the optimum material for NFLs as shown in figure 7.5. Silicon, aluminium, diamond, boron, and beryllium are compared. The parameters chosen are $N = 100$ and $L_1 = 40 \, $m. The lateral resolution $d_t$ varies strongly with photon energy and with lens material. Due to the manufacturing the radii of curvature $R$ are limited to the range between $30 \, \mu$m and $0.8 \, \mu$m for NFLs. Therefore,
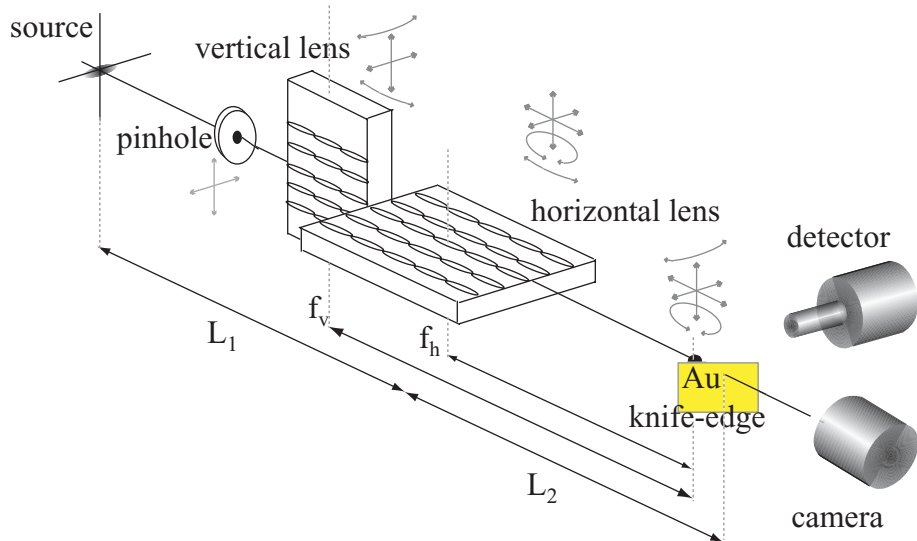
Figure 7.4: Sketch of an experimental arrangement with nanofocusing lenses. The two lenses perpendicular to each other must be aligned to focus in one plane.

the tuning of the geometries for best resolution is not always optimal and a kink occur if with increasing photon energy the radius cannot be reduced. The well established manufacturing techniques are the only argument in favor of silicon. Aluminium brings no real advantage compared to Si. Diamond and boron are very promising candidates. However diamond is difficult to process. When the problems with processing boron and diamond are solved a lateral resolution down to 20 nm can be reached above about 10 keV.

## 7.2 Experimental Implementation

A silicon NFL was tested at ID22 (ESRF). A microbeam setup, similar to that of section 5.2, was used in the present investigation. However, additional degrees of freedom in alignment were needed. They are shown as shaded arrows in figure 7.4. Problems occur due to their accuracy, their reproducibility and the tight space for the whole setup. In fact, the lenses, a pinhole, and the sample must move relatively to each other in a space less than 5 cm. This part of the experiment at ID22 is shown as photograph in figure 7.6. Both lenses are covered with kapton in order to avoid dust contamination. The experiment was done at 25 keV. At that energy the transmission through 8 mm of silicon is so large that a PtIr pinhole (10 $\mu$m or 20 $\mu$m in diameter and 80 $\mu$m thick) is needed in order to do the alignment. The fine alignment and focusing is done using a gold knife-edge mounted on the sample stage. The knife-edge was specially fabricated by lithographic techniques to get a small line-spread. Both NFLs have to be moved with nanometer accuracy, all positions have to be stable and reproducible, a task that is not easily achieved in the nanometer range.
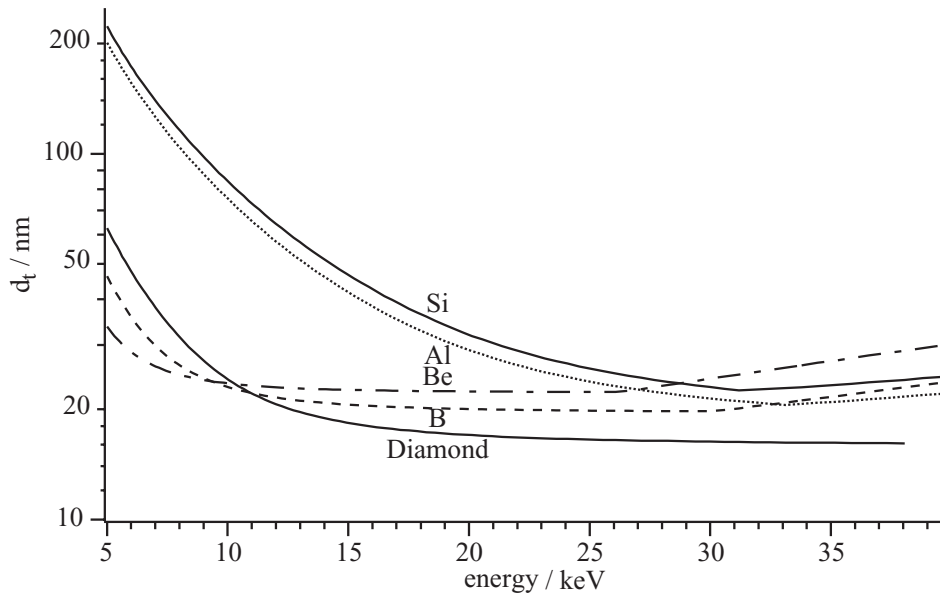
Figure 7.5: Lateral resolution for identical NFLs of the different lens materials silicon, aluminium, beryllium, boron, and diamond in the same typical geometry [parameters: $N = 100$, $L_1 = 40\,m$, $30\,\mu m > R > 0.8\,\mu m$, $\Rightarrow 8\,mm < f < 20\,mm$].
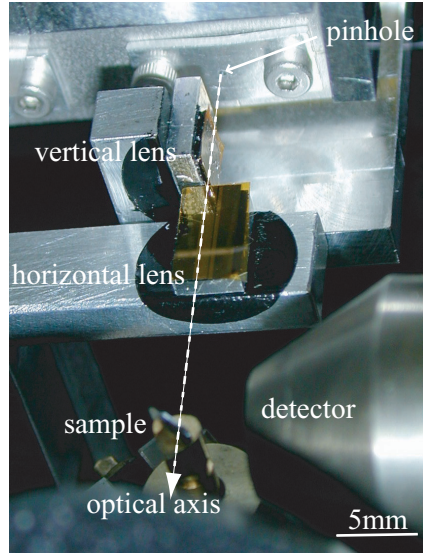


Figure 7.6: Experimental setup with nano focusing lenses as implemented at ESRF/ID22.

## 7.3    NFL Characterization

The NFL system was characterized at $25\,keV$ by the vertical and horizontal Au knife-edge scans of figure 7.7. The synchrotron radiation source (size: $S_h = 700\,\mu m \times S_v = 60\,\mu m$ FWHM) was focused to an image of $B_h = 380\,nm \pm 90\,nm \times B_v = 210\,nm \pm 50\,nm$.
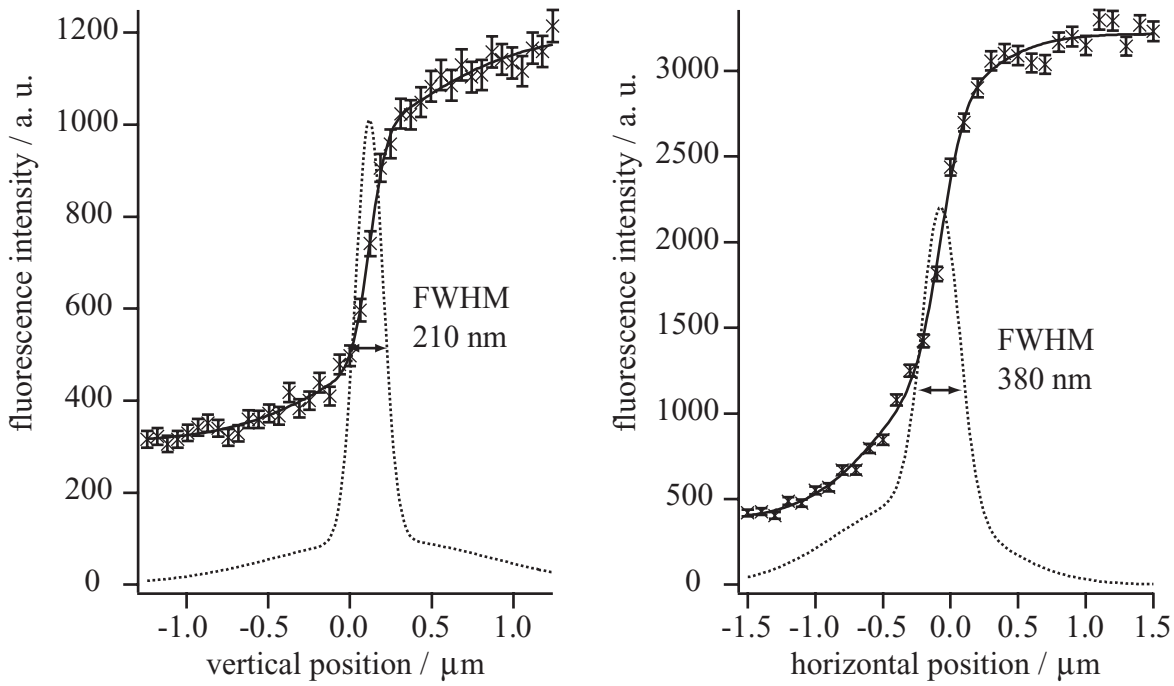
Figure 7.7: Measured gold fluorescence knife-edge scans which characterize the microbeam vertical and horizontal and therefore indicate the NFL performance. The recorded data are fitted by an error function which gaussian derivation represent the size of the microbeam.

The expected spot size was 340 nm and 110 nm. Obviously, there is room for improving the manufacturing process. This is also evidenced by the strong and asymmetric background under the focal spot. A better alignment and a more efficient pinhole might help to reduce the background.

Crossed NFLs offer the opportunity to obtain an almost circular focal spot by adapting the focal lengths of the horizontal and vertical lenses. This is a very interesting feature for most analytical tools. In the present setup this specification has not yet be achieved.

The flux in the focal spot is estimated on the basis of the data in figure 7.7.

$$
\begin{array}{llll}
I_0 = & 4.3 \cdot 10^{12} & \text{ph/(s mm}^2) & \text{[incident radiation]} \\
F_L = & 4.4 \cdot 10^{8} & \text{ph/s} & \text{[through the lenses]} \\
F_f = & 1.2 \cdot 10^{8} & \text{ph/s} & \text{[in the spot]} \\
& 2.1 \cdot 10^{8} & \text{ph/s} & \text{[expected]}
\end{array}
$$
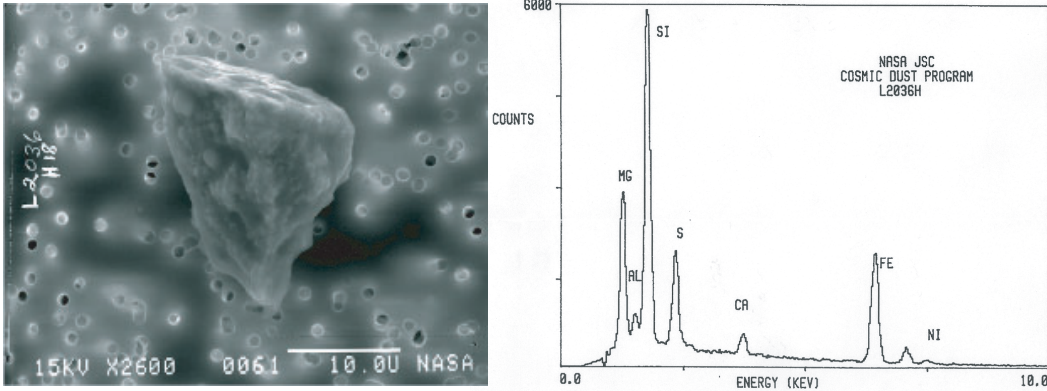
The incident intensity $I_0$ and the total flux behind the lenses were directly recorded by a PIN diode. Only the intensity in the focus area is useful. The flux in the spot can be evaluated with the knife-edge scans of figure 7.7 and is found to be $1.2 \cdot 10^8$ ph/s. It is only smaller by a factor 2 compared to the expected flux. The observed gain was 350.

## 7.4   First Nanofocusing Results

A number of experiments using the NFL prototype have been carried out, showing the following general features:

- The designed focal length of some millimeters generates the demagnification ratios needed to achieve a probing spot of nanometer size at common beamlines of 3rd generation synchrotron radiation facilities.

- The existing equipment is sufficient to align two NFLs to each other and to the synchrotron radiation beam.

- The analysis of small volumes can be performed with hard X-rays.

- Some of the problems not solvable with Be or Al refractive lenses can be tackled with NFLs.

(1) Characterization of the sample in the NASA Cosmic Dust Catalog #15: L2036H18.



(2) Multi channel fluorescence spectrum at ID22 / ESRF.
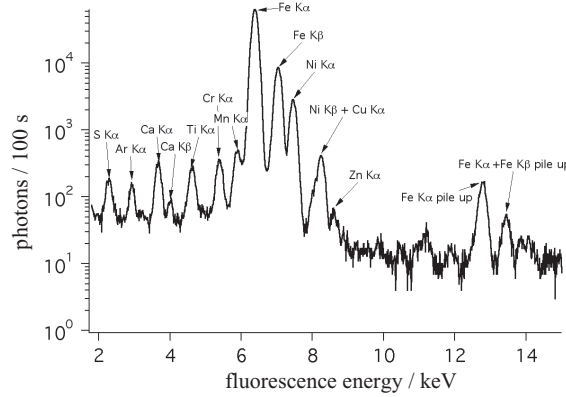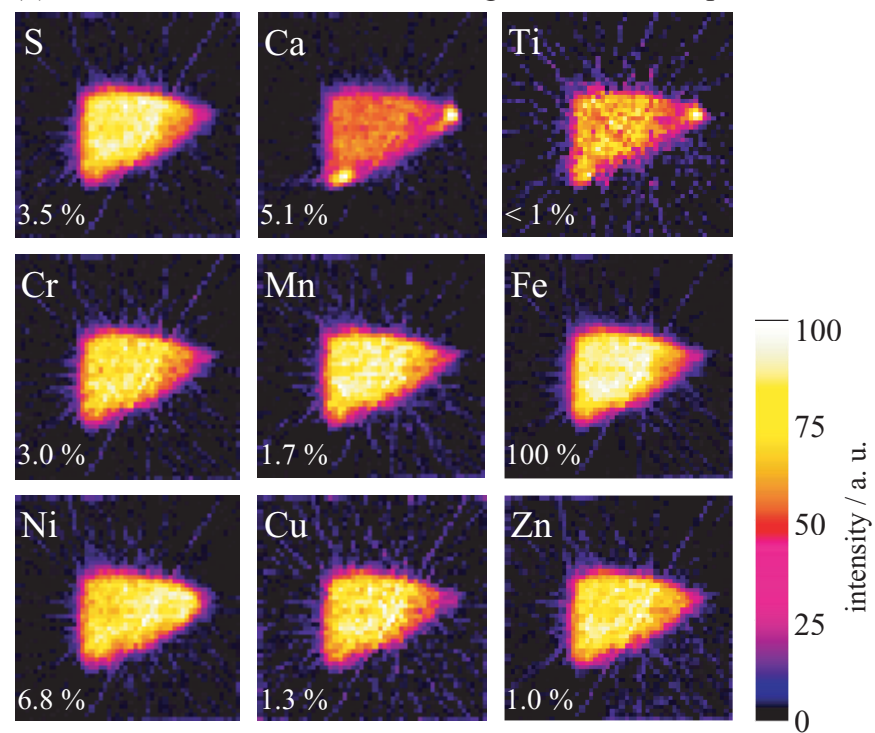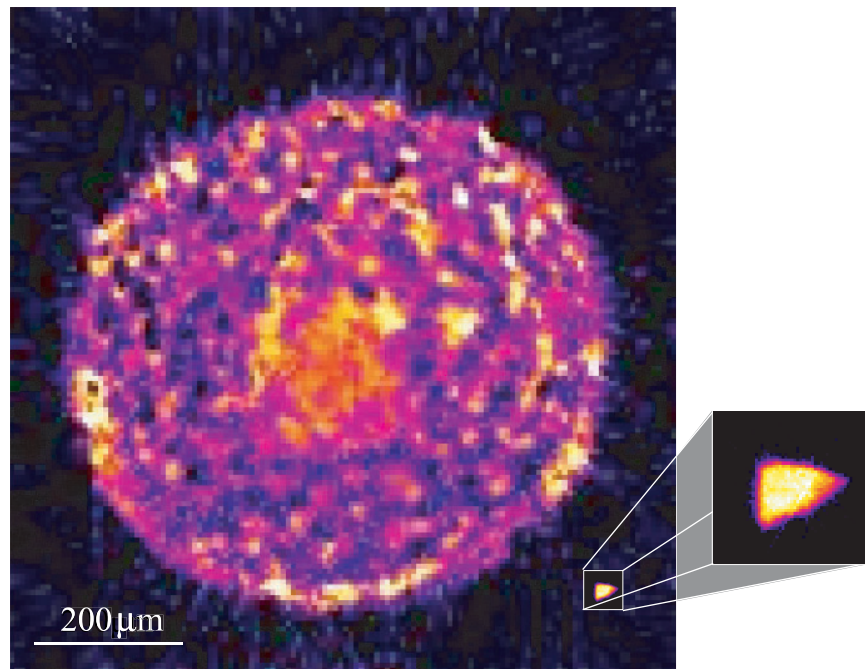


Figure 7.8:  Fluorescence nanotomography of a micrometeorite [59].  (1) Sample description taken from the NASA Dust Catalogue.  (2) Typical multichannel fluorescence spectrum of the meteorite.  (3) Reconstructed fluorescence tomograms for all detected elements. (4) Visualization of the increased spacial resolution due to NFLs (description in the text).

(3) Reconstructed fluorescence tomograms of the components.



(4) Presentation of the sample dimensions: Al lenses versus NFLs.

**Fluorescence tomography of a meteorite with a horizontal resolution of 600 nm**

A micrometeorite, about 20 $\mu$m in size, was analyzed by fluorescence tomography. The meteorite was captured by a high flying plane in the upper atmosphere. It is listed in the NASA Dust Catalogue #15:L2036H18 and was provided by G. Flynn (U. Plattsburgh). The uniqueness of the sample forbids any destructive analytical method. Since the sample is only 20 $\mu$m in size a lateral resolution below 1 $\mu$m is required. The NASA catalogue contains a scanning electron microscope (SEM) picture of the meteorite and an electron induced X-ray (EDX) fluorescence spectrum, shown in figure 7.8(1).

In the present fluorescence tomography elements with X-ray emission lines between 2 keV and 22.5 keV have been detected. This energy region was defined by the incident energy of 25 keV and by scattering and absorption. Absorption was minimized by a helium chamber around the sample and the detector. The high sensitivity of the fluorescence analysis using synchrotron radiation is demonstrated in the measured multichannel spectrum of figure 7.8(2). Obviously, the detection limit is better for excitation by X-rays than by electrons (figure 7.8(1)). More elements can be detected, e. g. Zn. Figure 7.8(3) shows the elementspecific tomograms for 9 elements from sulfur to zinc. A pixel size of 600 nm was achieved by means of 52 translations at 70 rotation positions with 2 s dwell time. To enhance the flux an additional Be parabolic refractive lens was positioned 1100 mm upstream from the NFLs, demagnifying the image of the synchrotron radiation source ~400 mm behind the NFLs. Thus the beam matched the NFL's aperture at their position. This additional beam collimation enhanced the flux from $1.8 \cdot 10^8$ ph/s, with Si refractive lenses alone, to $4.6 \cdot 10^9$ ph/s. The intensity in the tomograms (figure 7.8(3)) is given relative to their maximal concentration. The percentage values show the relation of these maxima to the maximal intensity of Fe. Note the strong variation in the distribution of calcium which is concentrated at two tips of the meteorite. A detailed evaluation of the sample and data analysis including selfabsorption correction is carried out in the PhD thesis of T. F. Günzler (RWTH) [59]. In the present context the gain and the sensitivity obtained by using NFLs is emphasised. This improvement is documented, once more, in figure 7.8(4). Here, the virtual slice through the micrometeorite is compared to a microfluorescence tomogram of the potassium distribution inside a mahogany plant root. That sample which had a diameter of about 750 $\mu$m was analyzed by means of an Al refractive lens ($N = 150$, $E = 19.5$ keV, $f = 0.45$ m, $g = 200$, $F_f = 10^{10}$ ph/s). The spot size was much larger than in the case of the micrometeorite, spotsize $= 1.4 \mu$m $\times 6 \mu$m. The improvement achieved by the NFL is obvious and fluorescence microtomography with a resolution way below 1 $\mu$m is now feasible.

**Diffraction by samples with submicrometer dimensions**

Micro- and nanotechnology require more and more tools to investigate the structure of samples with submicrometer dimensions. Two systems of this type were studied: the sensor part of a giant magnetoresistance (GMR) read head and a phase change storage device. Both experiments were carried out at ID22 / ESRF in close co-operation with M. Drakopoulos (now Diamond Light Source, UK).

**The GMR read head from IBM** is described in functionality and implementation in [60, 61]. This state of the art functional sensor is typical for the problems encountered in diffraction of very small samples. The interesting functional part is only 350 nm $\times$ 300 nm $\times$ 15 nm in

(1)



(2)



(3)



(4)
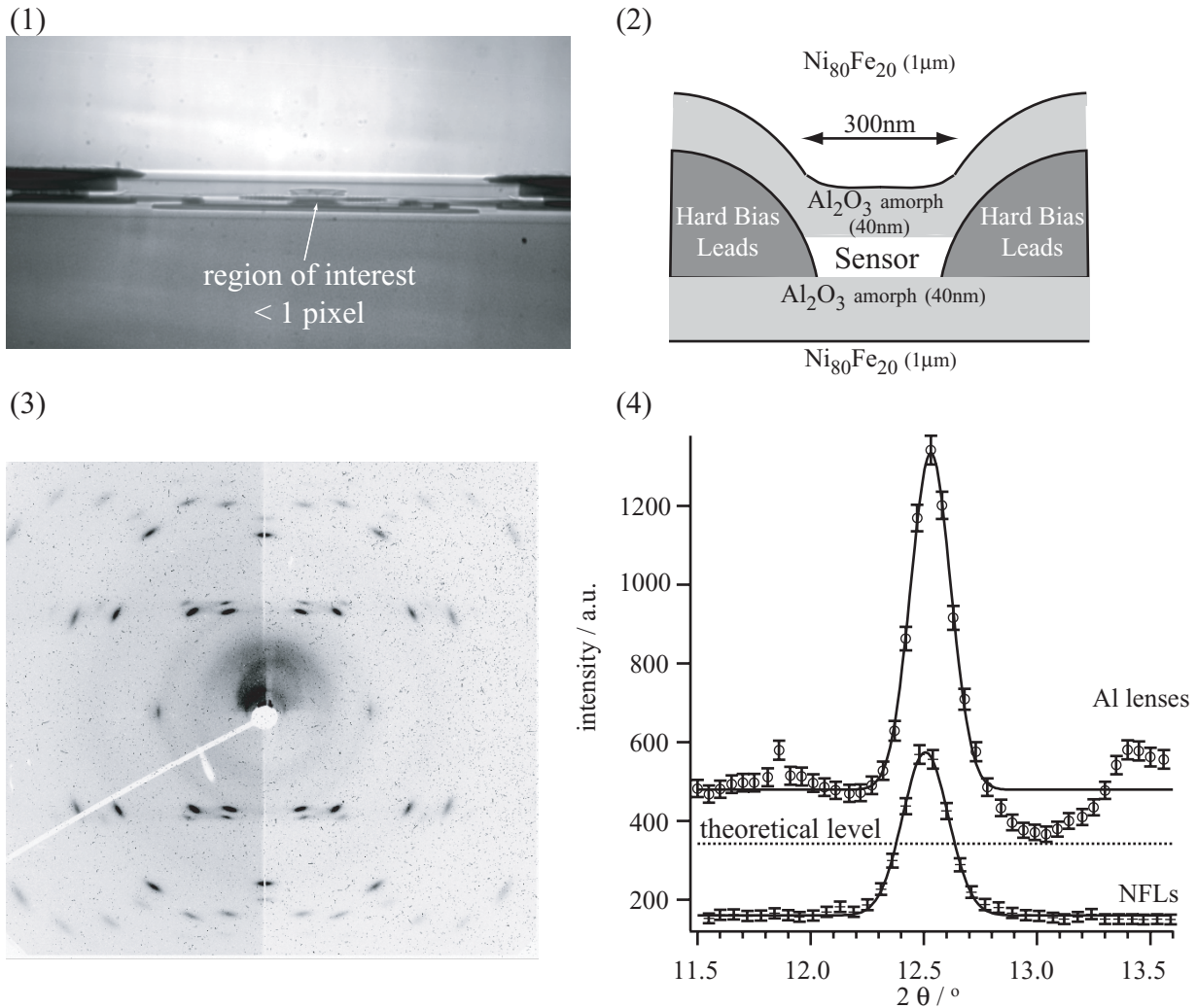


Figure 7.9: Test diffraction experiment of a GMR red head (IBM).
(1)Transmission alignment view of the interesting part of the GMR read head.
(2)Environment of the region of interest, the sensor, provided by C. Schug (IBM).
(3)The Laue pattern of a reference sample fct PtMn on glass during the NFL experiment.
(4)Integrals of an (111) PtMn fct peak comparing different lens setups.

size. Even worse, it is surrounded with strongly absorbing and partly diffracting materials. Furthermore, the complexity of the sample makes the alignment very demanding. The region of interest is illustrated in figure 7.9. A transmission view on a high resolution Princeton camera is imaged in picture (1). By means of this picture the sample is aligned to the optical axis. However, since the region of interest in this image is smaller than one pixel, mapping scans in combination with slight sample rotations are needed for achieving the alignment. Therefore, a detailed knowledge of the sample structure is indispensable. The experiment was performed in cooperation with C. Schug (IBM, SSD Mainz), who provided the samples and the detailed description in figure 7.9(2). The sensor part consist of a face centered

tetragonal PtMn texture (the lattice constants are a $= 3.99\,$Å, c $= 3.70\,$Å). It is unknown how
its structure adapts to its surroundings or how it changes during the active working of the
sensor.

The following two optical setups were directly compared at 25 keV:

| lens material: | aluminium | silicon |
|---|---|---|
| number of lenses: | $N = 250$ | $N_v{=}50$, $N_h{=}100$ |
| spot size: | $0.8\,\mu$m $\times$ $2.5\,\mu$m | $150\,$nm $\times$ $560\,$nm |
| reference example: PtMn (111) | | |
| acquisition time | 300 s | 300 s |
| peak hight [counts/pixel]: | 837 | 409 |
| noise level [counts/pixel]: | 480 | 161 |

The PtMn (111) peak at $2\Theta = 12.5°$ is a good candidate to test the sensitivity of our setup
for detecting the sensor structure in the GMR environment. First, a PtMn reference sample
on a glass substrate was investigated at 25 keV with an Al lens stack ($N = 250$, $f = 0.5\,$m) and
with a Si NFL (horizontal focal length $f_h = 18\,$mm). The probing spots on the sample were
$0.8\,\mu$m $\times 2.5\,\mu$m for the Al lens and $150\,$nm $\times 560\,$nm for the NFL. Figure 7.9(3) shows the
Laue pattern of the PtMn reference sample generated with the help of the NFL optic. The
detected images were calibrated by means of Si and Au standard samples and analyzed with
the program 'FID2D' by A. P. Hammersley (ESRF) [62].

The main result for the PtMn reference sample is shown in figure 7.9(4). It took 300 s in both
cases to collect the data. It is noteworthy that the signal to noise ratio is far superior to that
for the Al lens. Based on these measurements an assumed peak level for the PtMn (111) of
the sensor has been calculated. It is below the noise level for Al lenses, but with NFLs the
sensor peak is expected to be measurable. 5 Up to now, the PtMn signal was not detected
in the GMR sensor. There are many other structural elements around the exact PtMn layer
and it was difficult to find the exact sensor position. The experiences during this experiment
will have impact to more efforts in focusing and/or in sample alignment, which are needed to
detect the signal from a layer only $0.001\,\mu$m$^3$ in volume.

**Phase change media** are interesting candidates for non-volatile data storage devices with a high data storage capacity. AgInSbTe films are a candidate for these media. Data are stored in the form of crystallized submicrometer regions in the amorphous film. Crystallized and amorphous regions have different reflectivity for light. Such a sample was provided by S. Ziegler and M. Wuttig (I. Physikalisches Institut, RWTH). The crystallization kinetics of this complex are described by K. Njoroge et al. [63]. Differences in the crystalline state can be analyzed by hard X-ray microdiffraction. An NFL setup for a photon energy of 25 keV was chosen. A crystallized spot (bit) had a size of 130 nm × 470 nm × 50 nm. This corresponds to a volume of $0.003\,\mu\mathrm{m}^3$. The flux behind the NFL was $\mathsf{F_f} = 2{\cdot}10^8$ ph/s. It took 600 s to collect the diffraction picture in figure 7.10(1). The Debye-Scherrer rings become clearly visible when the photon scattering in air is subtracted from the picture (figure 7.10(2)). Three peaks (103), (106), and (110) are identified [63]. They show the correct intensity ratios and no expected peaks are missing. Note that this signal originates from a sample volume of only $0.003\,\mu\mathrm{m}^3$, which corresponds to about $10^7$ unit cells.
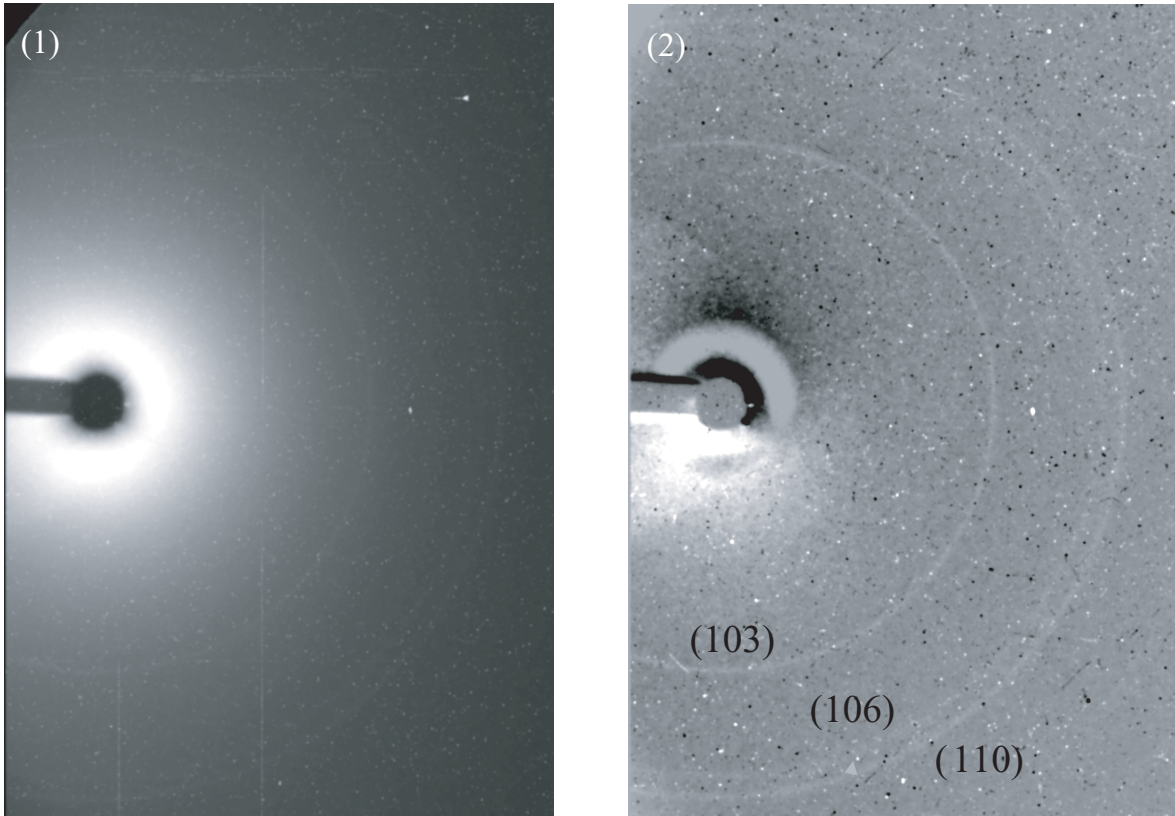


Figure 7.10: Nanodiffraction of an AgInSbTe thin film: a volume of $0.003\,\mu\mathrm{m}^3$ forms the base of the measured diffraction image (1), the Laue pattern becomes clearer when the photon scattering in air is subtracted (2).

## 7.5   Nanofocusing Lenses: Summary and Outlook

Parabolic refractive planar lenses with small radii of curvature R of $1\,\mu$m to $3\,\mu$m were fabricated by micro structuring processes in silicon. This design allows very short focal lengths, some few millimeter, which results in an extreme demagnification of the imaged synchrotron radiation source. This design makes nanoanalysis with hard X-rays possible.

A tomography experiment with the NFL prototype demonstrated the improvements for scanning analytical methods like fluorescence tomography. The tomographic reconstructions of a meteorite, only $20\,\mu$m in size was presented, with a resolution of $600\,$nm.

The diffraction of a GMR sensor head with an active sensor size of only $350\,$nm $\times$ $300\,$nm $\times$ $15\,$nm (or $0.0015\,\mu$m$^3$) underlines the necessity to use a nanoprobe. The comparison between rotational Al lenses and planar Si lenses underlined the abilities of the new NFL concept. The analysis of the sensor head is not possible without nanofocusing lenses. Finally, the Laue pattern out of $1.1{\cdot}10^7$ cells in a AgInSbTe thin film demonstrated that the achieved intensity gain is already sufficient for certain experiments.

A number of improvements in nanofocusing lenses is envisaged for the near future.

First, the alignment system for diffraction experiments has to be improved. This includes the degree of freedom for the lens alignment, a pinhole at close distance to the lens and the sample holder. Vibrations and other uncontrolled motions in the setup have to be avoided.

Second, the parabolic shape of the nanofocusing lenses has to be improved.

Finally, silicon is not the optimum material for NFLs. However, the microfabrication of silicon is well developed. Better materials with lower absorption are diamond, graphite, and boron. Appropriate processing procedures have to be developed for these materials.

# Chapter 8

# Summary

Parabolic refractive X-ray lenses show an outstanding potential for micro- and nano-analysis and for imaging with hard X-rays. Imaging can be done in absorption, fluorescence, diffraction, and small angle scattering. Beryllium as lens material has turned out as ideal material for photon energies below about $40\,\mathrm{keV}$. The lenses are manufactured with a rotational parabolic profile as is demonstrated by the quality of the images which are free of spherical aberration. A lateral resolution of $140\,\mathrm{nm}$ has been achieved. Beryllium as lens material improves the transmission of the refractive lenses and increases the field of view. This is favorable for microfocusing, and helps to improve microtomography and micro small angle scattering. The development of XANES microtomography is also made possible by these improvements. $90\,000$ single XANES spectra for one tomogram were handled in acquisition and data processing. It allows for chemical analysis in each pixel of the sample without need for sample destruction. Furthermore, the requirements on beryllium parabolic refractive lenses at an X-ray free electron laser XFEL have been investigated. Today, the implementation of microanalysis methods at an XFEL by using parabolic refractive lenses seems possible. In that respect, novel experiments will become feasible in many fields of science, in particular in the structure analysis of individual large biological molecules.

In order to push the resolution in microanalysis in the range below $100\,\mathrm{nm}$, new refractive lenses (nanofocusing lenses) with extremely short focal lengths have been developed. A prototype of such NFL's has been manufactured in silicon. The radius of curvature varies between $1\,\mu\mathrm{m}$ and $3\,\mu\mathrm{m}$. The potential of this concept is outstanding. A microprobe smaller than $100\,\mathrm{nm}$ is already feasible, and a microprobe smaller than $50\,\mathrm{nm}$ can be expected in the view of the ongoing improvements in the lens material. We were able to achieve diffraction pattern from a small volume ($50\,\mathrm{nm} \times 470\,\mathrm{nm} \times 130\,\mathrm{nm}$) consisting of $\sim 10^8$ atoms. A micrometeorite was analyzed in voxels of $600\,\mathrm{nm}$, even in horizontal direction. The larger size of synchrotron radiation source in horizontal direction can be compensated by a stronger demagnification of the source image in this direction. The alignment of NFLs under realistic experimental conditions is a demanding task. A compact and portable setup has been developed, including two independent NFLs for horizontal and vertical focusing, a pinhole, and the sample holder. This allows a lens exchange and alignment under realistic circumstances in about 2 hours. Hence, the limited available beamtime at synchrotron radiation facilities can be efficiently used in data acquisition.

Parabolic refractive X-ray lenses have greatly improved our capability to combine imaging techniques with spectroscopy, which will be required in many fields of science and technology.

# Appendix A

# The Choice of Lens Material

The trade of between high refraction of a refractive lens and little absorption is the basic problem for refractive optics with hard X-rays. As outlined in section 2.1, the mass attenuation coefficient $\mu/\rho$ is a quality factor for that purpose and in this context elements with a low atomic number $Z$ are preferred. Nevertheless, this argument depends on the energy of the X-rays and with that on the analytical application the lenses are used for.

The lens material has to meet some additional criteria. First, the material has to withstand the radiation on long timescales without loss of optical performance. Another requirement is a small degree of small angle X-ray scattering. Tests for both properties can be found in the PhD thesis of J. Tümmler (RWTH Aachen) [64]. A third criterium is the ability to give the material the required parabolic shape.

In the following only materials are presented which result in lenses or which are considered as promising.

**Aluminium Al:** is the material of which the first parabolic refractive X-ray lenses were manufactured. Its atomic number is $Z = 13$ and this is far from optimal considering the mass attenuation coefficient $\mu/\rho$. Obviously, the main argument for aluminium is its plasticity. It is ductile at room temperature and the thin oxidized layer at its surface prevent further corrosion. The development of parabolic refractive lenses of aluminium is described in [64] and the first results of a full field microscope in the hard X-ray region was presented by [21] in 1999. Since then, aluminium refractive lenses have been used for analytical applications in an energy range between $20\,\mathrm{keV}$ and $120\,\mathrm{keV}$ at 3rd generation synchrotron facilities.

**Lithium Li:** is the solid with the lowest atomic number, $Z = 3$. Unfortunately for the manufacturing of lenses it oxidizes immediately in air, loosing its shape and optical performance. Lenses have to be manufactured under inert gas atmosphere and must be sealed when used as optical element. These conditions were considered as too complicated, especially as lithium lenses promise only a small experimental profit compared to beryllium. This is indicated for example in figure 7.5 where the good resolution of Li lenses can also be realized with Be lenses. Nevertheless, in a teeth lens design coated Li have been tested as optical element at $10\,\mathrm{keV}$, [65].

**Beryllium Be:** has a higher density than Li and therefore the coefficient $\mu/\rho$ is comparable. Safety precautions have to be taken when handling beryllium. Beryllium is much harder than aluminium and the pressing of Be is done at elevated temperature.

Parabolic refractive lenses of Be were used in many different experiments since 2002. The improvements for analytical applications are topics of the chapters 4 and 5.

**Nickel Ni:** is an option as lens material for photon energies above $100\,\mathrm{keV}$, as shown in figure 4.2. Parabolic refractive Ni lenses were manufactured in Aachen and were tested at ID22 / ESRF.

**Boron B:** with $Z = 5$ and a relatively high density, boron was often considered as lens material. But boron has a high melting point, extreme hardness, and strong reactivity at higher temperatures with many other elements. Recently, parabolic refractive lenses in the design for nanofocusing lenses (figure 2.5 and chapter 7) were realized with boron and are under further development.

**Silicon Si:** is one of the best known materials and can be shaped accurately on a sub-$\mu$m scale. Therefore, the second design of parabolic refractive lenses was first realized in Si by standard micromachining techniques. Parabolic radii $R$ of $\sim1\,\mu$m minimize the possible focal length of refractive lenses. This is the approach for the strong demagnification required for a nanoprobe. The planar parabolic X-ray lenses are presented in chapter 7.

**Carbon/Diamond C:** Diamond is the material of low $Z$ with the highest density. The material was used for optical elements already [66]. It is considered as material for etched nanofocusing lenses but until now, lenses as presented here were not structured in diamond. Whereas, carbon in its graphite representation have been processed and first results are awaited.

# Bibliography

[1] R. W. James: *The Optical Principles of the Diffraction of X-Rays* (G. Bell and Sons LTD, London, 1962)

[2] E. Hecht: *Optics (second edition)* (Addison-Wesley, 1987)

[3] C. T. Chantler: *Theoretical form factor, attenuation and scattering tabulation for Z = 1 - 92 from E = 1 - 10eV to E = 0.4, 10.0MeV*, in Journal of Physical and Chemical References Data, volume 24, 71 (1995)

[4] J. H. Hubbell and S. M. Seltzer: *Tables of X-Ray Mass Attenuation Coefficients and Mass Energy-Absorption Coefficients*, in URL: http://physics.nist.gov/PhysRefData/XrayMassCoef/ (1996)

[5] P. Kirkpatrick and A. V. Baez: *Formation of Optical Images by X-Rays*, in Journal of the Optical Society of America, volume 38, 9 (1948)

[6] N. Gao, I. Y. Ponomarev, Q. F. Xiao, W. M. Gibson, and D. A. Carpender: *Monolithic polycapillary focusing optics and their applications in microbeam x-ray fluorescence*, in Applied Physics Letters, volume 69, 1529 (1996)

[7] K. Janssens, L. Vincze, B. Vekemans, F. Adams, M. Haller, and A. Knöchel: *Use of lead-glass capillaries for micro-focusing of highly-energetic (0-60 keV) synchrotron radiation*, in Journal of Analytic Atomic Spectroscopy, volume 13, 339 (1998)

[8] J. Kirz: *Phase zone plates for x rays and the exteme uv*, in Journal of the Optical Society of America, volume 64 (1974)

[9] S. D. Shastri, J. M. Maser, B. Lai, and J. Tys: *Microfocusing of 50 keV undulator radiation with two stacked zone plates*, in Optical Communication, volume 197, 9 (2001)

[10] S. Tamura, M. Yasumoto, N. Kamijo, Y. Suzuki, M. Awaji, A.Takeuchi, H. Takano, and K. Handa: *Development of a multilayer Fresnel zone plate for high-energy synchrotron radiation X-rays by DC sputtering deposition*, in Journal of Synchrotron Radiation, volume 9, 154 (2002)

[11] E. DiFabrizio, F. Romanato, M. Gentill, S. Cabrini, B. Kaulich, J. Susini, and R. Barrett: *High-efficiency multilevel zone plates for keV X-rays*, in Nature, volume 401 (1999)

[12] W. C. Röntgen: *Ueber eine neue Art von Strahlen.*, in Sitzungsberichte der physikal.-medicin. Gesellschaft, p. 132 (1895)

[13] C. Barkla: *Note on Experiments to detect Refraction of X-rays*, in Philosophical Magazine, volume 31, 257 (1916)

[14] S. Suehiro, H. Miyaji, and H. Hayashi: *Refractive lens for X-ray focus*, in Nature, volume 352, 385 (1991)

[15] A. G. Michette: *No X-ray lens*, in Nature, volume 353, 510 (1991)

[16] B. X. Yang: *Fresnel and refractive lenses for X-rays*, in Nuclear Instruments and Methods in Physics Research A, volume 328, 578 (1993)

[17] A. Snigirev, V. Kohn, I. Snigirev, and B. Lengeler: *A compound refractive lens for focusing high-energy X-rays*, in Nature, volume 384, 49 (1996)

[18] T. Tomie: *Japanese Patent No. 06045288*, in (1994)

[19] T. Tomie: *US Patent No. 5,684,852*, in (1997)

[20] T. Tomie: *German Patent No. DE19505433*, in (1998)

[21] B. Lengeler, C. Schroer, M. Richwin, J. Tümmler, M. Drakopoulos, I. Snigireva, and A. Snigirev: *Imaging by parabolic refractive lenses in the hard x-ray range*, in J. Synchrotron Rad., volume 6, 1153 (1999)

[22] C. G. Schroer, J. Tümmler, F. Günzler, B. Lengeler, W. H. Schröder, A. J. Kuhn, A. S. Siminiovici, A. Snigirev, and I. Snigireva: *Fluorescence Microtomography: External Mapping of Elements Inside Biological Samples*, in Proeedings of SPIE, volume 4142, 287 (2000)

[23] C. G. Schroer, B. Lengeler, B. Benner, T. F. Günzler, M. Kuhlmann, A. S. Siminiovici, S. Bohic, M. Drakopoulos, I. S. A. Snigirv, and W. Schröder: *Microbeam Production Using Compound Refractive Lenses: Beam Characterization and Applications*, in Proceedings of SPIE, volume 4499, 52 (2001)

[24] C. G. Schroer, M. Kuhlmann, B. Lengeler, T. F. Günzler, O. Kurapova, B. Benner, C. Rau, A. S. Siminiovici, A. Snigirev, and I. Snigireva: *Beryllium parabolic refractive x-ray lenses*, in Proeedings of SPIE, volume 4783, 10 (2002)

[25] C. G. Schroer, M. Kuhlmann, T. Hunger, F. Günzler, O. Kurapova, S. Feste, F. Frehse, B. Lengeler, , M. Drakopoulos, A. Somogyi, A. S. Simionovici, A. Sngirev, I. Snigireva, C. Schug, and W. H. Schröder: *Nanofocusing parabolic refractive lenses*, in Applied Physics Letters, volume 82, 1485 (2003)

[26] B. Lengeler, C. G. Schroer, B. Benner, A. Gehardus, F. Günzler, M. Kuhlmann, J. Meyer, and C. Zimprich: *Parabolic refractive X-ray lenses*, in Journal of Synchrotron Radiation, volume 9, 119 (2002)

[27] B. Lengeler, C. Schroer, M. Richwin, J. Tümmler, M. Drakopoulos, A. Snigirev, and I. Snigireva: *A novel microscope for hard x-rays based on parabolic compound refractive lenses*, in Applied Physical Letters, volume 74, 3924 (1999)

[28] B. Lengeler, J. Tümmler, A. Snigirev, I. Snigireva, and C. Raven: *Transmission and gain of singly and doubly focusing refractive x-ray lenses*, in Journal of Applied Physics, volume 84, 5855 (1998)

[29] S. G. Lipson, H. Lipson, and D. S. Tannhauser: *Optical Physics* (Cambridge University Press, 1998)

[30] B. Benner: *Imaging with Parabolic Refractive X-Ray Lenses*, Ph.D. thesis, RWTH Aachen, Aachen

[31] C. G. Schroer, J. Meyer, M. Kuhlmann, B. Benner, T. F. Günzler, B. Lengeler, C. Rau, T. Weitkamp, A. Snigirev, and I. Snigireva: *Nanotomography based on hard x-ray microscopy with refractive lenses*, in Applied Physics Letters, volume 81, 8 (2002)

[32] J.-C. Labiche, J. S. Puchades, D. von Brussel, and J. Moy: *FRELON Camera: Fast REadout LOw Noise*, in ESRF Newsletter, volume 25, 41 (1996)

[33] J. Radon: *Über die Bestimmung von Funktionen durch ihre Integralwerte längs gewisser Mannigfaltigkeiten*, in Ber. Ver. Sächs. Akad. Wiss., volume 69, 262 (1917)

[34] A. Kak and M. Slaney: *Principles of Computerized Tomographic Imaging* (IEEE Press, 1988)

[35] C. G. Schroer: *Reconstructing X-Ray Fluorescence Microtomograms*, in Applied Physics Letters, volume 79, 1912 (2001)

[36] C. Zimprich: *Demagnifying X-Ray Lithography*, Ph.D. thesis, RWTH Aachen, Aachen (2003)

[37] S. V. Roth, M. Burghammer, R. Gilles, D. Mukherji, J. Rösler, and P. Strunz: *Precipitate scanning in Ni-base $\gamma\gamma'$-superalloys*, in Nuclear Instruments and Methods in Physics Research B, volume 200, 255 (2003)

[38] C. G. Schroer, J. Tümmler, B. Lengeler, M. Drakopoulos, A. Snigirev, and I. Snigireva: *Compound Refractive Lenses: High Quality Imaging Optics for the XFEL*, in Proceedings of SPIE, volume 4143, 60 (2001)

[39] *TESLA Technical Design Report; Part V The X-Ray Free Electron Laser*, in (2001)

[40] *TESLA Technical Design Report, Supplement*, in

[41] H. Schulte-Schrepping: *Photon beamlines at X-FEL undulators*, in Proceedings of SPIE, volume 4143, 9 (2001)

[42] R. M. Bionta: *Controlling dose to low Z solids at LCLS*, in technical report Lawrence Livermore National Laboratory, LCLS-TN-00-4 (2000)

[43] C. G. Schroer, M. Kuhlmann, F. Günzler, B. Lengeler, M. Richwin, B. Griesebock, D. Lützenkirchen-Hecht, R. Frahm, E. Ziegler, A. Mashayekhi, D. R. Haeffner, J.-D. Grunwaldt, and A. Baiker: *Mapping the chemical states of an element inside a sample using tomographic x-ray absorption spectroscopy*, in Applied Physics Letters, volume 82, 3360 (2003)

[44] B. Henke, E. Gullikson, and J. Davis: in Atomic Data and Nuclear Data Tables, volume 54, 181 (1993)

[45] J. Stöhr: *NEXAFS Spectroscopy* (Springer, 1996)

[46] D. C. Koningsberger and R. Prins, eds.: *X-Ray Absorption: Principles, Applications, Techniques of EXAFS, SEXAFS and XANES* (John Wiley & Sons, 1988)

[47] E. A. Stern and S. M. Heald: *Basic Principles and Applications of EXAFS* (1983)

[48] R. Frahm: *New method for time dependent x-ray absorption studies*, in Review of Scientific Instruments, volume 60, 2515 (1989)

[49] M. Richwin: *Entwicklung und Anwendung neuer Verfahren zur zeitaugelösten Röntgenabsorbtionsspektroskopie mit Synchrotronstrahlung*, Ph.D. thesis, Bergische Universität Wuppertal (2002)

[50] J.-D. Grunwaldt and B. S. Clausen: *Combining XRD and EXAFSwith on-line catalytic studies for in situ characterization of catalyst.*, in Topics in Catalysis, volume 18 (2002)

[51] J.-D. Grunwaldt, D. Lützenkirchen-Hecht, M. Richwin, S. Grundmann, B. S. Clausen, and R. Frahm: *Piezo X-ray Absorption Spectroacopy for the Investigation of Solid-State Transformations in the Millisecond Range*, in Journal of Physical Chemistry B, volume 105, 5161 (2001)

[52] T. L. Reitz, P. L. Lee, K. F. Czaplewski, J. C. Lang, K. E. Popp, and H. H. Kung: *Time-resolved XANES Investigation of CuO/ZnO in the Oxidative Methanol Reforming Reaction*, in Journal of Catalysis, volume 199, 193 (2001)

[53] J.-D. Grunwaldt, M. Maciejewski, and A. Baiker: *I situ X-ray absorption study during methane combustion over $Pd/ZrO_2$ catalysts*, in Physical Chemistry Chemical Physics, volume 5, 1481 (2003)

[54] C. G. Schroer, B. Benner, T. F. Günzler, M. Kuhlmann, B. Lengeler, W. H. Schröder, A. J. Kuhn, A. S. Siminiovici, A. Snigirev, and I. Snigireva: *High Resolution Element Mapping Inside Biological Samples Using Fluorescence Microtomography*, in Proceedings of SPIE, volume 4503, 230 (2002)

[55] W. Yun, B. Lai, Z. Cai, J. Maser, D. Legnini, E. Gluskin, Z. Chen, A. A. Krasnoperova, Y. Vladimirsky, R. Cerrina, E. D. Fabrizio, and M. Gentili: in Review of Scientific Instruments, volume 70, 2238 (1999)

[56] K. Yamauchi, K. Yamamura, H. Mimura, Y. Sano, A. Saito, A. Souvorov, M. Yabashi, K. Tamasaku, T. Ishikawa, and Y. Mori: in Journal of Sunchrotron Radiation, volume 9, 313 (2002)

[57] O. Hignette, G. Rostaing, P. Cloetens, A. Rommeveaux, W. Ludwig, and A. Freund: *Submicron focusing of hard X-rays with reflecting surfaces at the ESRF*, in Proceedings of SPIE, volume 4499, 105 (2001)

[58] V. Aristov, M. Grigoriev, S. Kuznetsov, L. Shabelnikov, V. Yunkin, T. Weitkamp, C. Rau, I. Snigireva, A. Snigirev, M. Hoffmann, and E. Voges: *X-ray refractive planar lens with minimized absorption*, in Applied Physics Letters, volume 77, 4058 (2000)

[59] T. F. Günzler: *Element-specific X-ray Fluorescence Microtomography*, Ph.D. thesis, RWTH Aachen, Aachen (2004)

[60] D. E. Heim, R. E. Fontana, C. Tsang, V. S. Speriosu, B. A. Gurney, and M. L. Williams: *Design and Operation of Spin Valves Sensors*, in IEEE Transactions on Magnetics, volume 30 (1994)

[61] C. Tsang, R. E. Fontana, T. Lin, D. E. Heim, V. S. Speriosu, B. A. Gurney, and M. L. Williams: *Design, Fabrication and Testing of Sin-Valve Read Heads for High Density Recording*, in IEEE Transactions on Magnetics, volume 30 (1994)

[62] A. P. Hammersley, S. O. Svensson, M. Hanfland, A. N. Fitch, and D. Häusermann: *Two-Dimensional Detector Software: From Real Detector to Idealised Image or Two-Theta Scan*, in High Pressure Research, volume 14, 235 (1996)

[63] W. K. Njoroge and M. Wuttig: *Crystallization kinetics of sputter-deposited amorphous AgInSbTe films*, in Journal of Applied Physics, volume 90, 3816 (2001)

[64] J. Tümmler: *Development of Compound Refractive Lenses for Hard X-Rays*, Ph.D. thesis, RWTH Aachen, Aachen (2000)

[65] E. M. Dufresne, D. A. Arms, R. Clarke, N. P. Pereira, S. B. Dierker, and D. Foster: *Lithium metal for x-ray refractive optics*, in Applied Physics Letters, volume 79, 4085 (2001)

[66] B. Nöhammer, J. Hosowska, A. K. Freund, and C. David: *Diamond planar refractive lenses for third- and forth-generation X-ray sources*, in Journal of Synchrotron Radiation, volume 10, 168 (2003)

# List of Figures

# Acknowledgements to

**, and thanks for**

... the change in mimic of the person I try to propose an experiment immediately the moment I mention being a member of the group of Bruno Lengeler. Changing from 'not possible' into 'maybe I miss something, we should try!'.

... the single event I was faster in realizing a task than Christian has simulated it.

... my colleague Boris living a non-egoism I benefit way to often.

... the pride Thomas developed during the NFL project - it always takes a smile on my face, and for his friendship.

... physics, being the only thing Florian and I have in common. I have never thought of respecting someone I disagree so often, I still don't understand it.

... Olga coming along, adding a fine humor and an intelligent knowing of people beside her hard work for the group.

... the breath taking months with Malte. He, Thomas and I won the match versus boron, finally.

... the time during the beamtime. So I get to know Jens musical interests (imitation of live), which are sometimes interpreted by the motor movements.

... the knowing of Regina that physicians and bureaucracy often do not fit.

... all lenses Martin has manufactured (instead of me).

... our lights Mario has left; 'the' adapting plate constructed by Sebastian; the different perspective presented by Fatima; the 3D look of our results directed by Jannik; the belletristic of Hartmut.

... the end of all the problems, frustrations, and overtime during the machining of the pressing tools, each single time. I think Herbert Schlösser and Frank Neubauer will agree.

... the simple courage Michael Drakopoulos had shown by using the NFLs the first time.

... the foreign worker job with the boss Matthias Richwin and the warrior Bernd Grisebock.

... the weekly email from/to Gerda which has become a part of my life (ACKW 230).

... the trust and the perspective of my family.

...

# Curriculum Vitae

| | |
|---|---|
| Name: | Marion Kuhlmann |
| Date of birth: | 3.August 1969 |
| Place of birth: | Bramsche, Germany |

| | |
|---|---|
| 08.1976 - 06.1980 | Elementary school 'Meyerhof', Bramsche |
| 07.1980 - 06.1982 | Attendance at the 'Orientierungsstufe Innenstadt', Bramsche |
| 07.1982 - 07.1985 | Attendance at the 'Gymnasium Bramsche', Bramsche |
| 08.1985 - 05.1986 | Attendance at the 'Realschule Bramsche', Bramsche |
| 07.1986 - 05.1988 | Business school 'Fachgymnasium Wirtschaft Osnabrück', Osnabrück |
| 10.1988 - 12.1992 | Education computer science at the 'Friedrich-Alexander Universität Erlangen-Nürnberg', Erlangen |
| 10.1994 - 09.1999 | Education physics at the University Osnabrück, Osnabrück |
| 01.2000 - 10.2004 | PhD studies at Aachen University, Aachen |